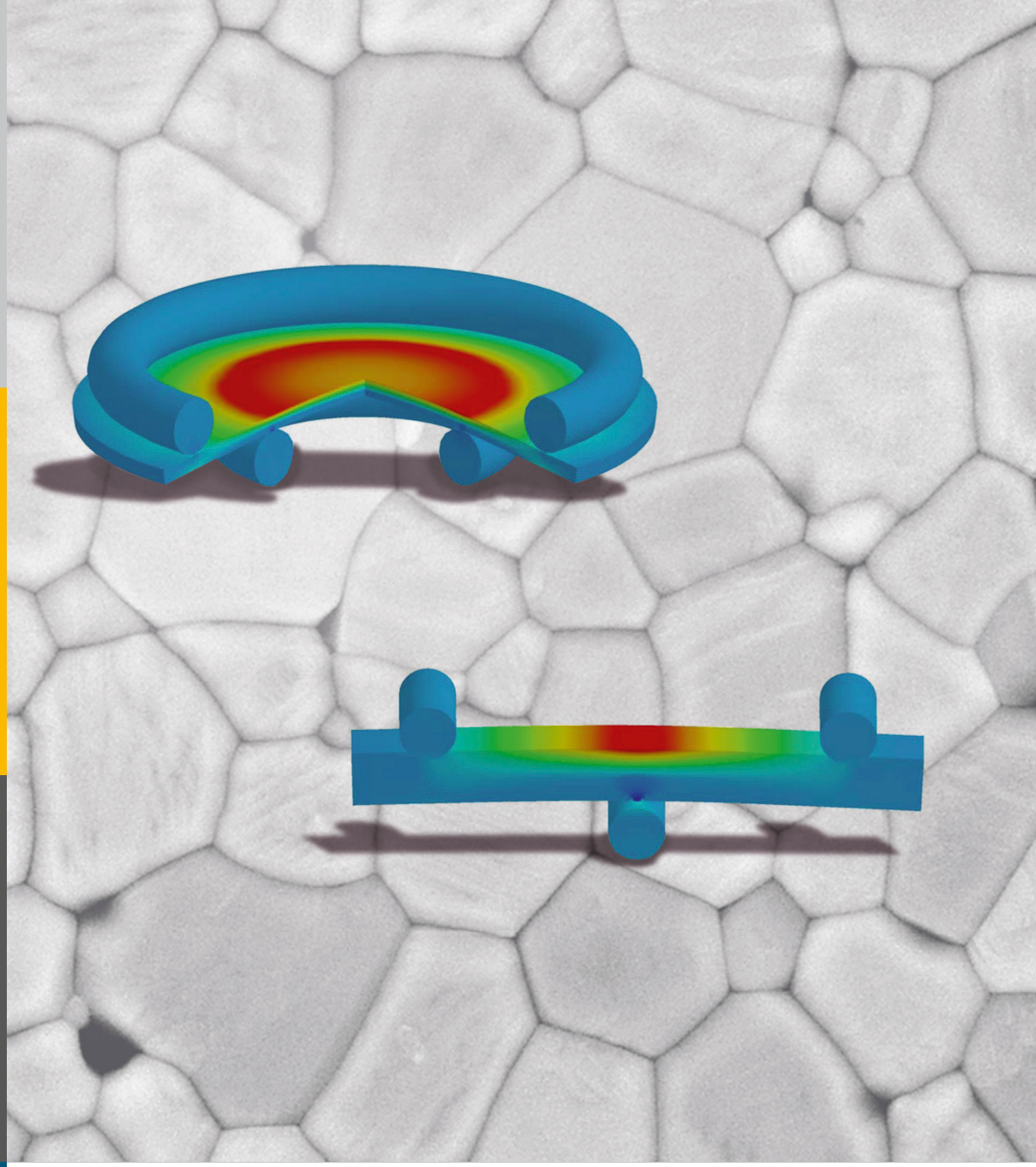

Thermo-mechanical investigations and predictions for oxygen transport membrane materials

Goran Pećanac

JÜLICH
FORSCHUNGSZENTRUM

Member of the Helmholtz Association

Schriften des Forschungszentrums Jülich
Reihe Energie & Umwelt / Energy & Environment Band / Volume 178

Forschungszentrum Jülich GmbH
Institute of Energy and Climate Research (IEK)
Microstructure and Properties of Materials (IEK-2)

Thermo-mechanical investigations and predictions for oxygen transport membrane materials

Goran Pećanac

Schriften des Forschungszentrums Jülich
Reihe Energie & Umwelt / Energy & Environment Band / Volume 178

ISSN 1866-1793 ISBN 978-3-89336-878-5

Bibliographic information published by the Deutsche Nationalbibliothek.
The Deutsche Nationalbibliothek lists this publication in the Deutsche Nationalbibliografie; detailed bibliographic data are available in the Internet at http://dnb.d-nb.de.

Publisher and Distributor: Forschungszentrum Jülich GmbH
Zentralbibliothek
52425 Jülich
Tel: +49 2461 61-5368
Fax: +49 2461 61-6103
Email: zb-publikation@fz-juelich.de
www.fz-juelich.de/zb

Cover Design: Grafische Medien, Forschungszentrum Jülich GmbH

Printer: Grafische Medien, Forschungszentrum Jülich GmbH

Schriften des Forschungszentrums Jülich
Reihe Energie & Umwelt / Energy & Environment, Band / Volume 178

D 82 (Diss., RWTH Aachen University, 2013)

ISSN 1866-1793
ISBN 978-3-89336-878-5

The complete volume is freely available on the Internet on the Jülicher Open Access Server (JUWEL) at www.fz-juelich.de/zb/juwel

Kurzfassung

Eine der effizientesten Wege zur Umsetzung des Oxy-fuel Prozesses ist die Verwendung keramischer, sauerstoffleitender Membrane zur Sauerstoffabtrennung. Der Oxy-fuel Prozess führt zu deutlich niedrigeren Wirkungsgradverlusten im Vergleich zur konventionellen kryogenischen Abtrennungstechnologie. Aufgrund der aus der Sauerstoffpartialdruckdifferenz resultierenden Triebkraft wird Sauerstoff über Leerstellen im Kristallgitter der Membran transportiert. Dünne, durch ein poröses Substrat unterstützte, Membraneschichten werden als effizienteste Designumsetzung angesehen. Das poröse Substrat gewährleistet hierbei die mechanische Stabilität der gesamten Membranstruktur. Die Betriebstemperatur ist relativ hoch, da die Freisetzung von Sauerstoffatomen aus dem Gitter bei erhöhten Temperaturen den Transportprozess unterstützt. Aufgrund ihrer vorteilhaften Transporteigenschaften, einer essentiellen funktionalen Voraussetzung, wurden verschiedene Materialien als vielversprechendes Membran- und Substratmaterial vorgeschlagen, im Einzelnen: $Ba_{0.5}Sr_{0.5}Co_{0.8}Fe_{0.2}O_{3-\delta}$, $La_{0.58}Sr_{0.4}Co_{0.2}Fe_{0.8}O_{3-\delta}$, $Ce_{0.9}Gd_{0.1}O_{1.95-\delta}$ und als alternatives Substratmaterial, die neuartige Fe21Cr7Al1Mo0.5Y Legierung. Zielsetzung der vorliegenden Studie ist die thermo-mechanische Charakterisierung und der Vergleich dieser Materialien.

Fundamentale mechanische Charakteristika wie elastisches Verhalten und Versagenseigenschaften wurden ermittelt um die Langzeitfunktionalität der Materialien sicherzustellen. Die Langzeitverlässlichkeit hängt jedoch nicht nur von der anfänglichen Festigkeit ab, sondern auch von Festigkeitsdegradations - Effekten. Insbesondere wurde die Empfindlichkeit für Umgebungsmedium unterstütztes Risswachstum bei unterkritischen Spannungsniveaus betrachtet und als Basis für eine Festigkeits-Wahrscheinlichkeits-Zeit Lebensdauervorhersage verwendet. Da bei betriebsrelevanten (erhöhten) Temperaturen Langzeitversagen aufgrund von Kriecheffekten möglich ist wurden Kriechverhalten und Kriechversagenszeit charakterisiert. Zusätzlich wurden die mechanischen Belastungsgrenzen der dünnen Membranschicht und ihr Effekt auf die Substratstabilität betrachtet. Unterstützende numerische Simulationen zur Analyse der experimentell bestimmten mechanischen Eigenschaften wurden durchgeführt, da analytische Standardgleichungen (ASTM C 1499) auf ebene Einzelschicht-Proben begrenzt sind. Die hauptsächlich experimentell basierte Arbeit wurde zusätzlich durch numerische Simulationen unterstützt um das Membrandesign zu

optimieren und den Effekt der letztendlichen geometrischen Membanstrukturumsetzung (planar oder tubular) und des Schichtdickenverhältnisses zu erfassen.

Abstract

One of the most efficient ways to realize an Oxy-fuel process is the utilization of ceramic oxygen transport membranes (OTMs) for air separation, since this process provides a significantly lower efficiency loss compared to conventional cryogenic separation technologies. Driven by the difference in oxygen partial pressure, the oxygen transport takes place via oxygen vacancies in the crystal lattice of the membrane. Thin membrane layers supported by a porous substrate are considered as the most efficient design solution for such air separation units. The porous substrate should provide mechanical stability of the entire membrane structure. The operational temperatures are rather high, since the release of oxygen atoms from the lattice at elevated temperatures aids the transport processes. Due to their favorable permeation properties, which are an essential functional prerequisite, several materials were suggested as promising membrane and substrate materials, namely: $Ba_{0.5}Sr_{0.5}Co_{0.8}Fe_{0.2}O_{3-\delta}$, $La_{0.58}Sr_{0.4}Co_{0.2}Fe_{0.8}O_{3-\delta}$, $Ce_{0.9}Gd_{0.1}O_{1.95-\delta}$ and as alternative substrate material, the novel Fe21Cr7Al1Mo0.5Y alloy. The current study aims at the thermo-mechanical characterization and comparison of those materials.

Fundamental mechanical characteristics such as elastic behavior and fracture properties were evaluated to warrant the long-term functionality of these materials. However, the long-term reliability of the component does not only depend on its initial strength, but also on strength degradation effects. In particular, the sensitivity to environmentally enhanced crack propagation at subcritical stress levels was assessed and also used as a basis for a strength–probability–time lifetime prediction. Creep behavior and time to rupture were characterized, since at operation relevant (elevated) temperatures long-term failure may occur due to creep damage. The mechanical limit of the thin membrane layer and its effect on the stability of the substrate material was also addressed.

Complementary numerical simulations were carried out to permit an assessment of the experimentally obtained mechanical characteristics since standard analytical relationships (ASTM C 1499) are limited to flat mono-layer specimens. The mainly experimentally based work was additionally supported by numerical simulations to assess the effects of the final membrane´s geometrical arrangement (i.e. tubular and planar) and thickness ratios of particular layers, in order to optimize the membrane design.

Contents

1 INTRODUCTION

Continuously increasing population and industrial growth will lead to an increasing energy demand. It can be expected that one of the main energy sources in the forthcoming decades remains fossil fuel. The flue gases from their combustion are, however, widely recognized as a critical source of global warming, which is mainly attributed to air pollution with carbon dioxide [1]. In order to reduce the amount of CO_2 released into the atmosphere, the Kyoto protocol was developed and signed in 1997 by almost all world countries. The protocol commits the participating countries to reduce their collective greenhouse gas emissions over the five-year period 2008-2012 to an average of 5 % with respect to the 1990 levels [2].

One of the strategies developed to reduce CO_2 emissions is CCS (Carbon Capture and Storage [3]), illustrated in Figure 1-1. Instead of releasing CO_2 into air, the aim is to separate it from other exhaust gases and subsequently store it in a compressed, liquidized form in natural deep cavities.

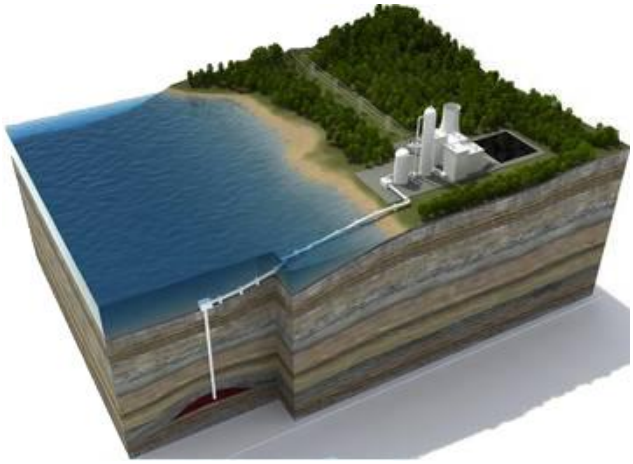

Figure 1–1: Carbon Capture and Storage [4].

Three different technological implementation routes for CCS power plants are currently under development, which are either based on post combustion treatment of the flue gas [5], or a treatment of the fuel before it reaches the burner, i.e. in the Oxy-fuel [6] and pre-combustion route [7]. The objectives of the present study aim at the Oxy-fuel process, in particular, ceramic oxygen transport membrane systems for air separation into N_2 and O_2 [8].

In the Oxy-fuel process, fossil is burned in pure oxygen. Therefore, the air has to be separated into pure oxygen and nitrogen. Oxygen is afterwards used to combust a carbon containing fuel (e.g. coal, gas, bio-gas) which produces exhaust gases consisting primarily of CO_2 and H_2O. As a result, final separation is rather simple since water is removed by condensation and the remaining CO_2 can be compressed and stored. The principle is schematically illustrated in Figure 1-2.

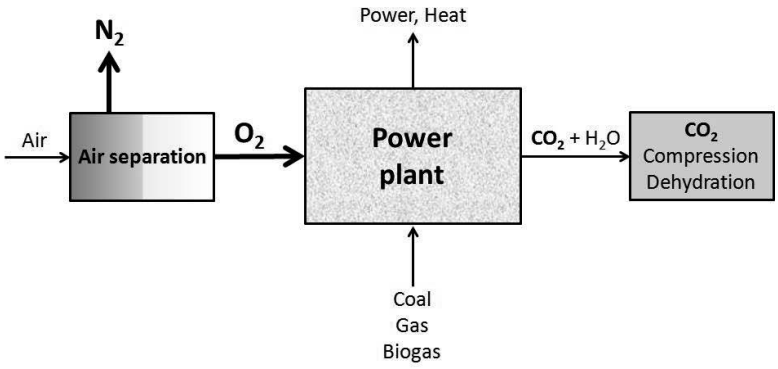

Figure 1–2: The Oxy-fuel process [9].

Based on the current state of knowledge it can be suggested that the most efficient way to realize an Oxy-fuel process is the utilization of ceramic oxygen transport membranes (OTM) for air separation, since this process provides a significantly lower efficiency loss compared to conventional cryogenic separation technologies [4]. The membrane needs to permit selective oxygen permeation from the feed (atmospheric or high pressure air) side to the permeate (low pressure) side. Since oxygen is transported through ceramics in an ionic state, the overall charge neutrality can only be maintained if electrons are conducted in the opposite direction. Therefore, only mixed ionic electronic conducting (MIEC) ceramics can be used as oxygen transport membrane materials. The oxygen transport in these materials takes place via oxygen vacancies in the crystal lattice. The operational temperatures are rather high, since the release of oxygen atoms from the lattice at elevated temperatures aids the diffusion processes.

An essential functional prerequisite of a material to be selected for oxygen transporting membranes is its oxygen permeation efficiency which is directly linked to the necessary

membrane area. Permeation rates of MIEC materials are in general (neglecting the surface limitations) inversely proportional to membrane thickness. Hence, thin membrane layers supported by a porous substrate are considered as the most efficient design solutions for such air separation units [10]. The technological implementation of this approach is based on a multi-layered membrane structure consisting of a thin, dense membrane layer, additional surface activation catalyst layers, and a thick porous substrate (Figure 1-3). Catalyst layers can be used to enhance oxygen permeation of thin membrane layers where surface exchange limitations take place [11]. The porous substrate should provide mechanical stability of the entire membrane structure, since the application-related loadings (due to thermal or chemical strains, pressure gradients between feed and sweep side, etc.) cannot be sustained by an unsupported thin membrane layer.

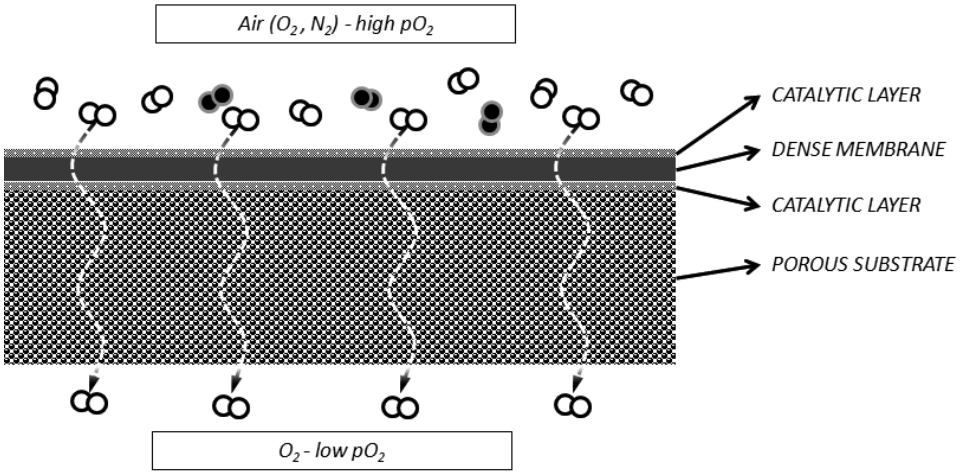

Figure 1–3: Membrane composite structure consisting of a porous substrate, dense membrane layer and catalytic layers. The schematic illustration is vertically over-scaled.

2 SCOPE OF THE WORK

The current study mainly concentrates on the thermo-mechanical characterization and lifetime prediction of porous substrates selected for the application in Oxy-fuel processes which should provide mechanical stability to the membrane structure. However, the influence and stability of the thin membrane layers is also assessed. Functional catalytic layers were not addressed since they are still under development.

The work was carried out within the framework of the "NAnostructured Surface Activated ultra-thin Oxygen Transport Membrane" project (NASA-OTM - NMP3-SL-2009-228701), supported by European Union in the 7th Framework Programme. Due to their favorable permeation properties, several materials were suggested as promising membrane and substrate materials, namely: $Ba_{0.5}Sr_{0.5}Co_{0.8}Fe_{0.2}O_{3-\delta}$, $La_{0.58}Sr_{0.4}Co_{0.2}Fe_{0.8}O_{3-\delta}$, $Ce_{0.9}Gd_{0.1}O_{1.95-\delta}$ and as alternative substrate material, the novel Fe21Cr7Al1Mo0.5Y alloy.

Under the severe conditions of real application, the stability of membrane materials is not only challenged by the high operating temperature (~ 850 °C), but also by pressure gradients across the membrane and chemically or thermally induced strains. Fundamental mechanical characteristics such as elastic behavior and fracture properties need to be evaluated to warrant the long-term functionality. Thermal stresses can arise due to differences in thermal expansion of the individual layers or temperature gradients along or across the entire layered structure. Chemical strains induce stresses due to lattice expansion associated with differences in oxygen partial pressure across the membrane layer. Hence, although membrane layer and porous substrate might consist of identical material, chemical strain can appear. In order to prevent failure, residual stresses need to be assessed. For substrates, residual stresses need to be balanced by the strength of materials for acceptable failure probabilities, whereas for the thin membrane layers an energy criterion appears to be more adequate and the energy release rate induced by residual stress should be compared to the fracture energy.

The long-term reliability of the component does not only depend on its initial strength, but also on strength degradation effects. In particular, environmentally enhanced crack propagation at subcritical stress levels, referred to as subcritical crack growth, can be important since this can

lead to a decrease of the in-service strength. The associated correlation between stress rate and strength is important to evaluate the effect of thermally induced stresses at the beginning of the start-up and at the end of the shut-down process and can be used as a basis for a strength–probability–time lifetime prediction. At operation relevant (elevated) temperatures, long-term failure may occur due to creep damage. Hence, creep rupture under tensile or combined tensile–compressive loads is an important aspect since during operation both, tensile and compressive stresses, act on the membrane components. Therefore, both lifetime related aspects were considered: failure at room temperature and operation relevant temperatures.

Complementary numerical simulations were carried out to permit an assessment of the experimentally obtained mechanical characteristics since standard analytical relationships (ASTM C 1499) are limited to flat mono-layer specimens. The mainly experimentally based work was additionally supported by numerical simulations to assess the effects of the final membrane´s geometrical arrangement (i.e. tubular and planar) and thickness ratios of particular layers, in order to optimize the membrane design.

3 LITERATURE REVIEW

In the following chapters information on the considered membrane materials, their development and motivation for their selection is given. Subsequently, the current knowledge on their mechanical properties is reviewed. Special attention is focused on lifetime prediction methodologies that are later used in the present study to predict the long-term reliability of the membrane composite.

3.1 Membrane materials

The development of membrane materials is mainly triggered by optimization of permeation and chemical stability under operation relevant conditions. Within the framework of the NASA-OTM project selected materials from two structure classes, perovskites and fluorite-oxides, were selected as the most appropriate candidates for the oxygen transport membrane application. Whereas the perovskites are advantageous with respect to their permeation properties, fluorite-structured materials feature a favorable chemical stability.

In the membrane assembly a dense membrane layer will be deposited on a porous support. The preparation route of the layered membrane composite is based on warm-pressing and subsequent co-sintering for laboratory specimens, whereas the industrial-relevant approach is tape-casting. Hence, depending on the materials development stage, specimens produced using both of these technologies were investigated. In order to minimize residual stresses, design solutions based on a combination of identical materials for membrane layer and porous substrate were favored. However, aiming at an alternative approach, cheaper metallic substrates with enhanced thermal shock stability were also considered.

The MIEC materials, considered as membrane layer and substrate and therefore investigated in the current study, are perovskite-structured $Ba_{0.5}Sr_{0.5}Co_{0.8}Fe_{0.2}O_{3-\delta}$ (BSCF) and $La_{0.58}Sr_{0.4}Co_{0.2}Fe_{0.8}O_{3-\delta}$ (LSCF), and the fluorite-structured $Ce_{0.9}Gd_{0.1}O_{1.95-\delta}$ (CGO). As an alternative substrate material, the high-temperature resistant, Fe21Cr7Al1Mo0.5Y (FeCrAlY) alloy was selected. The latter can be used as porous substrate for membrane layers produced from any of the MIEC materials considered above.

The particular advantage of BSCF is its high permeation [11]. However, it is not stable against CO_2 [12] and therefore can only be used in an Oxy-fuel process without flue-gas recirculation. LSCF has a lower permeation than BSCF [13,14,15], but is expected to be stable under CO_2 containing atmospheres.

Doped ceria is taken into consideration due to its chemical stability, which is generally significantly higher than that of perovskites [16]. Among all doped ceria materials, the selected CGO has the highest ionic conductivity [14].

The considered alumina-scale forming ferritic steel Fe21Cr7Al1Mo0.5Y was specifically developed as membrane substrate by the project partner DTU Energy Conversion (Roskilde, Denmark). Compared to ceramics, the ferritic steel is significantly cheaper and allows production of robust, thermo-shock and damage tolerant supports which can be easier integrated into modules (welding and brazing is possible). As alumina-former, it has a superior high-temperature corrosion resistance compared to other FeCr alloys, and should not exhibit Cr-poisoning problems [17].

3.1.1 Perovskites

Among the mixed-conducting ceramic membranes, perovskite-type ceramic membranes exhibit the highest oxygen permeability due to their high ionic and electronic conductivity [18]. BSCF and LSCF share this perovskite structure [16], which can be described with the crystal lattice of calcium titanium oxide $CaTiO_3$. The lattice is schematically shown in Figure 3-1. The general chemical formula of perovskite compounds is ABO_3, where A are large cations of alkaline earth or rare earth elements, B are small cations of transient metals or rare earth metals, and O are oxygen anions which bond to cations [19]. Contrary to other oxide structures, in which the oxygen anions usually form a closed-packed structure, perovskites are formed in closed-packed cubic structure by large A-cations and oxygen anions along with smaller, but highly charged B-cations [20]. Large A-ions are positioned at the unit corner sites, B-ions occupy the center, whereas oxygen ions are located at the face-centered positions. Accordingly, in the ideal cubic-symmetry structure, B-cations feature 6-fold coordination, surrounded by an octahedron of anions, and the A-cations possess 12-fold cuboctahedral coordination.

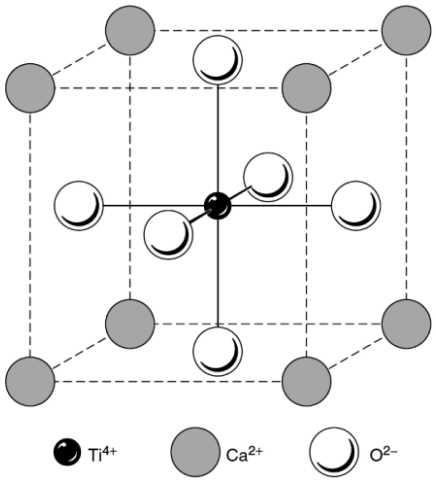

Figure 3–1: Ideal $CaTiO_3$ perovskite structure [21].

However, the structure of cubic symmetry usually exhibits some distortion. An imbalance induced distortion is caused by the different radii of the A- and B-cations. The degree of distortion can be defined by the Goldschmidt tolerance factor which is based on geometric considerations [22]:

$$t = \frac{r_A + r_O}{\sqrt{(r_B + r_O)}} \qquad 3.1$$

where r_A, r_B and r_O are the radii of the respective ions. Nominally, the perovskite structure should be stable for $1.0 < t < 0.75$ [23]. When the distortion becomes too large, other crystal symmetries such as orthorhombic and rhombohedral can appear. A tolerance value higher than unity implies that the A-cations are too large for the compound to adopt the ideal cubic perovskite structure. In these cases hexagonal perovskites in which octahedra share faces and form chains along the hexagonal *c*-axis are often formed [24].

BSCF development

In general, the membrane materials must possess a high oxygen permeability and good structural stability. Teraoka et al. [25,26,27] addressed these problems by developing high oxygen permeation membranes using the perovskite $SrCo_{0.8}Fe_{0.2}O_3$. Their high oxygen flux was attributed to the high concentration of oxygen vacancies in the lattice caused by the A-site substitution. As

outlined above, the phase structure of the perovskites is closely linked to the Goldschmidt tolerance factor [23]. Since cobalt and iron have multiple oxidation states, the tolerance factor can be tuned by varying temperature and oxygen partial pressure [28]. Assuming a most stable oxidation state of 3+ for both cobalt and iron ions, implies that the A-site cation (Sr^{2+}) of $SrCo_{0.8}Fe_{0.2}O_{3-\delta}$ is too small to sustain a perovskite structure with a cubic symmetry, which is believed to be the most stable conducting lattice symmetry for perovskites [29]. Since this material suffers from insufficient chemical and structural stability, research concentrated on compositions which might overcome these problems. Consequently, Shao et al. [30] adopted partial substitution of Sr^{2+} by the larger sized cation Ba^{2+} in order to increase the tolerance factor of the perovskite. It was found that substitution of 50 % of Sr^{2+} by Ba^{2+} which has a larger ionic radius but the same valence state as Sr [12] is the most promising composition and BSCF ($Ba_{0.5}Sr_{0.5}Co_{0.8}Fe_{0.2}O_{3-\delta}$) was proposed as a membrane material for oxygen separation. Experimental results confirmed that the phase stability of the membrane was remarkably improved while the oxygen permeation remained at a high level at elevated temperatures [12,31]. However, at temperatures below 850 °C, a significant decrease of the oxygen permeation with time was observed by Shao et al. [12]. They assigned this decrease to partial decomposition of the cubic to a hexagonal phase at intermediate temperatures. Their XRD investigations at 750 °C revealed the presence of $BaCoO_2$ as a secondary phase which is a product of the reaction:

$$Ba_{0.5}Sr_{0.5}Co_{0.8}Fe_{0.2}O_{3-\delta} \Rightarrow BaCoO_2 + SrCo_{0.6}Fe_{0.4}O_{3-\delta}$$

This hexagonal $BaCoO_2$ compound acts as a diffusional barrier and leads to a continuous decrease of oxygen permeation. The $SrCo_{0.6}Fe_{0.4}O_{3-\delta}$ compound is assumed to have brownmilerite structure formed at low oxygen partial pressures and therefore has not been found after annealing in air [32,33]. The permeation as a function of operational time for BSCF at different temperature is given in Figure 3-2.

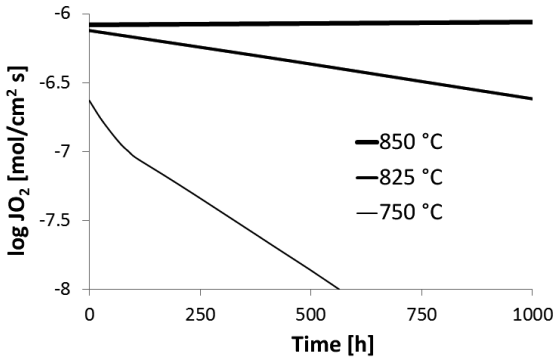

Figure 3–2: Oxygen permeation fluxes of BSCF as a function of operation time. The decrease of the flux at different temperatures is assigned to an increase of the hexagonal phase content [[12]].

A disadvantage of BSCF is its instability in CO_2 - containing environments which results in a decrease of oxygen permeation even at temperatures where no hexagonal phase forms. Schulz et al. [[34]] investigated $Ce_{0.2}Gd_{0.8}O_2$ coated BSCF membranes and found a strong influence of CO_2 on oxygen permeation for the BSCF material. The mixture of CO_2 and N_2 was used as a sweep gas, where the CO_2 amount was varied from 0 to 100 %. The influence of phase transformation occurring below 850 °C was ruled out since the tests were performed at 900 °C. For the environment containing 20 % of CO_2, uncoated BSCF exhibited a decrease of oxygen permeation of ~ 35 % (Figure 3-3), which did not occur in the case of coated BSCF. Such degradation effects were also observed in other reports [[35,36,37]].

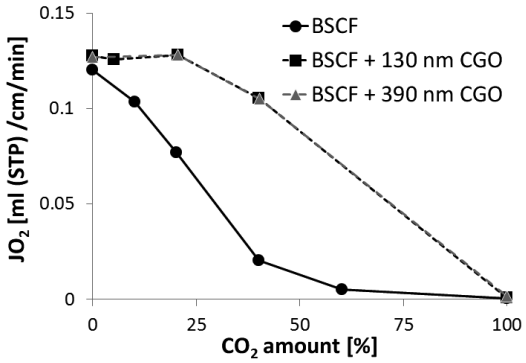

Figure 3–3: Oxygen permeation at 900 °C for coated and uncoated BSCF at different CO_2 concentrations applied during 4 hours dwell time at each concentration [[34]].

LSCF development

$La_{0.58}Sr_{0.4}Co_{0.2}Fe_{0.8}O_{3-\delta}$ has been mostly developed for the use as a cathode material in solid oxide fuel cells (SOFCs). It has a perovskite structure similar to BSCF. As reviewed above, the cation substitution leads to a range of possible variations in chemical composition. One possibility is the substitution of Sr by lanthanum (La), resulting in $LaCoO_{3-\delta}$. Since this increases ionic and electronic conductivity, La^{2+} seems to be the most appropriate dopant among alkaline-earth cations for lanthanum A-side cations. The similar ionic radii of La^{3+} and Sr^{2+} result only in an insignificant distortion. The change in electronic state due to cation substitution is balanced by creating oxygen vacancies and the partial conversion of Co^{3+} to Co^{4+} [26,38].

Extensive studies have been carried out on acceptor-doped oxides with the composition $Ln_{1-x}A_xCo_{1-y}B_yO_{3-\delta}$ (A can be Sr, Ba, Ca and B might be Fe, Cu, Ni; Ln with Ln either La, Pr, Nd, Sm or another lanthanide element) [26,39,40,41,42]. These materials are considered to be most promising for the application as oxygen separation membranes. The amount of substitution of A-site cations by lower valence metal ions is application oriented since it is basically a compromise between high oxygen permeation and phase stability. Higher amount of substitution leads to an increase of oxygen permeation flux. The widely studied $La_{1-x}Sr_xCo_{1-y}Fe_yO_{3-\delta}$ (LSCF) [39,40 ,43,44] series was found to be more stable and to exhibit only slightly lower ionic conductivity than the strontium-doped lanthanum cobaltite. Although it decreases the oxygen flux, doping with iron was found to be necessary to preserve the stability of the perovskite at higher strontium concentrations [26]. This decrease is related to the fact that oxygen diffusion is more difficult in the surrounding of Fe^{3+} ions since they have larger ionic radius and larger bonding energy to oxide ions than Co^{3+}.

According to Huang et al. [45], the rhombohedral symmetry of LSCF at low temperatures transforms to a cubic symmetry at elevated temperatures by a second order phase transition. The transition temperature depends on the doping amount. In case of $La_{0.58}Sr_{0.4}Co_{0.2}Fe_{0.8}O_{3-\delta}$, the transition temperature is about 750 °C in air. It has been verified that this transformation influences the mechanical properties [45].

Ellet investigated the temperature dependence of the oxygen permeation fluxes of $Ba_{0.5}Sr_{0.5}Co_{0.8}Fe_{0.2}O_{3-\delta}$ and $La_{0.58}Sr_{0.4}Co_{0.2}Fe_{0.8}O_{3-\delta}$ [46], which permits a direct comparison of

both materials (Figure 3-4). The tests were performed at 1 mm thick membranes in a temperature range from 700 °C to 950 °C. In both cases the fluxes increased with increasing temperature which is related to the increase in mobility and concentration of the oxygen vacancies [42]. Hence, these data prove that the higher stability of LSCF compared to BSCF goes along with a decrease in permeation.

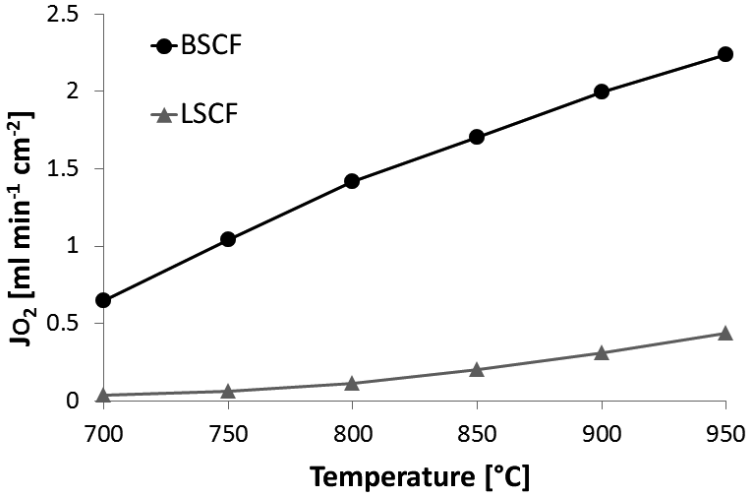

Figure 3–4: Oxygen permeation flux density of 1 mm thick $Ba_{0.5}Sr_{0.5}Co_{0.8}Fe_{0.2}O_{3-\delta}$ and $La_{0.58}Sr_{0.4}Co_{0.2}Fe_{0.8}O_{3-\delta}$ [46].

3.1.2 Fluorite - structured oxides

The fluorite structure, with the compound formula AO_2, consists of a simple cubic oxygen lattice with the body centers occupied by eight coordinated A-cations, and is termed after the CaF_2 structure (Figure 3-5). The unit cell is based on the face-centered cubic packing of cations [47]. The empty interstice is located in the center of the cubic anion lattice. Common materials which form this structure are uranium dioxide (UO_2), thorium dioxide (ThO_2), and cerium oxide (CeO_2). The latter has the calcium fluoride structure over the whole temperature range from RT to the melting point (approximately 2750 K) [48]. Ceria is also known to tolerate considerable reduction without phase change, especially at elevated temperatures [48].

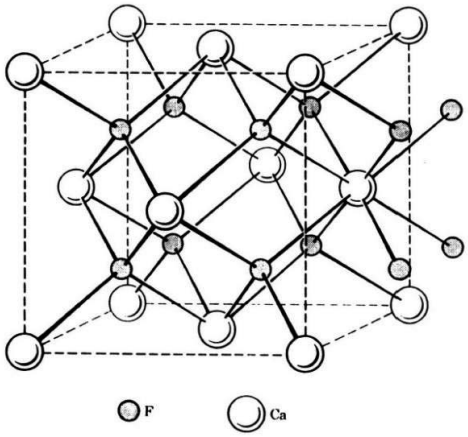

Figure 3–5: Fluorite structure of CaF_2 [21].

The fluorite structure is relatively open and it shows large tolerance for high levels of atomic disorder, which may be introduced by doping, reduction or oxidation [49]. Doping is usually realized by introducing lower valence cations into the lattice, resulting in additional oxygen vacancies to maintain the overall charge neutrality. Doping of the fluorite oxides is achieved by substitution of the host cation by either a rare or alkaline earth material.

CGO development

Cerium is the most abundant member of the element series known as lanthanides or rare earths. It has two stable valence states, Ce^{4+} known as ceric, and Ce^{3+} known as cerous. The ceric ion is a strong oxidizing agent but when associated with oxygen, it becomes completely stabilized [50].

Doped cerium oxide was initially developed for the use as an electrolyte in SOFCs [51,52,53]. Compared to the competitive material yttria stabilized zirconia, it has a low internal resistance in SOFCs operating at low temperatures due to higher ionic conductivity [54]. The disadvantage for SOFC application is its electronic conductivity. However, for membrane application, this material is favorable since it provides both, high ionic and sufficient electronic conductivity.

Dopants such as alkaline and rare-earth oxides have a large solubility in the Ce sub-lattice. In case of substituting the Ce^{4+} with divalent or trivalent cations, anion vacancies are created to compensate the lattice charge. Consequently, the fluorite structured doped cerium oxide exhibits

predominantly ionic oxygen conductivity over a large temperature and oxygen partial pressure range [55] and is therefore one of the most promising materials for membrane applications. The conductivity depends on the actual dopant. In particular, dopants with ionic radii close to that of the matrix material, such as gadolinium, yttrium and samarium, are considered to be most suitable [48].

Doped cerium oxide belongs to the MIEC (exhibits the mixture of ionic and electronic conductivity) materials group at low oxygen partial pressures. In reducing atmospheres, some oxygen ions are mobile in the lattice which leads to a reduction of Ce^{4+} to Ce^{3+}. This generates electrical carriers, oxygen vacancies and electrons, and therefore, both electronic and ionic conductivity are enhanced.

The chemical composition of the gadolinium doped CeO_2 is written as $Ce_{1-y}Gd_yO_{2-y/2-\delta}$, where δ is the stoichiometry deviation (oxygen deficit). Up to now, the optimal composition with respect to oxygen conductivity appears to be 10 mol % Gd^{3+} ion doped ceria ($Ce_{0.9}G_{0.1}O_{1.95-\delta}$) which received significant attention [56,55 ,57,48].

3.1.3 Fe21Cr7Al1Mo0.5Y

In addition to the ceramic materials, the ferritic steel Fe21Cr7Al1Mo0.5Y was selected in the present study as potential substrate material. Alloying elements that tend to stabilize ferritic structure are chromium, molybdenum and silicon [58]. Depending on the application, various elements might be added which then also affect the mechanical properties [59,60]. Chromium and aluminum can be added to increase the oxidation resistance. Molybdenum and vanadium improve the tempering resistance by formation of stable carbides. Manganese can be added to improve the elevated temperature processing behavior and to increase strength, toughness and hardening behavior, whereas silicon might be used as a deoxidizing agent in the melt. Silicon also contributes to hardening of the ferritic phase. Small additions of reactive elements (less than 0.5 %) such as Y, Hf, Zr, Ce or La (usually rare-earths) can further improve oxidation behavior [61,62,63,64]. Improved scale adhesion will result from the diffusion of reactive elements to the metal/oxide scale interface and will limit the development of voids which might lead to scale spallation. These elements also prevent sulphur segregation at the interface, which could reduce the activation energy for void growth within segregation affected regions [65].

High temperature alloys should form Cr_2O_3 or Al_2O_3 scales to prevent fatal corrosion (i.e. formation of iron oxides) [58]. In case of FeCrAl alloys, an alumina scale provides corrosion resistance and makes the material suitable for high temperature application in a wide range of aggressive media in the chemical and process plant industry. This oxide scale serves as a diffusion barrier and protects the alloy from progressive oxidation. If the scale is damaged by abrasion or scratching, healing occurs almost immediately [58]. The protective effect of the scale depends on the oxide phase composition and the thickness of the initial scale. The most preferable aluminium oxide phase is α-Al_2O_3 (formed over 1000 °C) as it is slowly growing and chemically inert and more stable than the "transient" alumina phases formed at lower temperatures [65]. In order to provide long-term corrosion protection, the alumina scale needs to adhere well (as spallation and regrowth of the scale eventually leads to Al-depletion). Pre-oxidation, forming a thin protective scale of pure α-Al_2O_3 before the alloy is exposed to the application conditions, has shown to be a very effective method of increasing lifetime of FeCrAl alloys [66,67]. A reduction of sulphur content in the alloy has also been suggested as an advantageous pre-treatment [66,67]. Bennet et al. [68] showed that pre-oxidation of FeCrAl alloys by gas annealing has the most beneficial effect at operational temperatures around 900 °C.

Porous metal structures have been developed for various industrial applications [69,70]. Porous metal components differ from metal foams (with closed porosity) as they require interconnected porosity, and are formed using powder metallurgy routes. The long-term corrosion stability of porous steel structures is often poor due to their high specific surface [70]. Strategies for increasing the lifetime of such components are to ensure an adequate Al reservoir (high Al content), good scale adhesion, and formation of a thin protective α–Al_2O_3 scale by pre-oxidation [65].

A novel composition based on doping FeCrAl alloy with molybdenum and yttrium was investigated within the NASA-OTM project [65]. The alumina-forming alloy was chosen due to its higher stability at high temperatures compared to chromia-formers and the protective alumina scale that limits oxidation and also prevents Cr poisoning of the active ceramic layers [71].

3.2 Mechanical characteristics

High pressure and temperature gradients, as well as thermal expansion mismatches, induce stresses in a layered membrane structure. An assessment of stresses and deformation under thermal cycling and steady state operational relevant conditions requires thorough knowledge of deformation and fracture behavior of the membrane composite components. For long-term application, also the influence of environmental conditions on the strength and possible creep deformation and creep damage need to be investigated. In the following sections, basic principles and theoretical backgrounds of the mechanical investigations performed within the present study are introduced, and a review on the current literature on the considered classes of membrane materials is given.

3.2.1 Elastic behavior

An accurate knowledge of the elastic properties is of high importance since it provides basic data for analytical and numerical modeling of the stress states. Elastic properties of uniaxially loaded isotropic materials can be represented by the elastic modulus E as a material´s resistance to elastic deformation. It is defined using Hooke´s law as the ratio of stress to strain during elastic loading:

$$E = \frac{\sigma}{\varepsilon} \qquad 3.2$$

where σ is the applied stress and ε is the strain.

Elastic moduli can be determined with different methods. For brittle materials, uniaxial and biaxial bending tests are widely used. As macroscopically non-destructive method, micro-indentation is also commonly used.

The three-point bending test [72] is a widespread method for analyzing material´s behavior where material´s associated clamping problems do not permit tensile testing [72]. The alignment is easily achieved and specimens with simple geometric shapes can be used. The disadvantage of this method is that the maximum stress is laterally and vertically inhomogeneous and the specimen edges need to be well prepared to avoid any influence of cutting induced defects.

Contrary to the three-point bending test, the stress distribution in a biaxial ring-on-ring test [73] is not influenced by such edge effect. In particular, symmetrical and approximately constant equibiaxial maximum stress occurs on the tensile surface opposite to the area enclosed by the loading ring. The disadvantage of this test is the influence of the specimen unevenness and frictional effects on stress distribution [73].

Micro-indentation test [74] is also commonly used for measuring elastic moduli. The investigations can be performed with various indentation tips, e.g. Vickers [75], in which the diagonals of pyramidal tip enclose an angle of 136°. The advantage of this method is its macroscopic non-destructiveness and the use of a very small surface area during the investigation.

Literature data for elastic moduli of BSCF with various porosities are given in Table 3-1.

Table 3-1: Elastic moduli of BSCF as a function of temperature and porosity.

Composition	Elastic modulus [GPa]	Temperature [°C]	Test method	Ref.
$Ba_{0.5}Sr_{0.5}Co_{0.8}Fe_{0.2}O_{3-\delta}$ (porosity 5 %)	72	RT	Indentation	[45]
	63	RT	Ring-on-ring	
	45	200		
	52	400		
	48	800		
$Ba_{0.5}Sr_{0.5}Co_{0.8}Fe_{0.2}O_{3-\delta}$ (porosity 8 %)	52	RT	Ring-on-ring	[76]
$Ba_{0.5}Sr_{0.5}Co_{0.8}Fe_{0.2}O_{3-\delta}$ (porosity 38 %)	38	RT	Indentation	[77]
	33	RT	Ring-on-ring	
	27	200		
	27	400		
	29	600		
	27	800		

Huang at al. thoroughly studied the elastic modulus as a function of temperature for $Ba_{0.5}Sr_{0.5}Co_{0.8}Fe_{0.2}O_{3-\delta}$ [78]. They reported an elastic modulus of 63 GPa at RT and, contrary to

the commonly expected decrease with temperature of this property for ceramic materials, found a local minimum value at ~ 200 °C, followed by an increase to a local peak value at ~ 400 °C, and a slight decrease thereafter up to 800 °C. They assigned this anomaly up to ~ 400 °C to spin transition effects. Lipinska-Chwalek et al. studied the mechanical properties of porous BSCF as a function of temperature [77]. They compared their results with the data of dense BSCF in the work by Huang et al., and found similar behavior of the normalized elastic moduli (Figure 3-6). Both groups additionally carried out indentation tests and obtained slightly higher values at RT compared to the ring-on-ring test.

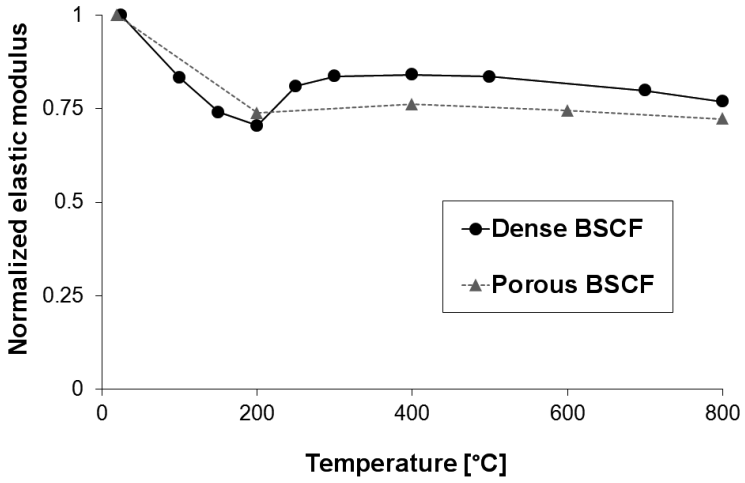

Figure 3–6: Normalized elastic moduli of porous and dense BSCF as a function of temperature [77]. Increase above 200 ° C is assigned to a spin transition.

Elastic moduli of several materials similar to LSCF were found in literature. Table 3-2 compiles the data with the corresponding testing temperature and method. All data are for dense material (porosity lower than 10 %). Data for porous materials were not available.

Table 3-2: Elastic moduli of materials similar to LSCF.

Composition	Elastic modulus [GPa]	Temperature [°C]	Test method	Ref.
$LaCoO_3$	83	RT	4-point bending	[79]

$LaFeO_3$	213	RT	4-point bending	[80]
$La_{0.8}Sr_{0.2}CoO_3$	86	RT	4-point bending	[79]
$La_{0.8}Sr_{0.2}Fe_{0.8}Co_{0.2}O_3$	161	RT	Resonant ultrasound spectroscopy	[81]
$La_{0.6}Sr_{0.4}Fe_{0.8}Co_{0.2}O_3$	152	RT	Resonant ultrasound spectroscopy	[81]
$La_{0.4}Sr_{0.6}Fe_{0.8}Co_{0.2}O_3$	167	RT	Resonant ultrasound spectroscopy	[81]
$La_{0.58}Sr_{0.4}Fe_{0.8}Co_{0.2}O_{3-\delta}$	78	RT	Ring-on-ring	[82]
	62	200		
	63	400		
	67	600		
	70	700		
	115	800		

Elastic modulus of $LaCoO_3$ is determined to be 83 GPa at RT [79]. Substitution of Co with Fe increases the elastic modulus by almost three times [80]. The substitution of 20 % La by Sr resulting in lanthanum cobaltite oxide does not significantly change the elastic properties [79], similar as in the case of LSCF when the La-Sr ratio is varied [81].

Huang et al. [45] studied the elastic modulus of LSCF in a temperature range from RT to 800 °C. They found that the load-displacement behavior is non-linear between RT and 700 °C, and linear at 800 °C, and assigned this effect to ferro-elasticity of the rhombohedral phase, which does not exist in the cubic symmetry at higher temperatures. The load-displacement curves are shown in Figure 3-7.

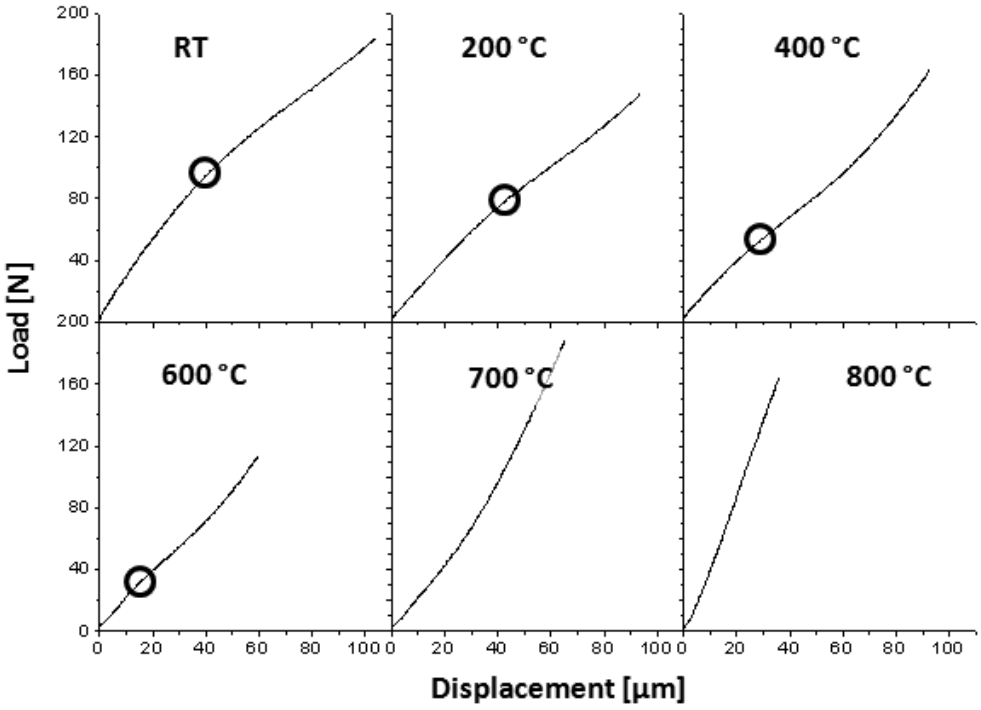

Figure 3–7: Typical load-displacement curves of LSCF at various temperatures [45]. The beginning of non-linearity is indicated by circles.

Yasuda et al. [83] investigated the mechanical properties of $Ce_{0.9}Gd_{0.1}O_2$ produced at different sintering temperatures. Increasing the sintering temperature led to a densification up to 1200 °C, above this temperature the density decreased. They assumed that this effect is a result of pore formation at 1300 °C and 1400 °C since non-stoichiometric phases of ceria that release oxygen are generated at these temperatures. Using 4-point bending test they showed (Figure 3-8) that the elastic modulus decreases with increasing sintering temperature from 1200 °C to 1400 °C, which they assigned to a change of porosity.

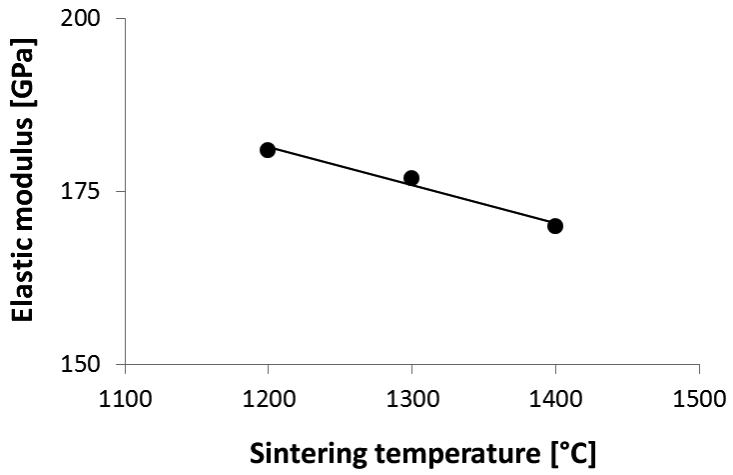

Figure 3–8: Elastic modulus of CGO decreasing with sintering temperature in a range of 1200 – 1400 °C [83].

Reports on the elastic moduli of various FeCr alloys can be found in literature [84,85,86]. Some of them are compiled in Table 3-3. In all cases the elastic modulus at RT was determined to be ~ 180 GPa with a constant decrease with temperature (Figure 3-9). The data reported by Schweda [84] are slightly lower and show a rather large scatter at elevated temperatures.

Table 3-3: Elastic moduli of FeCr alloys as a function of temperature for various chemical compositions.

Composition	Elastic modulus [GPa]	Temperature [°C]	Test method	Ref.
FeCr alloy *(Fe rest, Cr 21.8 %, Al 4.84 %, Y < 0.005 %, Mg < 0.005 %, Ti 0.013 %)*	147	RT	Tensile test	[84]
	135	200		
	100	400		
	93	600		
	27	800		
	12	1000		
MA956 *(Fe rest, Cr 19.6 %, Al 4.39 %, Y 0.34 % (Y_2O_3), Mg < 0.005 %, Ti 0.38 %)*	180	RT	Tensile test	[85]
	170	200		
	145	400		
	125	600		
	110	800		
	75	1000		
X10CrAlSi18 (1.4742) *(Fe rest, Cr 17-19 %, Al 0.7-1.2 %, C < 0.12 %, Si 0.7-1.4 %, Mn < 1 %, P < 0.04 %, S < 0.015 %)*	191	RT	Tensile test	[86]
	182	200		
	167	400		
	145	600		

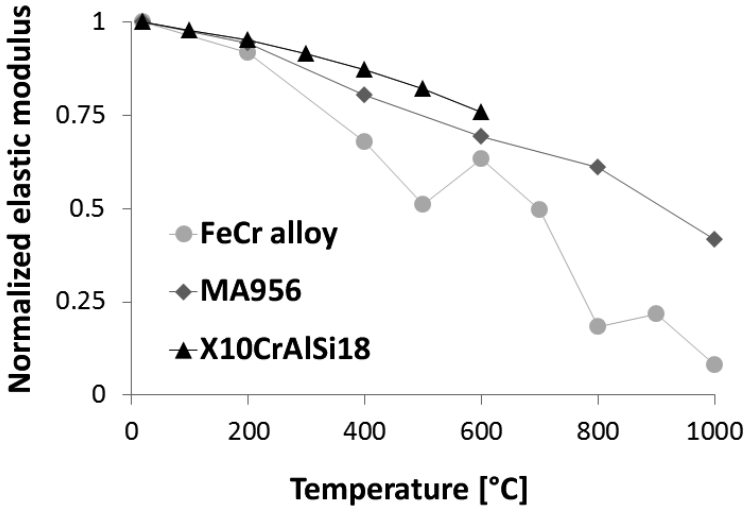

Figure 3–9: Normalized elastic moduli values for typical FeCrAl alloys [84,85,86] revealing a monotonous decrease with temperature. The lines are a guide to the eye.

3.2.2 Strength, strain and reliability

Usually, brittle materials exhibit large statistical variation in fracture stresses since the failure is initiated by defects. Hence, the strength needs to be statistically analyzed and related to a certain failure probability and in addition related to a specific effectively deformed area or volume. A larger sample will fail at a lower stress since it is more likely that it will contain a larger flaw. Furthermore, ceramic materials are typically stronger in bending than in tension, since in bending the highest tensile stress is localized at the surface, whereas in tension the entire sample is under homogeneous stress leading to a larger deformed volume.

The statistical distribution and hence the failure probability as a function of stress is commonly described by a two-parameter Weibull distribution [87]:

$$P_f(V_0) = 1 - exp\left[-\left(\frac{\sigma}{\sigma_0}\right)^m\right] \qquad 3.3$$

where σ_0 and m are constants, termed characteristic strength and Weibull modulus, respectively. If $\sigma = \sigma_0$ then $P_f(V_0)$ is equal to 0.632. Therefore, the characteristic strength σ_0 is the stress at

which 63.2 % of the samples will fail. The Weibull modulus reflects the correlation of fracture stress and failure probability.

As mentioned above, the failure probability depends on the tested effective volume or area, depending if volume or surface defects are failure relevant. A large component used in real application will have lower strength than a test specimen for the same failure probability. The correlation can be described using the relationship [88]:

$$\frac{\sigma_2}{\sigma_1} = \left(\frac{V_1}{V_2}\right)^{\frac{1}{m}} \qquad 3.4$$

where V_1 and V_2 represent the effective volume of specimen and component, respectively.

The Weibull modulus is generally biased by the number of specimens. The bias can be eliminated by increasing the number of tested specimens. According to ISO 20501:2003(E), an unbiased estimate is obtained by multiplying the calculated Weibull modulus by a correction factor. Tabulated values of correction factor as a function of tested specimen number can be found in the ISO 20501:2003(E). Contrary to significant influence of statistical bias on Weibull modulus, the bias associated with the characteristic strength can be neglected since, according to ISO 20501:2003(E), 20 specimens reduce the bias already to less than 0.3 %.

The standard deviation of Weibull modulus s_m and characteristic strength s_{σ_0} can be estimated in dependence of the number of specimens n, using the equations [89]:

$$s_m = \frac{m}{\sqrt{n}} \qquad 3.5$$

$$s_{\sigma_0} = \frac{\sigma_0}{m\sqrt{n}} \qquad 3.6$$

Characteristic fracture strengths were found for similar materials as in the case of the elastic modulus. Since the fracture strength can depend on several experimental parameters, such as test method, effective stress volume, specimen geometry, porosity, surface conditions, etc., a comparison might lead to misleading conclusions and hence most data are not discussed in detail. The values of materials similar to that considered in the present work are compiled in Table 3-4.

Table 3-4: Fracture strength of materials similar to these selected in the current study.

Composition	Fracture strength [MPa]	Temperature [°C]	Test method	Ref.
$Ba_{0.5}Sr_{0.5}Co_{0.8}Fe_{0.2}O_{3-\delta}$ (porosity 5 %)	100	RT	Ring-on-ring	[78]
	57	200		
	50	400		
	67	500		
	77	700		
	79	800		
$Ba_{0.5}Sr_{0.5}Co_{0.8}Fe_{0.2}O_{3-\delta}$ (porosity 8 %)	86	RT	Ring-on-ring	[76]
$Ba_{0.5}Sr_{0.5}Co_{0.8}Fe_{0.2}O_{3-\delta}$ (porosity 38 %)	34	RT	Ring-on-ring	[77]
	31	200		
	29	400		
	36	600		
	52	800		
$La_{0.58}Sr_{0.4}Co_{0.2}Fe_{0.8}O_{3-\delta}$	70	RT	Ring-on-ring	[90]
	61	200		
	66	400		
	80	700		
	132	800		

Huang et al. [78] and Lipinska-Chwalek et al. [77] found that for both, dense and porous BSCF, the fracture strength has a local minimum value at ~ 400 °C and increases at higher temperatures. A similar tendency was also found for dense LSCF, where the local minimum appeared at ~ 200 °C. The curves are shown in Figure 3-10. The origin of this anomaly might be again associated with spin transitions.

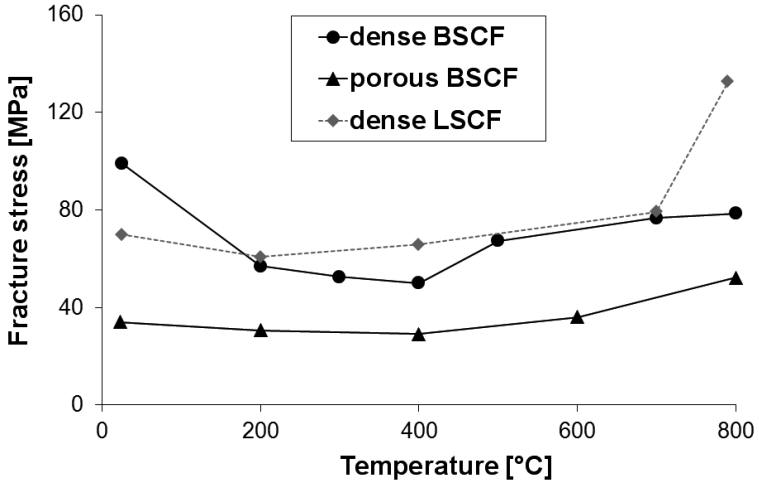

Figure 3–10: Fracture stress of BSCF and LSCF as a function of temperature [78,77].The lines are a guide to the eye.

Similar as for the elastic modulus of $Ce_{0.9}Gd_{0.1}O_{2,}$ Yasuda et al. [83] reported a decrease of fracture strength with sintering temperature in the range from 1200 °C to 1400 °C (Figure 3-11). They assigned this effect to an increase in porosity.

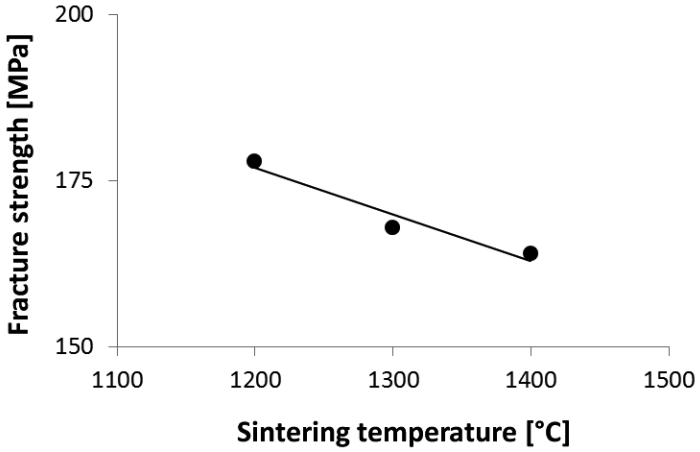

Figure 3–11: Decrease of the fracture strength of CGO with increasing sintering temperature in a range of 1200 – 1400 °C [83].

Literature data on mechanical properties of FeCrAlY alloys are currently not available. Therefore, data for the similar FeCr alloy reported by Schweda [84] are used for comparison. Schweda et al. analyzed the strength of this FeCr alloy in a temperature range from RT to 1000 °C. He found that both, yield stress and tensile strength rapidly decrease above 500 °C (Figure 3-12).

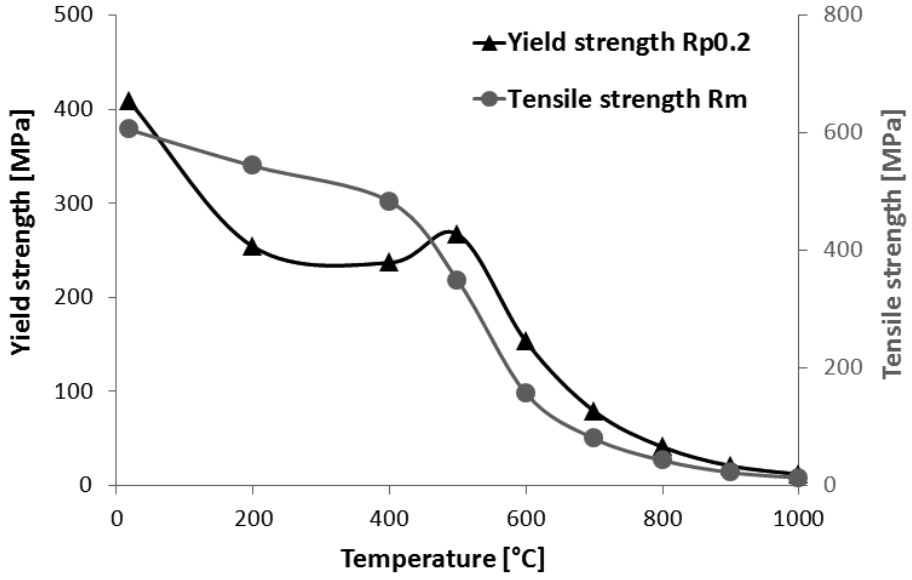

Figure 3–12: Yield strength and tensile strength of a FeCr alloy as a function of temperature [84]. The lines are a guide to the eye.

3.2.3 Subcritical crack growth

Subcritical crack growth (SCG) progressing from defects can be caused by mechanical loading combined with a chemical interaction of the ceramic material with the environment. Moist or corrosive atmosphere might cause chemical reactions which result in a structural weakening [91]. For example, water or water vapor can reach the crack tip, react and break the structural bonds. This effect is enhanced by mechanical stresses. A schematic illustration is given in Figure 3-13.

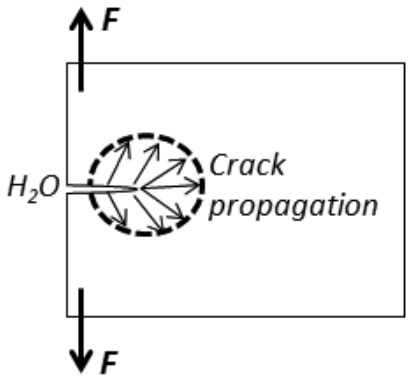

Figure 3–13: Chemical reaction causing the subcritical crack growth.

According to ASTM C 1465, the subcritical crack growth rate v is governed by an empirical power-law crack velocity:

$$v = A\left(\frac{K_I}{K_{IC}}\right)^n \qquad 3.7$$

where A is a constant, K_I is mode I stress intensity factor, K_{IC} is fracture toughness under mode I condition, and n is the subcritical crack growth exponent. In a test with constant stress rate, the characteristic fracture strength σ_0 can be correlated with the stress rate $\dot{\sigma}$ using the equation [92]:

$$log\,\sigma_0 = \frac{1}{n+1} log\,\dot{\sigma} + log\,D \qquad 3.8$$

where D is the SCG constant. As a consequence of this effect, characteristic fracture strength depends on the stress rate for materials sensitive to subcritical crack growth. Bending tests performed with different stress rates permit an experimentally straight forward way to assess the sensitivity to subcritical crack growth [47,92]. An example of such an evaluation of subcritical crack growth is given in Figure 3-14 for alumina. The plot illustrates the measured strength values as a function of stress rate. If a material is sensitive to subcritical crack growth, the fracture strength will strongly decrease with decreasing stress rate, since subcritical crack growth leads to an increase of defect size already during the test and therefore reduces the fracture stress. However, it is shown in [93] that the Weibull modulus of specimens that failed in subcritical

crack growth experiments is related to the Weibull modulus obtained from inert strength tests under identical loading rates by:

$$m_{SCG} = m_{INERT} \cdot \frac{n+1}{n-2} \qquad 3.9$$

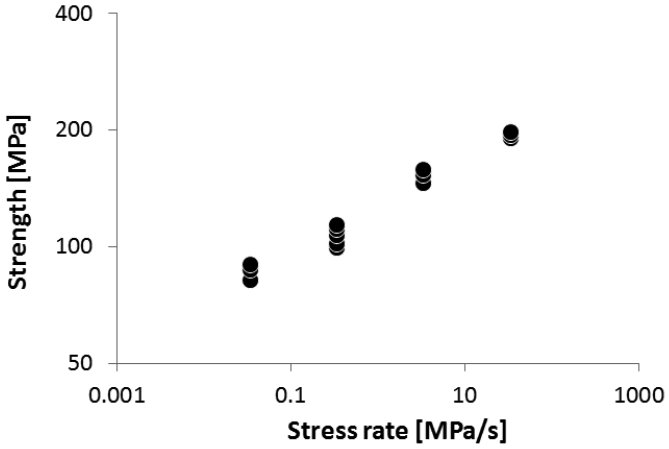

Figure 3–14: Effect of subcritical crack growth on the fracture strength of 96 % pure alumina tested in air at 1000 °C [92].

Subcritical crack growth phenomena are mostly observed for glassy materials, but can also affect oxide ceramics. No results regarding BSCF, LSCF and CGO were found in literature.

3.2.4 Fracture energy criterion

The fracture energy criterion was formulated first by Griffith [94]. He stated that a crack in a strained elastic body will propagate if the energy released during crack propagation is equal or higher than the energy necessary for creating a new surface:

$$G \geq Gc \qquad 3.10$$

where G refers to the energy released per unit area of crack and is called energy release rate, and Gc is the critical energy release rate. The latter is a material parameter determined experimentally from fracture tests, in particular, from the fracture toughness K_{Ic} [95,96,97], since:

$K_{Ic} = \sqrt{G_c E}$ (plane stress) *3.11* a)

$K_{Ic} = \sqrt{\frac{G_c E}{1-\nu^2}}$ (plane strain) *3.11 b)*

where E is the elastic modulus and ν is the Poisson´s ratio. In case of an infinite plate of unit thickness, containing a crack of finite length $2a$ perpendicular to a uniaxial stress field σ, the energy release rate G is given by:

$$G = \frac{\pi \sigma^2 a}{E} \qquad 3.12$$

Since the membrane layer is some orders of magnitude thinner than the porous substrate, it can sustain extremely high residual stress even for small differences in thermal expansion. The residual stresses can therefore easily be higher than their fracture strength but failure will only occur if also the energy release rate exceeds the critical value. The thermally induced residual stresses increase with increasing temperature difference from deposition temperature. Furthermore, even if dense membrane and porous substrate are made of the same material, residual stresses might appear due to chemical strains caused by the difference in oxygen partial pressure across the composite thickness [[98]]. The following relationship has been proposed for determining the energy release rate in bi-axially stressed thin layers [[99]]:

$$G = \frac{t_{mem} {\sigma_{mem}}^2}{Z\, E_{mem}} (1 - \nu^2) \qquad 3.13$$

where t_{mem} is the membrane thickness, σ_{mem} is the maximum membrane (residual) stress, ν is the Poisson´s ratio, and Z is the non-dimensional constant which depends on the failure mode [[99]]. The layer thickness and residual stresses are clearly important parameters which should be considered during membrane design since Equation (3.13) indicates their direct influence on failure. Compressive stresses are preferable since in that case the non-dimensional Z- constant for delamination will be almost an order of magnitude higher than for the formation of segmentation cracks.

Hendriksen et al. [[95]] analyzed several different material combinations in a bi-layered structure. Using Equation (3.13) they predicted that a critical TEC mismatch of $1 \cdot 10^{-6}$ K^{-1} can lead to membrane failure by surface cracking. The prediction was verified experimentally for several

materials, where for $0.1 \cdot 10^{-6}$ K^{-1} no failure was found. The surfaces and associated fracture features of several membrane layers are shown in Figure 3-15.

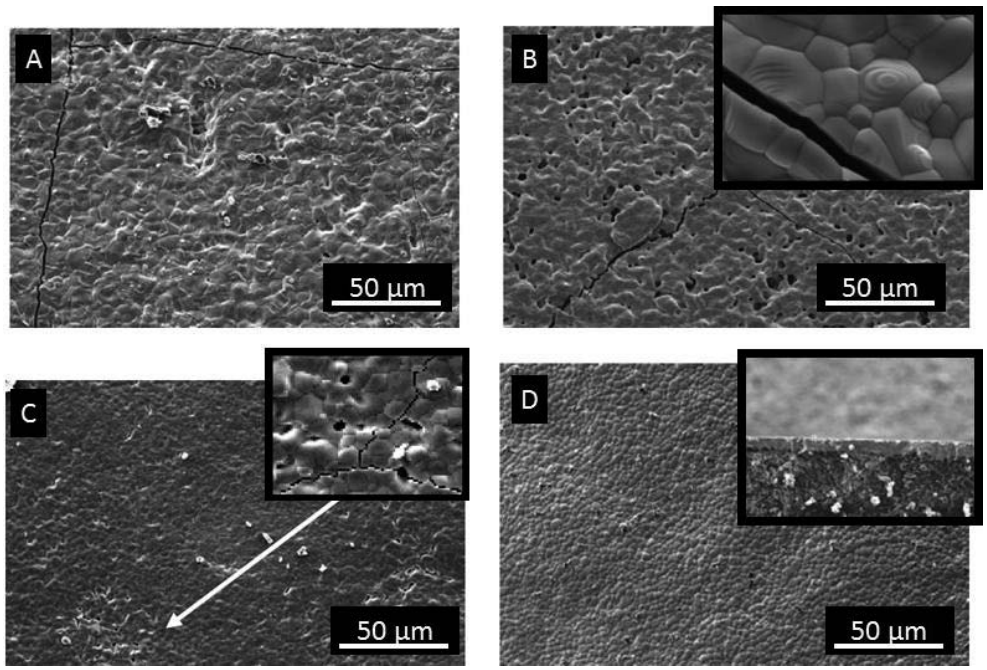

Figure 3–15: Top views of membrane structures with different TEC mismatches [95]. Cracks are visible for material combinations with TEC mismatch of a) $5 \cdot 10^{-6}$ K^{-1}, b) $4 \cdot 10^{-6}$ K^{-1}, c) $1.6 \cdot 10^{-6}$ K^{-1}. In case of d) where TEC mismatch is $0.1 \cdot 10^{-6}$ K^{-1}, no cracks were found.

3.2.5 Creep

One of the most critical factors determining the integrity of components exposed to elevated temperatures can be the time-dependent, thermally assisted plastic deformation under constant load (stress), known as creep [100]. As a consequence of such deformation, unacceptable dimensional changes and distortions, as well as rupture can occur [101]. Most materials exhibit primary, secondary and tertiary creep, as illustrated in Figure 3-16. The shape of the creep curve is determined by several competing reactions, including strain hardening, softening processes such as recovery, recrystallization and strain softening, and damage processes such as cavitation

and cracking, and in case of tensile loads specimen necking [102]. Strain hardening tends to decrease the creep rate, whereas the other factors tend to increase the creep rate.

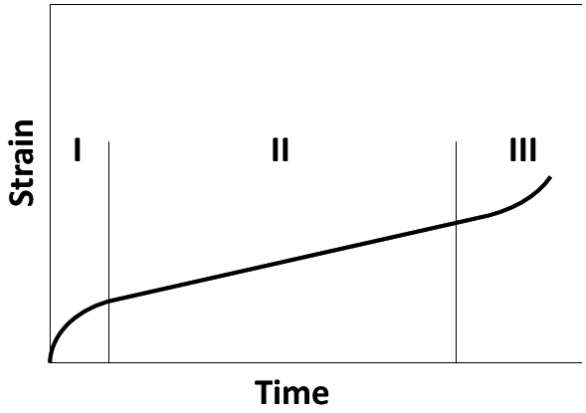

Figure 3–16: Creep stages: I primary, II secondary (minimum), and III tertiary.

Although several mechanisms are proposed, in general three mechanisms are governing creep behavior: diffusion, dislocation movement and grain-boundary sliding [103].

Diffusional creep is driven by the motion of single atoms or ions either by lattice diffusion (Nabarro-Herring creep [104,105]) or by grain-boundary diffusion (Coble creep [106]). When this creep mechanism is dominating, the steady-creep rates are postulated to correlate approximately linearly with stress. The flow of atoms (cations) is envisaged to occur from regions of local compressive stress toward regions of local tensile stress, balanced by a counter-flow of vacancies in the opposite direction. This results in a permanent strain of the material. The shorter bulk diffusion distance for structures with smaller grain size results in higher creep rates. A schematic illustration of the Nabarro-Herring creep mechanism is shown in Figure 3-17.

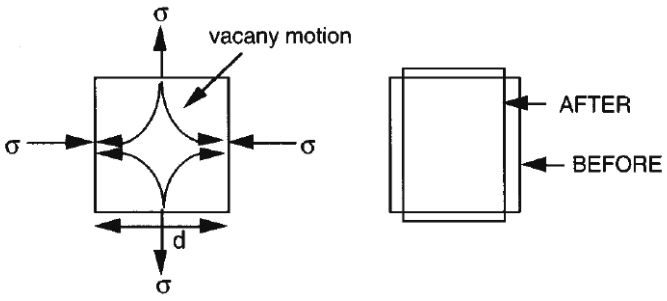

Figure 3–17: Lattice diffusion induced by the combination of tensile and compressive stresses [103]. The curved arrows indicate direction of vacancy motion. The diffusion leads to permanent strain (right image).

For Coble creep, diffusion occurs along the grain boundaries. Hence, the Nabarro-Herring creep is controlled by the lattice diffusivity D_L, and Coble creep by the grain boundary diffusivity D_G. In the latter case, it is necessary to define the grain boundary width d_G since in this case creep depends on d_G^{-3}. Since the diffusion involves more than one ionic species, the creep rate depends on the diffusion behavior of the slowest moving ions. Both mechanisms are illustrated in Figure 3-18.

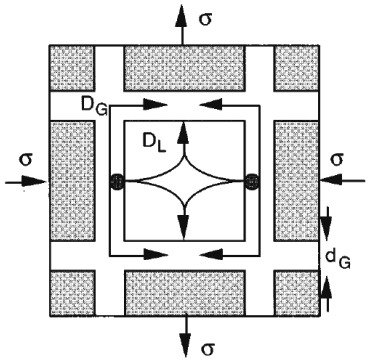

Figure 3–18: Stress induced diffusion paths for Nabarro-Herring (D_L) and Coble creep (D_G). The curved arrows indicate atom motions [103].

Dislocation creep is controlled by the motion of dislocations which occurs via dislocation glide and climb [47], which is usually impeded by a variety of obstacles. In this case, a short range

diffusion process is required which allows the dislocation to move to an adjacent slip plane [103]. Dislocation creep is not influenced by the grain size [107] and usually occurs in metals at relatively low temperature and high stress [47].

Grain boundary sliding occurs in ceramic materials which have sufficient amount of glassy phase that aid densification in the fabrication process. The softening of this phase at high temperatures allows deformation by grain boundary sliding.

According to [103], the effect of the creep mechanisms can be qualitatively correlated with grain size, applied stress and operational temperature (Figure 3-19). The creep rate contributions associated with the various mechanisms are considered to be independent, and the overall creep rate can be associated with the dominant mechanism.

Contrary to dislocation creep that predominates at high stresses, low stresses promote diffusional creep. At lower temperatures (and finer grain size), Coble creep is known to dominate over Nabarro-Herring creep. In general, the creep rate decreases with grain size, and increases with temperature.

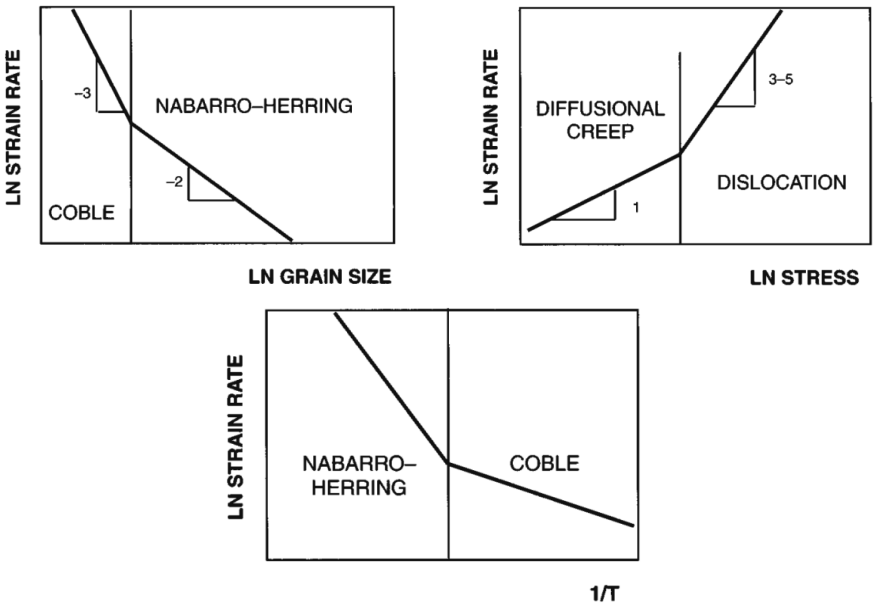

Figure 3–19: Correlation of creep - parameters and - mechanisms (schematic) [103].

Except for the linear dependency in the case of diffusional creep, creep varies nonlinearly with stress, either as a power law or an exponential function of stress. Norton and Bailey [108] proposed the relationship:

$$\dot{\varepsilon} = A\,\sigma^n \qquad 3.14$$

where A and n are stress-independent constants. The constant n usually lies between 1 and 8 [47]. For values higher than 1, creep is commonly referred to as power law creep. Note that the n parameter in the creep equation should be distinguished from the SCG n parameter (section 3.2.3). Since creep is a thermally activated process, its temperature sensitivity is expected to follow an Arrhenius law, with a characteristic activation energy Q for the rate-controlling mechanism. Hence, Equation (3.14) can be expanded to [107,109]:

$$\dot{\varepsilon} = A\,\sigma^n\,exp\,(-\frac{Q}{R\,T}) \qquad 3.15$$

where R is the universal gas constant. Although n and Q are expected to be constant, changes of the creep mechanism might lead to discontinuities in the ε - σ curve [110] (see Figure 3.19). Whereas steady state creep can be characterized by the above relationship, creep rupture occurs by the nucleation and stable growth of cracks followed by unstable crack growth.

Selected membrane materials have been extensively investigated with respect to their creep behavior since it is one of the key parameters to define their lifetime limits. Creep rates of materials for membrane application are compiled in Table 3-5 with the corresponding applied stresses and temperatures.

Table 3-5: Creep rates of various potential membrane materials.

Composition	Stress [MPa]	Temperature [°C]	Conditions	Creep rate [s^{-1}]	Ref.
$Ba_{0.5}Sr_{0.5}Co_{0.8}Fe_{0.2}O_{3-\delta}$	20	900	air	$3.1 \cdot 10^{-8}$	[110]
		950		$1.4 \cdot 10^{-7}$	
	30	700		$1.2 \cdot 10^{-9}$	
		800		$1.5 \cdot 10^{-9}$	
		850		$2.3 \cdot 10^{-9}$	
		900		$4.9 \cdot 10^{-8}$	
		950		$2.6 \cdot 10^{-7}$	
	63	900		$1.6 \cdot 10^{-7}$	
		925		$4.5 \cdot 10^{-7}$	
		950		$1.3 \cdot 10^{-6}$	
$La_{0.58}Sr_{0.4}Co_{0.2}Fe_{0.8}O_{3-\delta}$	20	750	air	$1.9 \cdot 10^{-10}$	[111]
		800		$2.2 \cdot 10^{-10}$	
		850		$9.3 \cdot 10^{-10}$	
		900		$6.3 \cdot 10^{-9}$	
		950		$4.2 \cdot 10^{-8}$	
	30	750		$4.2 \cdot 10^{-10}$	
		800		$5.3 \cdot 10^{-10}$	
		850		$2.2 \cdot 10^{-9}$	
		900		$1.5 \cdot 10^{-8}$	
	50	750		$8.9 \cdot 10^{-10}$	
		800		$1.8 \cdot 10^{-9}$	
		850		$6.3 \cdot 10^{-9}$	
		900		$5.3 \cdot 10^{-8}$	
FeCr alloy	20	700	air	$7.5 \cdot 10^{-8}$	[84]
	20	750		$2.2 \cdot 10^{-7}$	
	20	900		$1.3 \cdot 10^{-4}$	
	35	700		$1.0 \cdot 10^{-6}$	
	35	750		$6.5 \cdot 10^{-6}$	
	35	850		$3.5 \cdot 10^{-4}$	

With respect to creep of BSCF, previous reports mainly concentrated on the deformation under compressive loads [109,110]. Rutkowski et al. [110] thoroughly studied the creep behavior of BSCF under this loading mode. They found that creep rates under reduced oxygen partial pressure are approximately one order of magnitude higher than in air, and an increase of grain size slightly decreases creep rates at temperatures above 850 °C in air. Moreover, they reported that between 600 °C and 800 °C the compressive creep rates of BSCF in air are almost constant and the creep rate continuously increases between 850 and 900 °C. However, potential creep rupture under tensile or combined tensile-compressive loads is obviously an important aspect since during operation both, tensile and compressive stresses, act on the membrane components (see section

3.3.2). Rutkowski et al. [110] found in C-ring creep tests carried out at BSCF the formation of pores along grain boundaries normal to the tensile stresses that ultimately might lead to creep rupture for long term loading. In fact, they estimated a critical strain of ~ 0.2 % for damage initiation.

Huang et al. [111] also reported higher creep rates under vacuum than in air for LSCF. A change in activation energy between 800 and 850 °C was assigned to a phase transition along with a change of the dominating effect of intrinsic to extrinsic vacancies and not to a transition of the creep mechanism since the stress factor remained rather constant.

Schweda analyzed the creep behavior of a FeCr alloy [84] and, as might be expected for metals, reported a few orders of magnitude higher creep rates than for BSCF and LSCF. No creep data of CGO are reported so far.

In order to predict the long term performance of membrane structure, a maximum tolerable creep deformation has to be determined. According to [112], membrane materials should not creep in a compressive mode more than 1 % per year to warrant reliable long term operation. Since the creep rate depends on the applied stress, Schulz et al. [113] calculated that the compressive stress exerted on a membrane during operation in a CO_2 separation system is approximately 30 MPa. The literature data of BSCF and LSCF for this applied stress are presented in Figure 3-20. It seems that both materials exhibit higher creep rates than acceptable under this stress level, hence stress reducing design modifications might be necessary.

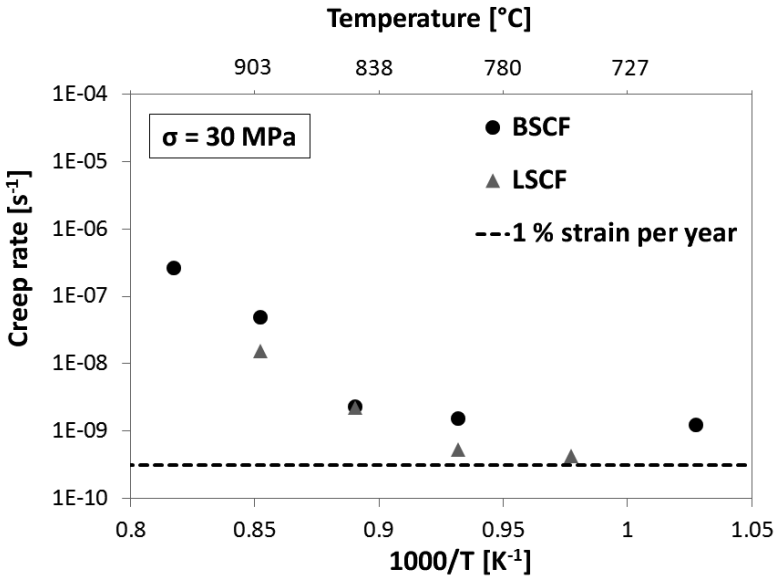

Figure 3–20: Creep rates of BSCF [110] and LSCF [111] compared to the tolerable creep strain per year.

3.2.6 Mechanical properties - porosity

The porosity of the potential substrate materials needs to be high enough to limit its influence on oxygen permeation through the membrane structure. However, the porosity does not only affect the transport properties. It also influences mechanical properties since it decreases the effective cross-sectional area which carries the applied load.

The porosity can be characterized by the volume fraction of pores with respect to other phases. Pores can act as stress concentrators, for instance, a single ideally spherical pore increases the local stress by a factor of three [114]. Hence, porosity needs to be considered in the interpretation of experimental data since it is verified that it strongly influences the mechanical properties [115,116,117]. Due to processing limitation and ongoing developments, not all substrate materials were available with the desired porosity and a prediction of the properties of porous materials based on the data obtained for dense materials was sometimes necessary. The effect of porosity is usually based on experimental data which are fitted by a power law relationship. For the

elastic modulus a variety of relationships has been suggested [118], which all agree well up to porosities of ~ 20 %. Radovic et al. [119] performed investigations on oxidized NiO-YSZ and reduced Ni-YSZ with different porosities. They reported that the elastic modulus, fracture strength and fracture toughness can be described with the same power law equation. Recently, a master thesis by Yao [120], carried out for membrane and solid oxide fuel cell materials, suggests the relationship to obtain the closest fitting curve:

$$E_p = E_0 \cdot (1 - 1.372 \cdot p)^{1.897} \qquad 3.16$$

where E_p and E_0 are the elastic moduli of porous and dense material, respectively, and p is the volume fraction of pores.

3.3 Lifetime predictions

3.3.1 Stress–probability–time diagram

Stress–probability–time (SPT) diagrams [47] incorporate the time dependence of strength into failure statistics. Because of the stochastic nature of failure of ceramic components it is not possible to calculate a specific and definite lifetime depending on load and geometry. Rather failure needs to be expressed in terms of probabilities. The use of SPT diagrams, together with finite element analysis of local stress distribution, allows the design of ceramic components with very low failure probabilities during their envisaged minimum lifetime. Prerequisites for calculation of a SPT diagram are loading rate dependent strength data (see section 3.2.3), as a measure of the subcritical crack growth sensitivity of the material, and the Weibull distribution (see section 3.2.2).

To construct SPTs, the results obtained in SCG investigations need to be taken as input data. In particular, the values of Weibull modulus, characteristic fracture strengths and n parameter are necessary. The fracture strength values under dynamic loading can be converted into equivalent fracture strengths under static loading, permitting a prediction of lifetime under constant load. Hence, the characteristic fracture strength σ_0, measured at a stress rate of $\dot{\sigma}$, can be converted into an equivalent strength that would cause the sample to fail in 1 s, with a fracture probability P_f of 63.2 % [121,47] using:

$$\sigma_{1s} = \sigma_0 \left(\frac{\sigma_0}{\dot{\sigma} \cdot (n+1)}\right)^{\frac{1}{n}} \qquad 3.17$$

Combination of this stress and the failure probability of 63.2 % results in a first data point on the SPT diagram. The *1 s* line crosses the σ_{1s} data point and has a slope equal to the Weibull modulus *m*. The prediction of different lifetimes can be performed using the relationship [47]:

$$\frac{t_2}{t_1} = \left(\frac{\sigma_1}{\sigma_2}\right)^n \qquad 3.18$$

Therefore, a series of lines can be drawn, with spacing between the lines equal to (*ln10)/n*. In this case, each line represents one decade increase in lifetime. Equation (3.3) can then be used to assess the failure probability as a function of stress for a given geometry. In order to analyze the influence of the specimen or component size on the allowable stress, Equation (3.4) should be used.

An example of an SPT plot for $La_{0.2}Sr_{0.8}Fe_{0.8}Cr_{0.2}O_{3-\delta}$ (LSFCO) is given in Figure 3-21. According to Nagabhushana et al. [121], for a failure probability of 37 %, the maximally tolerable constant stress for this material is 10 MPa in order to reach 30 years lifetime.

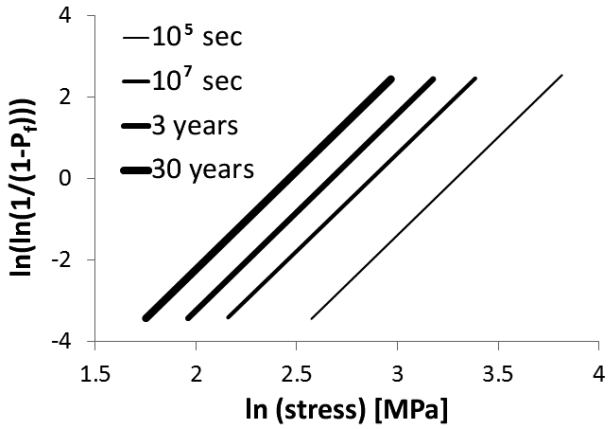

Figure 3–21: Lifetime prediction for LSFCO using a strength-probability-time diagram [121]. The slope corresponds to the Weibull modulus.

3.3.2 Creep rupture

Creep rupture [101] appears after the final, tertiary creep stage which is rather short and the material exhibits a rapid deformation in this stage. The creep rupture time is influenced by the applied stress, temperature and environment. Creep rupture can depend on the initial defect distribution, but often failure occurs by the formation and percolation of pores at the grain boundaries. Corresponding observations were reported by Passmore et al. [122] for magnesium oxide after creep deformation in bending (Figure 3-22).

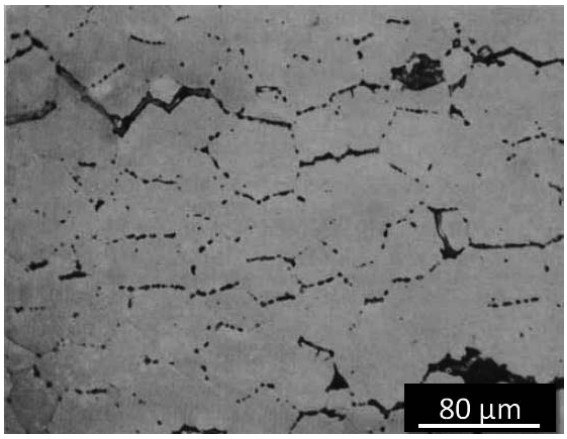

Figure 3–22: Crack-opening normal to the tensile stress leading to creep failure of magnesium oxide [122]. A stress of 33 MPa was applied at 1267 °C.

Creep rupture was in this study investigated using three-point bending test. In fact, bending tests have been frequently used to assess creep deformation of ceramic materials [123,124,125,126,127], where sometimes the strain distribution has been characterized in addition using hardness impressions as markers [128,129], to assess potential differences between tensile and compressive creep.

The need to investigate creep of membrane materials in combined tensile – compressive mode is proven by results obtained by Schulz et al. [113], who used numerical simulation to investigate the stress distribution of a bulk membrane under realistic operational conditions. BSCF was used as a model material. The applied load corresponded to the pressure gradient (outer: feed side 20 bar; inner: sweep side 10^{-5} bar) and the associated chemically induced stress at 900 °C, however,

creep was not taken into account. The resulting stress distribution over the membrane thickness proves that the stress changes from tensile on the outer side to a compressive state on the inner side. A schematic illustration is shown in Figure 3-23.

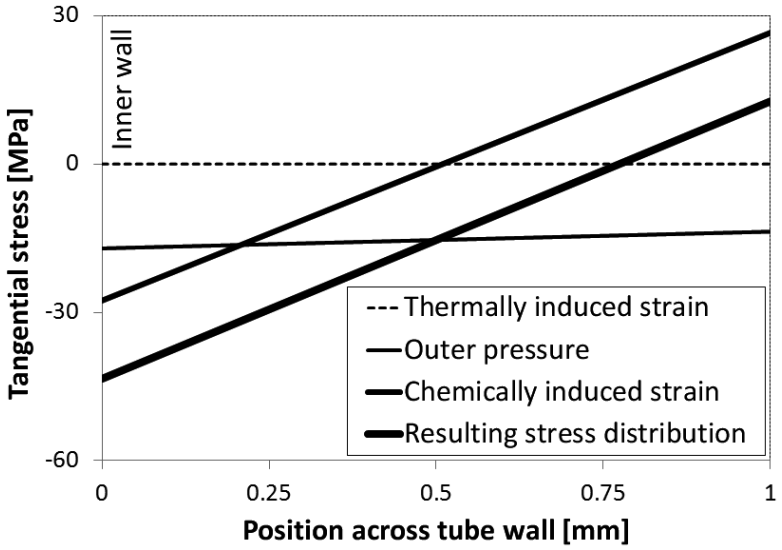

Figure 3–23: Stress distribution over the membrane thickness revealing the existence of tensile and compressive stresses [[113]].

3.3.3 Monkman-Grant relationship

Creep life prediction is possible if the creep rates and stresses leading to failure can be assessed mathematically. If the secondary creep regime dominates the strain – time behavior (see section 3.2.5), the creep rupture of the material should be independent of the initial defect distribution. It can then be described by a Monkman-Grant relationship [[130,131,132]]:

$$\dot{\varepsilon}_{min} \cdot t_r = C_{MG} \qquad 3.19$$

with the material constant C_{MG}, the minimum (secondary) creep rate $\dot{\varepsilon}_{min}$ and the creep rupture time t_r. Therefore, if the material´s constant and creep rate behavior are known, the time to rupture can be predicted. This relationship is effectively a critical strain criterion since it assumes that materials always fail by creep rupture after reaching a certain strain. However, from an

analysis of the experimental data obtained on a number of materials, it has been verified that the scatter in the experimental results can be reduced by using the relationship [133]:

$$\frac{\dot{\varepsilon}_{min} \cdot t_r}{\varepsilon_r} = C_{MMG} \qquad 3.20$$

where ε_r is the strain at rupture, and C_{MMG} is a modified Monkman-Grant constant.

4 EXPERIMENTAL

4.1 Material description

4.1.1 BSCF

Dense disc-shaped $Ba_{0.5}Sr_{0.5}Co_{0.8}Fe_{0.2}O_{3-\delta}$ specimens were produced at Fraunhofer Institute for Ceramic Technologies and Systems (IKTS), Hermsdorf branch. The powder was prepared by a conventional mixed oxide route. The components $BaCO_3$, $SrCO_3$, Fe_2O_3 and Co_3O_4 were weighted in stoichiometric amounts and milled together. After repeated milling, the powder was dried and pressed to pellets with a pressure of 90 MPa for 1.5 min. Afterwards they were sintered for 2 h at 1130 °C with heating and cooling rate of 2 K/min. The specimen geometries were approximately Ø 16 mm × 2 mm.

Porous disc-shaped BSCF specimens were produced at IEK-1, Forschungszentrum Jülich by tape casting. The powders, supplied by Treibacher Industrie AG Austria, were mixed with 20 wt-% organic pore former (corn starch) and different volatile additives to form homogenous slurry. Afterwards they were tape cast using the doctor blade technique [134] with a thickness of 1.9 mm, and dried in ambient air. The discs were cut using a hollow punch to a diameter of 30 mm. The specimens were then debindered and sintered at the same time on ZrO_2 plates. The program consisted of a large number of temperature steps in order to provide sufficient time for debinding and evaporation of the organic components. The sintering procedure is described in Figure 4-1. After sintering, the specimens had diameter of approximately 24 mm and were 0.8 mm thick. According to the manufacturer, resulting porosity was 34 %.

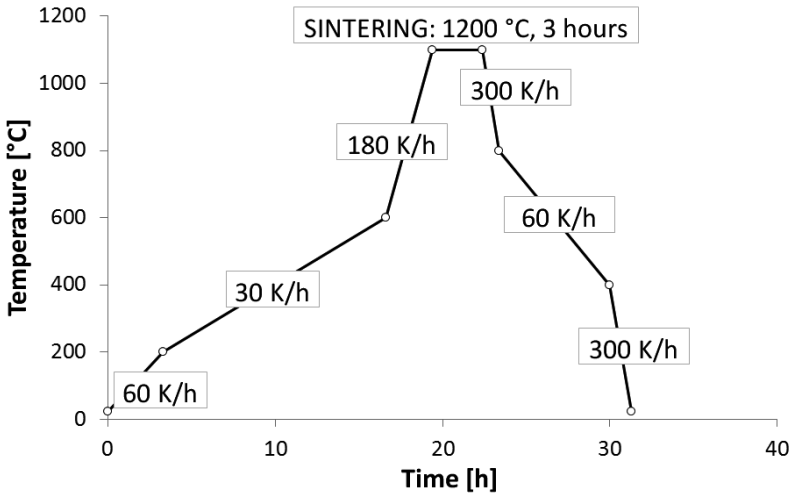

Figure 4–1: Sintering procedure of porous BSCF. Step 3 corresponds to the sintering temperature of 1100 °C with 3 hours of dwell time.

Dense, bar-shaped BSCF specimens were prepared at IEK-1, Forschungszentrum Jülich, from powders supplied by Treibacher Industrie AG, Austria. The powders were uni-axially pressed in a bar mold 5 mm × 40 mm with a pressure of 85 MPa for 1.5 min, and then sintered at 1100 °C for 3 h. Heating and cooling rate were 5 K/min. The specimen geometries were approximately 4 mm × 4 mm × 30 mm.

4.1.2 LSCF

$La_{0.58}Sr_{0.4}Co_{0.2}Fe_{0.8}O_{3-\delta}$ powder was produced at IEK-1, Forschungszentrum Jülich by spray-pyrolysis [135]. Disc-shaped LSCF specimens were pressed to pellets in a mold of 27 mm diameter with a pressure of 80 MPa for 1.5 min. Afterwards they were sintered for 5 h at 1200 °C with a heating rate of 5 K/min and a cooling rate of 0.5 K/min. The specimen geometries were approximately Ø 22 mm × 1 mm.

Bar-shaped specimens were pressed in a bar mold 5 mm × 40 mm with a pressure of 75 MPa for 1.5 min, and then sintered at 1200 °C for 5 h. Heating rate was 5 K/min, and cooling rate was 0.5 K/min. The specimen geometries were approximately 4 mm × 4 mm × 30 mm.

4.1.3 CGO

Eleven $Ce_{0.9}G_{0.1}O_{1.95-\delta}$ batches were supplied for mechanical characterization with the aim to get process dependent properties in order to optimize the production process. The CGO material was produced by tape casting by DTU Energy Conversion (Roskilde, Denmark). Ultra low surface area (ULSA) CGO from Rhodia S.A. (France) was used as base ceramic powder for all tapes. Table 4-1 shows all preparation details and differences in production of the CGO batches. The porosity was graphically determined from SEM images by the manufacturer.

Table 4-1: Manufacturing details of the investigated CGO batches.

Batch	Sint. time [h]	Sint. temp. [°C]	Layers	Ceramics v %	Graphite v %	Dispersant v %	Binder v %	Porosity [%]
1	12	1300	7	17.2	15.1	1.7	66.0	29
2	12	1300	7	17.3	15.1	1.7	66.0	21
3	12	1300	7	23.3	15.2	1.6	60.0	16
4	4	1050	1	30.0	14.4	3.8	51.8	38
5	4	1050	1	30.9	11.1	3.9	54.1	36
6	4	1050	1	31.0	11.1	4.4	53.6	56
7	4	1150	1	31.0	11.1	4.4	53.6	40
8	4	1250	1	31.0	11.1	4.4	53.6	27
9	4	1050	1	24.9	16.4	3.6	55.2	43
10	4	1150	1	24.9	16.4	3.6	55.2	29
11	4	1250	1	24.9	16.4	3.6	55.2	12

2 mol% of cobalt was used as sintering aid in the form of $Co(NO_3)_2$ for batches 1-3, whereas for batches 4-11 Co_3O_4 was used. A graphite powder, V-UF1 99,9 from Graphit Kropfmühl, was added as a pore former. The powder used for the batches 4-11 was pre-calcined for 2 h at 1100 °C. According to manufacturer, the pre-calcined powder had lower specific surface area of 5.1 m^2/g compared to the as-received powder (6.6 m^2/g), in order to obtain a sufficient thickness of the final tape cast layer.

The supports were mixed with different amounts of pore-former. Batches 1-3 were cast at 500 µm, whereas batches 4-11 were cast to a thickness of 1200 µm. These casting gaps correspond to a support of approx. 50 µm for batch 1-3, and 300 µm for batch 4-11 after sintering, depending on the specific sintering temperature. Due to the small thickness of the supports produced in batch 1-3, seven layers had to be laminated together before sintering. Slurries were prepared by dispersing the CGO powders and the sintering aid in a methylehylketone and ethanol solvent mixture (MEKET) with polyethyleneimine (PEI) dispersant for batches 1-2, and polyvinylpyrrolidone (PVP) for batches 3-11. These mixtures were ball milled for 72 h in PE bottles using zirconia balls. At this point, D50 (the diameter for which 50 % mass of the powder particles are larger than D50) was approximately 0.8 µm for batches 1-3, and 0.4 µm for batches 4-11, with particle size distributions (PSD) exhibiting a bimodal distribution. A polyvinyl butyral (PVB) based binder system [136] was finally added to the slurry and the slurry was then slowly rotated for another 24 h to achieve proper homogenization. Additionally, graphite powder was added in two to three portions within the first two hours after binder addition. Sequential additions were necessary in order to obtain a proper mixing. All slurries were finally filtered and de-aired before being tape casted with a doctor blade [134] adjusted as mentioned above. A slow temperature ramp adjusted to the used binder system was used for de-bindering and degassing at low temperatures. Finally, disc-shaped specimens were produced with dimensions shown in Table 4-2.

Table 4-2: Specimen dimensions of the eleven investigated CGO batches.

Batch number	1	2	3	4	5	6	7	8	9	10	11
Height [mm]	0.4	0.3	0.4	0.3	0.3	0.4	0.4	0.3	0.3	0.3	0.3
Diameter [mm]	18	18	20	25	25	27	24	22	27	25	24

4.1.4 FeCrAlY alloy

Gas-atomized FeCrAl powders were produced by Sandvik Osprey (United Kingdom). The composition (wt %) is shown in Table 4-3. Other minor alloying elements were 0.15 % Co, 0.1 % Ni, 0.05 % C, 0.015 % P, and 0.01 % S (maximum values). The powders were supplied in two different size fractions: < 10 μm, and 10 - 38 μm. The smaller size fraction was used for preparing dense specimens, and the larger size fraction for preparing porous structures.

Table 4-3: Nominal composition (wt %) of the FeCrAlY alloy (with the balance being Fe).

Cr	Al	Mo	Y	Si	Mn
21 ± 1	7.5 ± 0.5	1 ± 0.3	0.125 ± 0.075	0.1 (max)	0.4 (max)

Both, metal tapes and pellets made from this alloy were fabricated by the project partner DTU Energy Conversion (Roskilde, Denmark).

Tape casting slurries were prepared by dispersing metal powder (10 – 38 μm) in 5 wt. % water-based PVA solution by ball milling for 24 h. Octanol was added to the slurry as a de-foamer. The slurry was evacuated for at least 10 min to remove trapped gas, and prevent defects in the tape induced by air bubbles in the slurry. Tapes were cast onto a polymer sheet using the doctor blade technique [[134]], resulting in tapes with a dry thickness between 450 – 750 μm. Tape strips of the desired dimensions for mechanical measurements were cut from the tape using a blade.

Metal powder pellets were made by mixing the metal powder with a few drops of aqueous 3 wt. % PVA binder, which was hand milled until dry and then uni-axially pressed in a 6 mm diameter die with a pressure of 277 MPa for 20 s. For dense pellets the < 10 μm powder was used, and to prepare porous pellets the larger particle size fraction powder was used.

Sintering of both, tapes and pellets was performed in a tube furnace with 55 mm internal tube diameter with a single, approximately 10 cm long hot zone. An alumina tube was used with porous alumina heat shields. Ti sponge was also included in the furnace together with the specimens to trap remaining oxygen in the system, achieving oxygen partial pressures $pO_2 = 10^{-18}$ - 10^{-20} atm. All specimens were sintered at 1250 °C for 1 hour in a reducing atmosphere (flowing 9 % H_2/Ar ($pO_2 = \sim 10^{-19}$ atm)), with heating and cooling rates of 50 K/h.

Porous material was tested in two geometries: thin strips and cylinders. The dense specimens had only cylindrical shape. Detailed geometry data is given in Table 4-4.

Table 4-4: Specimen geometries of the FeCrAlY alloy.

Microstructure	Shape	Dimensions [mm]
Porous	Strips	45 × 10 × 0.5
Porous	Cylinders	Ø 6 × 10
Dense	Cylinders	Ø 6 × 10
Dense	Hollow cylinders	($Ø_{inner}$ 8, $Ø_{outer}$ 13) × 10

4.1.5 Model material - SOFC

Since membrane composites of adequate dimensions were not available, a SOFC half-cell was used as model material to investigate the applicability of linear elastic theory for curved bi-layered materials typical for layers on porous substrates to verify the applied ring-on-ring bending test procedures.

The specimens were supplied by CeramTec GmbH (Marktredwitz, Germany) as composite material consisting of substrate and membrane. The samples had an overall thickness of ~ 310 µm (substrate layer ~ 300 µm, membrane layer ~ 10 µm). In the as-sintered state, the substrate consisted of a mixture of yttria-stabilized zirconia (YSZ) and nickel oxide (NiO) and the membrane of YSZ. Due to a thermal expansion mismatch between the substrate and coating ($\Delta\alpha \sim 2 \times 10^{-6}$ K^{-1}), the unconstrained half-cell composites were curved at room temperature. The electrochemical operation requires NiO to be reduced to Ni. However, the reduction of NiO to Ni increased the porosity and led to an additional change in substrate stiffness and curvature. During the reduction of the samples (4 % H_2/Ar), the curvature radius of the specimens changed from ~ 520 mm to ~ 170 mm.

4.2 Characterization techniques

In this chapter details of the experimental procedures that are employed for mechanical characterization and lifetime assessment are outlined together with their theoretical background.

4.2.1 Micro-indentation

The indentation tests were carried out with a Fischer HC100 micro-indenter (Figure 4-2). As recommended in the ASTM C1327, indents were sufficiently distanced from each other in order to avoid interactions. Indentations were performed with a Vickers diamond tip [137].

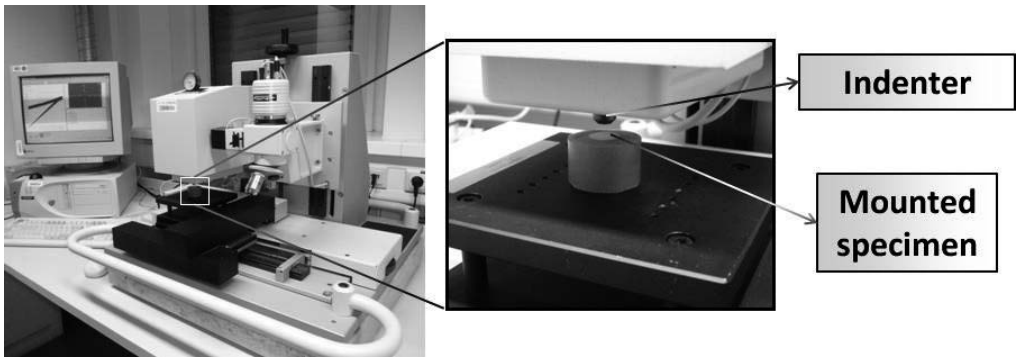

Figure 4–2: Fischer micro-indenter and mounted specimen.

When the indenter is loaded onto the specimen surface, the resulting load-depth curve reflects the elastic-plastic deformation, followed by an elastic unloading curve (Figure 4-3).

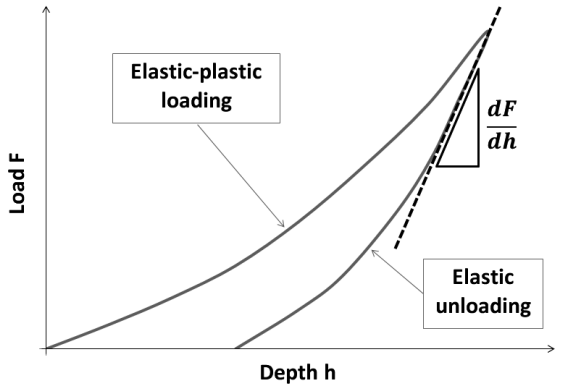

Figure 4–3: Typical load-displacement curve obtained with a Vickers micro-indenter.

Hence, the elastic contact equations were used for the unloading stage to determine the elastic modulus. According to Oliver and Pharr [138], the reduced elastic modulus is given by:

$$E_r = \frac{dF}{dh}\frac{1}{2}\frac{\sqrt{\pi}}{\sqrt{A}} \quad 4.1$$

where *dF* and *dh* are linear parts of force and depth in the elastic unloading, respectively, and *A* is the contact area. However, E_r is a combination of the elastic modulus of specimen (E_{IT}) and indenter (E_i), which, however undergoes only a small deformation during the test. The elastic modulus of the specimen is then calculated using the relationship [[138]]:

$$\frac{1}{E_r} = \frac{1-\nu^2}{E_{IT}} + \frac{1-\nu_i{}^2}{E_i} \quad 4.2$$

where ν and ν_i are the Poisson ratios of the specimen and indenter, respectively.

Indents were made on two materials at RT in air: dense FeCrAlY alloy and dense BSCF. The tests at dense FeCrAlY alloy were carried out to determine the elastic modulus since specimens were not available in the necessary geometry for the other testing methods. The maximum load was 1 N with 15 seconds hold time. The analysis was based on 50 indents. An example of an impression mark is given in Figure 4-4.

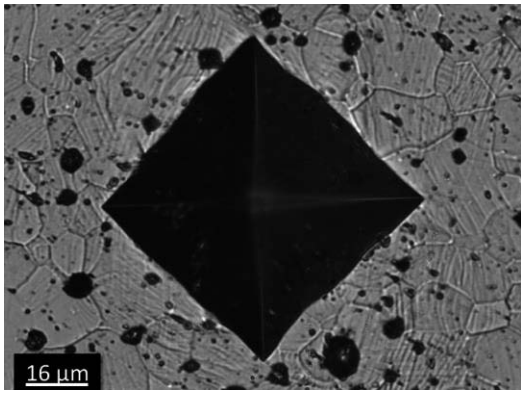

Figure 4–4: Indent imprinted with 1 N in FeCrAlY alloy.

Impressions were also performed on dense BSCF bar-shaped specimens. Here the indents were placed on one polished lateral side. The aim was not to determine the elastic modulus, but to determine the apparent creep strain by the change of distance between indentation marks before and after creep testing in bending. An example of an indented specimen is shown in Figure 4-5. Two lines, each consisting of 50 indents with sufficient distances ensuring no crack interaction

among them, were imprinted in the middle region of the sample. The indentation load was 1 N with a holding time of 5 seconds.

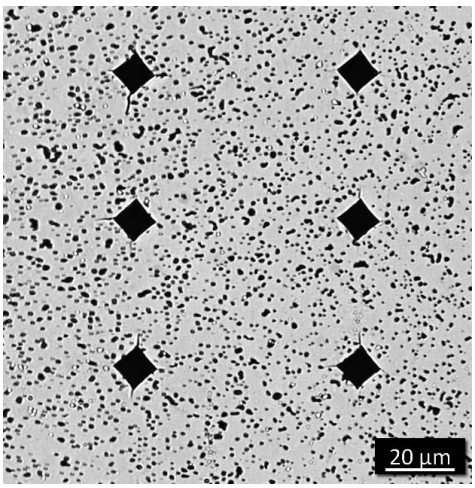

Figure 4–5: Indented BSCF surface (load 1 N) before the bending test.

4.2.2 Bending tests

Bending tests were performed using an Instron 1362 test machine. The central displacement of the specimens was detected by a sensor in contact with the lower (tensile loaded) surface of the sample. The displacement was measured with a ceramic extension rod attached to a linear variable differential transformer (Sangamo, LVDT, range ± 1 mm, precision 1.25 µm). The load was determined with a 1.5 kN load cell (Interface 1210 BLR). A half-sphere was used in the loading set-up to exclude any misalignment which could lead to uncertainties and scatter of results. Two different bending techniques have been used, ring-on-ring test and three-point bending test, with disc- and bar-shaped specimens, respectively. Tests were carried out from room temperature up to maximally 1000 °C. The temperature was monitored close to the outer specimen surface with a thermocouple type K.

4.2.2.1 Ring-on-ring bending test

a) Test procedure and general evaluation

In the ring-on-ring bending test [[139]], a loading ring bends a thin plate vertically constrained by a supporting ring (Figure 4-6). The linear bending theory is used to determine the fracture stress since brittle ceramic materials usually fail after mainly elastic deformation.

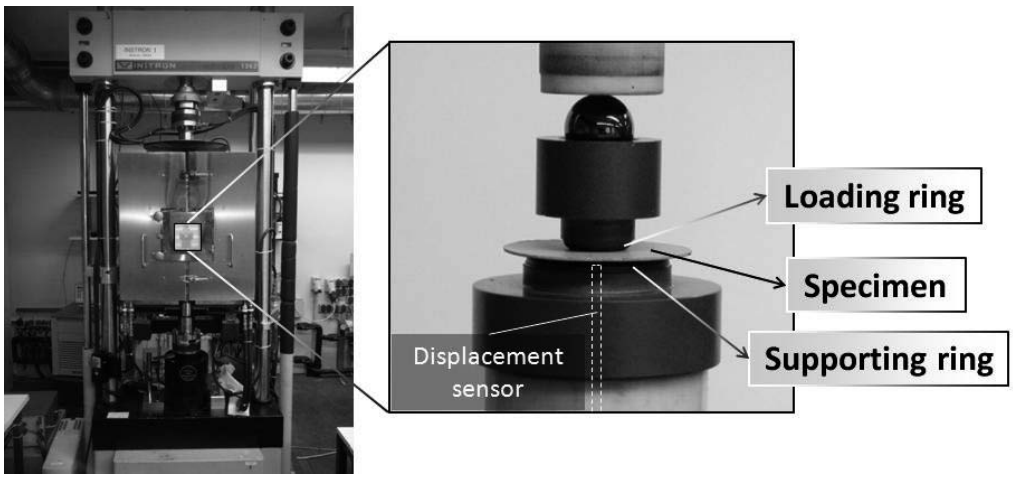

Figure 4–6: Ring-on-ring test set-up.

The applied procedure followed DIN 51105. The determination of the elastic modulus was based on the equation:

$$E = \frac{3 \cdot F \cdot r_1^2 \cdot (1-\nu^2)}{2\pi \cdot u \cdot h^3} \cdot \left[\left(\frac{r_2}{r_1}\right)^2 - 1 - ln\left(\frac{r_2}{r_1}\right) + \frac{1}{2}\left(\frac{1-\nu}{1+\nu}\right) \cdot \left(\frac{{r_2}^2 - {r_1}^2}{{r_3}^2}\right) \cdot \left(\frac{{r_2}^2}{{r_1}^2}\right) \right] \quad 4.3$$

where F and u are force and deflection determined from the linear part of the load-deflection curve (at low loads a non-linearity in the curve might be observed due to specimen unevenness), respectively, ν is the Poisson´s ratio, h is the sample height, and r_1, r_2, and r_3 are the loading ring, support ring, and specimen radii, respectively. For linear behavior, as might be expected for brittle fracture, the maximum stress is constant over the tensile loaded surface inscribed by the loading ring and:

$$\sigma = \frac{3 \cdot F \cdot (1+\nu)}{2\pi \cdot h^2} \cdot \left[ln\left(\frac{r_2}{r_1}\right) + \left(\frac{1-\nu}{1+\nu}\right) \cdot \left(\frac{{r_2}^2 - {r_1}^2}{2 \cdot {r_3}^2}\right) \right] \quad 4.4$$

The statistical analysis requires a determination of characteristic strength and Weibull modulus, since the measured strength decreases with increasing deformed characteristic area/volume [73,140,141]. The fracture stress data σ were used to determine the characteristic strength σ_0 and the Weibull modulus *m.* Taking the logarithms of both sides, the Weibull relationship Equation (3.3) converts to:

$$ln\,\sigma_0 = ln\,\sigma + \frac{1}{m} ln\left\{ ln\left[\frac{1}{1-P_f(V_0)}\right]\right\} \quad 4.5$$

which corresponds to the simple linear equation $y = ax + b$ where the X-axis represents $ln\,\sigma$, and the Y-axis $ln\left\{ ln\left[\frac{1}{1-P_f(V_0)}\right]\right\}$. Particular stress values σ are ranked in ascending order with specific probabilities of $P_i = i / (n+1)$, where i stands for particular rank number and n is the total number of investigated values. Weibull modulus and characteristic strength can be determined graphically in such a Weibull plot [142], and numerically using the maximum likelihood method [143], according to ASTM C1239-07. For the latter case, the system of equations obtained by differentiating the likelihood function is defined by ISO 20501:

$$\frac{\sum_{i=1}^{n}(\sigma_i)^m \; ln\,\sigma_i}{\sum_{i=1}^{n}(\sigma_i)^m} - \frac{1}{n}\sum_{i=1}^{n} ln(\sigma_i) - \frac{1}{n} = 0 \quad 4.6$$

$$\sigma_0 = \left[\left(\sum_{i=1}^{n}(\sigma_i)^m\right) \frac{1}{n} \right]^{\frac{1}{m}} \quad 4.7$$

The ring-on-ring tests were carried out for BSCF, LSCF and CGO. The purpose of the tests and their detailed description are given in Table 4-5. The tests performed at CGO batch 9 to determine the mechanical properties as a function of temperature were carried out on 9 specimens till failure with elastic loading of the specimens at each prescribed temperature. The number of specimens per test was limited by the available material.

Table 4-5: Performed ring-on-ring tests. Resulting fracture properties are represented by fracture strength and strain with the associated Weibull moduli. Bold text indicates the material and batch.

Material	Test purpose	Number of specimens	Loading rate [N/min]	Loading / supporting ring diameter [mm]	Environmental conditions
Dense BSCF	Elastic modulus, fracture properties, SCG, SPT	4	1	3.3 / 10	RT, air
		10	10		
		10	100		
		5	1000		
Porous BSCF	Elastic modulus, fracture properties, SCG, SPT	10	1	7.9 / 15	RT, air
		9	10		
		10	100		
		10	1000		
LSCF	Elastic modulus, fracture properties, SCG, SPT	4	1	7.9 / 15	RT, air
		4	10		
		15	100		
		4	1000		
CGO 1-11	Elastic modulus, fracture properties	221	100	7 / 10 **(1-3)** 9 / 19 **(4)** 7.9 / 15 **(5-11)**	RT, air
CGO 9	Elastic modulus, fracture properties-temperature dependence	9	100	7.9 / 15	200,400, 600,800 -air
CGO 9	SCG, SPT	6	0.1	7.9 / 15	RT, air
		7	1		
		17	10		
		28	100		

b) Subcritical crack growth

The experiments for SCG analysis were carried out with different loading rates, with steps of one order of magnitude. Depending on the test conditions and available material, 4 up to 28 specimens were tested at each loading rate, permitting an estimation of Weibull modulus following ASTM C1239-07. The fracture stress was determined using Equation (4.4). The fracture stress data σ were used to determine characteristic strength σ_0 and Weibull modulus m using a maximum likelihood statistical analysis according to ASTM C1239-07, based on the relationship for the failure probability P_f (Equation 3.3). The stress rate sensitivity of fracture strength was used to assess subcritical crack growth sensitivity using Equation 3.8.

BSCF, LSCF and CGO were analyzed with respect to their SCG sensitivity. Porous and dense BSCF was tested in order to determine the influence of porosity on SCG. Results from fracture tests were taken as input data. The test description is therefore given in Table 4-5.

c) Stress–probability–time diagram

Results of all materials tested with respect to their SCG sensitivity were used as input data for the SPT lifetime predictions. Equation (3.3) was then used to assess the failure probability as a function of stress for a given geometry. The SPT plot was calculated from Equations (3.17) and (3.18), as described in section 3.3.1.

4.2.2.2 Three-point bending test

In a three- point bending test, a bar-shaped sample is placed on two supporting rods, and the load is applied by a rod placed in the center, as illustrated in Figure 4-7.

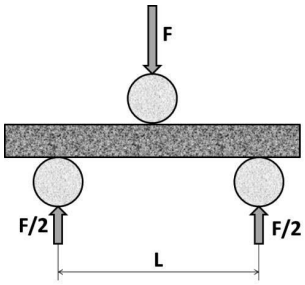

Figure 4–7: Schematic illustration of a three-point bending test.

Three point bending tests were used to characterize creep rupture of BSCF and LSCF, following the procedure recommended in ASTM C1-161. Appropriate CGO specimens were not available. The tests were carried out up to failure at 850 °C and 900 °C, which are proposed operating temperatures of gas separation membranes in air. At 800 °C the creep rates were too low to reach failure relevant creep deformations in a reasonable time.

Three point bending tests were also carried out at the FeCrAlY alloy in order to determine the elastic modulus as a function of temperature. The tests were performed on two specimens, each elastically loaded four times at the respective temperatures. The testing conditions are given in Table 4-6.

Table 4-6: Testing conditions for specimens tested in three-point bending for a) creep rupture, and b) elastic modulus as a function of temperature. In case of (a), letter B represents BSCF, whereas L represents LSCF material.

a)	1	2	3	4	5	6	7	8	9	10	11	12	13	14
Material	B	B	B	B	B	B	B	B	B	B	B	B	L	L
Stress [MPa]	27	35	42	57	64	14	20	25	29	33	38	44	33	43
Support distance [mm]	20	20	20	20	20	20	20	20	20	20	20	20	20	20
Temp. [°C]	850	850	850	850	850	900	900	900	900	900	900	900	900	900

b)	1	2
Material	FeCrAlY alloy	
Support distance [mm]	40	
Elastically loaded at each temperature	4 x	4 x
Temperature [°C]	RT, 200, 400, 600	RT, 200, 400, 600

The specimens were heated in load free state with a rate of 8 K/min. A dwell time of 1 h was chosen to reach thermal equilibrium before testing. The specimens were tested in the as-sintered condition. Only one side face of selected bar-shaped BSCF specimens was polished to permit an optical assessment of the strain using the change of distance between hardness impressions [144,145], as illustrated in Figure 4-8. Confocal (Keyence VK 9700) and scanning electron microscopy (LEO 440) were used to analyze fracture surfaces and microstructure.

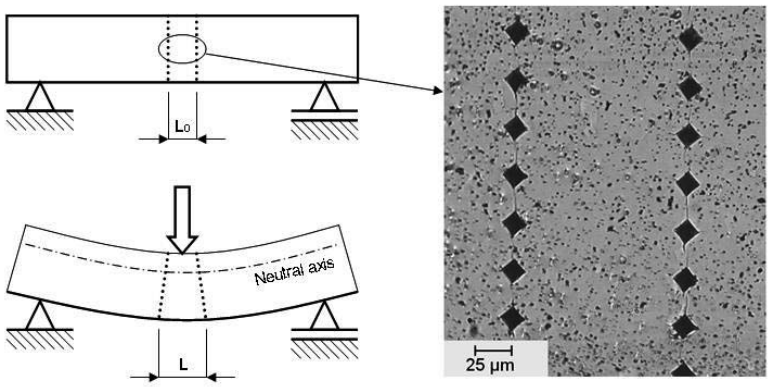

Figure 4–8: Indentation marks used for evaluation of the local strain in three-point bending test.

According to the linear elastic theory, the maximum stress, which appears in the central part on the tensile side of the specimen, can be determined from the relationship [146]:

$$\sigma = \frac{3 \cdot F \cdot L}{2 \cdot b \cdot h^2} \qquad 4.8$$

where F is the applied force, L is the length between supporting rods, b is the sample width, and h is the sample height. The maximum strain can be determined using the equation [146]:

$$\varepsilon_{cr} = \frac{6 \cdot h \cdot \Delta f}{L^2} \qquad 4.9$$

where Δf is the sample deflection after the creep test.

4.2.2.3 Monkman–Grant relationship

BSCF specimens that failed in creep rupture tests at 850 °C and 900 °C were also used to check whether a description of the high temperature deformation behavior by the Monkman–Grant

lifetime prediction relationship is possible [133]. Some tested specimens had additional marks on one side imprinted before the three point bending test. Table 4-7 gives the testing conditions of the specimens with indentation marks. Some specimens were loaded till failure and compared with non-indented specimens in order to verify that the indentation marks did not influence the creep rupture of material, i.e. if they have identical failure times.

Table 4-7: Testing conditions of BSCF specimens used for the Monkman-Grant analysis.

	1	2	3	4	5	6
Temperature [°C]	850	850	900	900	900	900
Stress [MPa]	35	57	14	20	29	33
Till failure	+			+		+

4.2.3 Compressive creep test

Creep behavior of the metallic material was analyzed in compression creep tests in which cylindrical specimens were uniaxially loaded between two supports (Figure 4-9). The flatness of the previously ground and polished base surfaces and the parallelism between them was ensured to be 0.04 mm and 0.1 mm, respectively, to minimize surface effects and superimposed bending induced by misalignments. The strain was calculated from the measured deformation by:

$$\varepsilon = \frac{\Delta h}{h_0} \qquad 4.10$$

where h_0 is the initial height and Δh is the deflection of the specimen. Similar as Schweda who analyzed creep of a FeCr alloy [84], a Norton law (Equation 3-14) was used in the current study to determine the creep rate of FeCrAlY alloy. By plotting the natural logarithm *ln* of the steady state creep-rate $\dot{\varepsilon}$ against $ln\ (\sigma)$, at constant temperature T, n is determined as the slope in the plot. The Arrhenius approach (Equation 3.15) suggests that by plotting $ln\ (\dot{\varepsilon})$ against the reciprocal of the absolute temperature $(1000/T)$ at constant stress, the slope should permit a calculation of the activation energy Q.

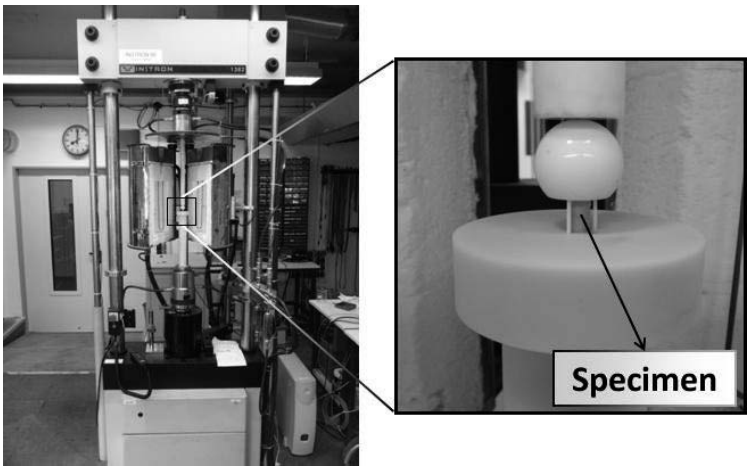

Figure 4–9: Compression creep test set-up.

Compression creep tests were performed using an Instron 1362 testing machine. A linear variable differential transformer (Sangamo, range ±1 mm, precision 1.25 μm), was used for measuring the vertical displacement. The transformer was coupled with the half-sphere in the clamping device by an alumina rod (Figure 4-9). The load was measured by load cells with 10 kN measuring range (1210 ACK, Interface Company). The temperature was monitored close to the outer specimen surface with a thermocouple type K.

The tests were only carried out for the FeCrAlY alloy in air from 700 °C up to 1000 °C, since for BSCF and LSCF compressive creep test data were available. No tests were performed at CGO since dense creep specimens of this material were not available. The specimens were heated in load free state with a heating rate of 8 K/min. A dwell time of 1 h was chosen to reach thermal equilibrium before testing. The applied stresses were 15, 30 and 45 MPa.

4.2.4 Microstructural analysis

Cross-sections were prepared for microstructural analysis according to [147]. The specimens were embedded in epoxy resin (Demotec 33) for several reasons: suitability for automatic preparation, easy handling, and possibility of marking specimens. The specimens were ground with SiC abrasive papers up to 4000 grit. Subsequently, polishing was performed with suspensions down to 1 μm grain size, and afterwards diamond paste was used with 0.25 μm grain size.

For grain size investigation, BSCF, LSCF and FeCrAlY alloy were etched using different procedures in order to make grain boundaries visible. Table 4-8 gives details of the etching procedures. Before thermal etching, the epoxy resin embedding the BSCF and LSCF specimens was dissolved in acetone.

Table 4-8: Etching methods.

	BSCF	LSCF	FeCrAlY alloy
Etching method	Thermal etching at 980 °C in air	Thermal etching at 1150 °C in air	Electrolytical etching with 5 % H_2SO_4
Dwell time	30 min	60 min	45 sec

Due to handling difficulties, related to the thickness of only 300 μm and extreme brittleness, CGO was not etched. As an alternative, its fracture surface was characterized to yield the grain size. Since the material had fine grains of around 1 μm, scanning electron microscopy was used.

The grain size was analyzed using the area counting technique. In particular, the equivalent circle diameter was obtained for all the materials by measuring grain areas and afterwards calculating the circle diameter of the equivalent area. The high amount of analyzed grains ensured that a representative mean value could be determined for all materials. Regarding CGO, only 6 batches were thoroughly analyzed since all CGO batches had rather similar grain size. Table 4-9 presents information on the investigated area and the number of analyzed grains.

Table 4-9: Number of analyzed grains.

	BSCF	LSCF	FeCrAlY	CGO 6	CGO 7	CGO 8	CGO 9	CGO 10	CGO 11
Investigated area [μm^2]	140 × 105	55 × 40	280 × 210	4 × 5	8 × 12	8 × 12	16 × 24	8 × 12	8 × 12
Number of analyzed grains	294	465	240	150	107	162	69	114	72

The analysis was performed using the software AnalySIS. The same software was also used for evaluation of the specimens' porosity. The principle was based on automatic detection of pores in a black/white microstructural image. The porosity value was obtained from the ratio of pore area to total area. All materials were investigated.

The microstructure of all materials was investigated using optical microscope (CSM, Switzerland) and scanning electron microscope (LEO 440). For the SEM analysis, specimens were coated with a thin platinum layer to prevent electrostatic charging of the surface. Whereas the fracture surfaces were investigated with a stereo-microscope (Zeiss Axiomat) at lower magnifications, confocal microscope (Keyence VK 9700) and the scanning electron microscope were used at higher magnifications.

4.3 Simulations

All numerical simulations were performed using the software package ANSYS 12. A 2D analysis was used in order to reduce computation time. All parameters are described in the following sections. Aiming for the accurate solutions, simulations were iteratively repeated until the convergence level decreased below 5 %.

4.3.1 Influence of mechanical properties on stress/strain induced failure

In addition to the elastic behavior, which is important for the simulation of the stress state, also the fracture strength has been experimentally characterized. However, one remaining question is whether the criterion for the selection of a substrate material should be the critical strength, critical strain, or the elastic modulus. The FEM analysis addressing this question was made for CGO since the largest database was available for this material. However, the analysis can be generalized to all materials.

As outlined above, various CGO batches were characterized with respect to their elastic behavior and fracture strength (see section 5.2.3). The properties depended on sintering temperature and porosity. Finite element analysis was used to determine which CGO batch provides optimal mechanical properties to be used as a porous substrate in an assumed symmetrical CGO on CGO membrane arrangement. Elastic modulus, fracture strength and critical strain were therefore taken into account in the analysis. The mechanical properties of dense layer were fixed and,

according to [148], the elastic modulus was assumed to be 180 GPa. Poisson's ratio was 0.3 for all materials. Since no thermal expansion mismatch exists between dense CGO membrane layer and porous CGO substrate, an assumed chemical strain of 0.2 % was used as an applied substrate load on the reduced side, decreasing with linear gradient across the membrane thickness (Figure 4-10). This rather high strain was used to compare how different CGO batches react to the chemically induced stresses. In real application the difference in oxygen partial pressure between feed and sweep side will result in much lower chemical strains (see section 6.4.4).

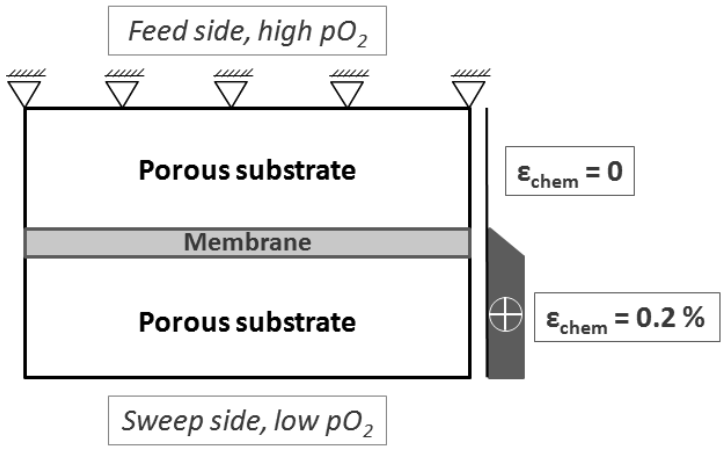

Figure 4–10: Assumed chemical strain distribution in a symmetric CGO membrane assembly.

The ratio of the apparent stress to fracture strength, and the ratio of the apparent strain to critical strain were taken as key parameters to find the optimum membrane arrangement.

The membrane structure was analyzed in plane stress state. Thicknesses of porous supports and dense membrane layer were 2 × 0.15 mm and 0.03 mm, respectively, which are realistic values according to the manufacturer (DTU Energy Conversion). The length of the structure was 5 mm. The horizontal surface of the substrate on the feed side was vertically constrained (Figure 4-10). The mesh was generated using 8-node plane stress quadratic quadrilaterals. The mesh also contained few triangle elements (~ 5). Simulation was performed with different mesh sizes. The most accurate solution was obtained with a mesh size of 10 µm (50574 nodes, 16503 elements). An example of the meshed model is given in Figure 4-11.

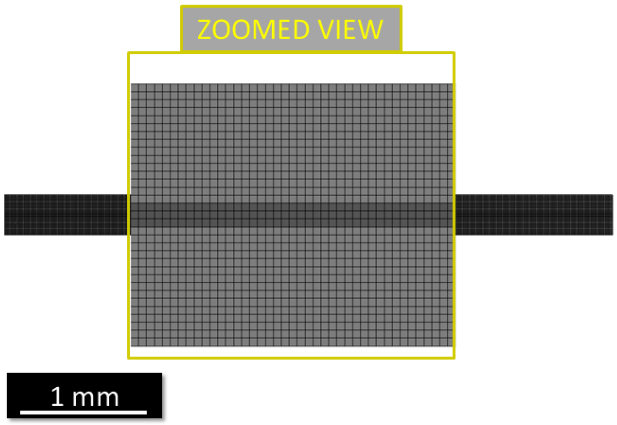

Figure 4–11: Meshed 2D model with 0.01 mm finite element size in the case of symmetrical membrane arrangement.

4.3.2 Parameters influencing the stress state of the membrane structure

Finite element analysis was used to verify the influence of parameters such as thicknesses, elastic moduli and thermal expansion coefficients, and to assess geometry influence on structural integrity of membranes. Both, planar and tubular arrangements were considered (Figure 4-12). The analysis was focused on three characteristic positions – the middle of the membrane layer, the substrate near the interface and the free substrate surface (Figure 4-13).

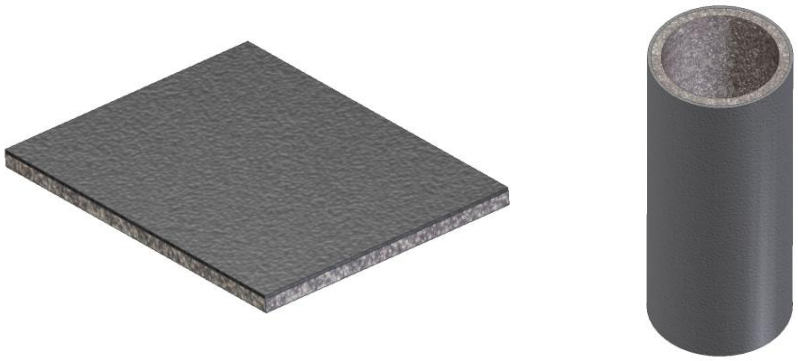

Figure 4–12: Illustration of planar and tubular membrane assembly.

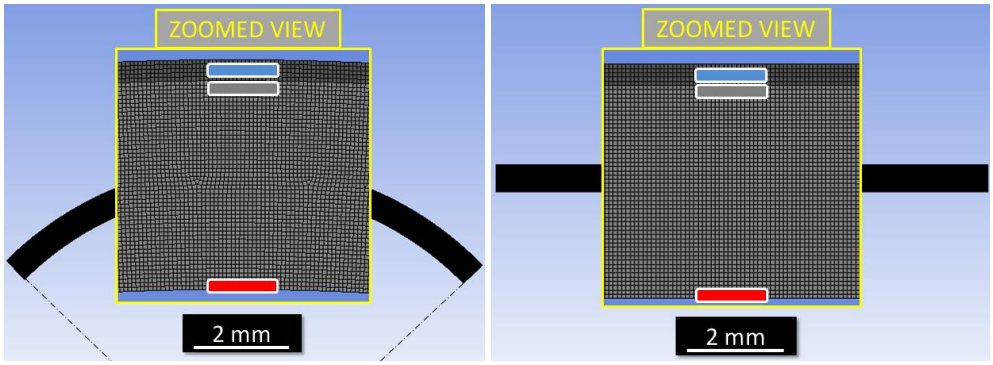

Figure 4–13: Meshed 2D models showing the analyzed positions of the tubular and planar structure: membrane layer (blue box), substrate interface (grey box) and the free substrate surface (red box).

The planar and tubular designs were modeled with similar loading conditions. Both were analyzed using plane stress state. Using the symmetry planes, the simulation was reduced to ¼ quarter of the cross-section. Although the geometry was varied, the standard inner and outer diameters of the substrate were 13 mm and 14 mm in case of tubular design, respectively. The outer diameter of the tube with membrane layer was 14.01 mm. Same thicknesses were used for the planar structure. The length of the structure was 10 mm. The mesh was generated using 8-node plane stress quadratic quadrilaterals. For the tubular case, the mesh also contained few triangle elements (~ 20). Simulations were performed with different mesh sizes in order to obtain results independent from the mesh size. The most accurate result was obtained with a mesh size of 1 µm (177974 nodes, 58585 elements in total for one simulation). An example of a meshed tubular model is given in Figure 4-14.

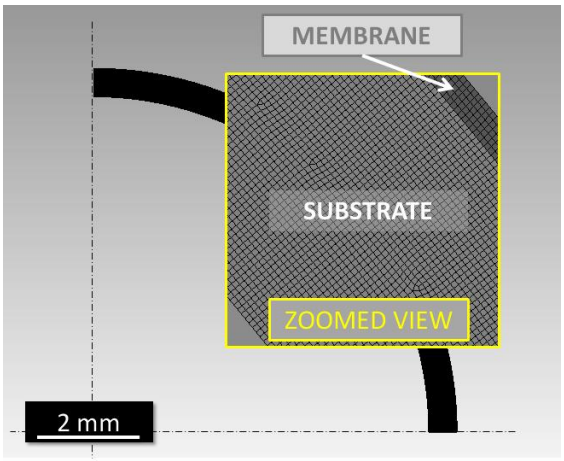

Figure 4–14: Meshed 2D model of the structure consisting of 500 µm thick substrate and 50 µm thick membrane.

To simplify the analysis, representative mechanical properties were used for the porous material (E = 55 GPa) based on the properties determined experimentally, for the dense membrane material the value might be considered as an upper limit for the properties of a dense layer (E = 200 GPa). The TEC values were assumed to be $8 \cdot 10^{-6}$ K^{-1} and $10 \cdot 10^{-6}$ K^{-1} for substrate and membrane layer, respectively. If not stated otherwise, the thicknesses of 0.5 mm and 0.005 mm were used for substrate and membrane, respectively. Poisson ratio was 0.3 in all cases. The stress free temperature during membrane deposition was assumed to be 1100 °C and the stress state was observed at RT. Stresses at higher temperatures are assumed to be relaxed by creep effects.

4.3.3 Optimal membrane design

The membrane structure can be symmetrical, or the substrate can be placed on the sweep or on the feed side in asymmetrical membrane configuration. Stress distribution over the membrane thickness depends on the layer arrangement. The aim of these investigations was to find which arrangement provides optimal stress state. Although the analysis was based on the data of CGO material, it might be generalized to all investigated material combinations.

The properties of the most suitable CGO batch 5 (see section 5.2.3) were used in the analysis on different membrane designs. Similar conditions were used for analyzing the asymmetric

membrane assemblies (Figure 4-15), as for the symmetric arrangement given in section 4.3.1. The equivalent substrate thickness was the sum of two supports in the symmetric arrangement. Again the chemical strain was assumed to be 0.2 %. Stress and strain obtained using FEM were taken as critical parameters. For all arrangements the horizontal surface of the substrate on the feed side was vertically constrained (Figure 4-15).

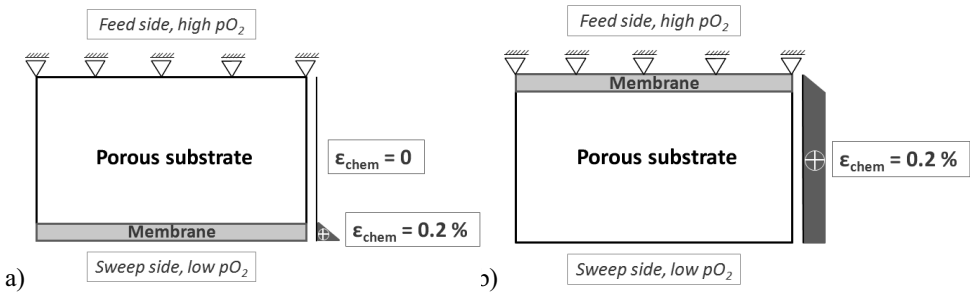

Figure 4–15: *Possible design arrangements of asymmetric membranes.*

4.3.4 Membrane layer failure - Fracture energy criterion

The aim of this analysis was to determine whether the membrane layer will fail under operating conditions. Investigations were limited by the available data to a dense CGO layer on porous CGO substrate, and a dense BSCF layer on porous BSCF substrate.

In the case of CGO, similar conditions as in section 4.3.1 were used, but now the focus was the stress state of the membrane layer which potentially exhibits high tensile stresses. The elastic modulus and fracture toughness for dense CGO were assumed to be 180 GPa and 0.7 MPa√m [148]. The fracture strength of 92 MPa was taken from experimental results of the CGO batch 11 (see section 5.2.3) which had the lowest porosity (12 %). The values of porous CGO batch 5 were taken as input data for the porous substrate.

The chemical strain of 0.018 % (calculation based on literature data [149] for 1 bar air pressure on the feed side and 20 mbar on the sweep side, at 900 °C) was assumed to be constant across the substrate and to linearly decrease from the membrane interface to the free surface (Figure 4-16). All experimentally obtained mechanical properties were taken from room temperature data (section 5.2.3) since the complete data at elevated temperatures were available at the final stage

of the study. However, it was shown that for both materials, CGO and BSCF, the elastic modulus and fracture strength do not change significantly at ~ 800 °C compared to RT (section 6.1).

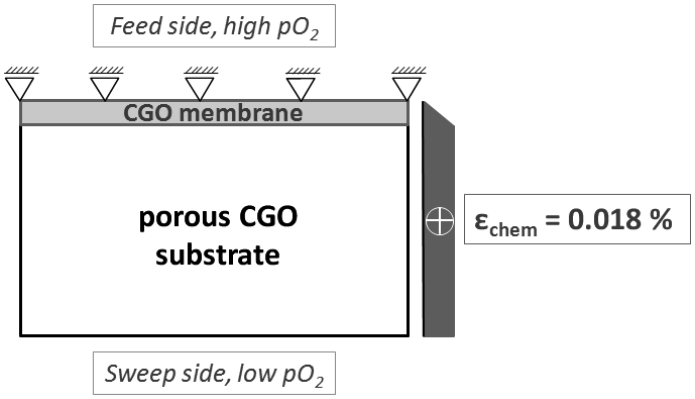

Figure 4–16: Model of CGO membrane (substrate on the sweep side).

The membrane structure was analyzed in a plane stress state, and the resulting stress values were divided by 0.7 to have plane strain solution (plane stress = plane strain × (1 – *v*)) which is more realistic for the membrane geometry. The Poisson ratio *v* was therefore assumed to be 0.3. An asymmetric membrane design, with the substrate on the sweep side was investigated, since it showed optimal stress distribution for the substrate (see section 6.4.3). The thickness of the porous substrate was 0.3 mm, whereas the thickness of membrane layer was varied from 20 µm to 60 µm. The length of the structure was 5 mm. The mesh was generated using 8-node plane stress quadratic quadrilaterals. Simulation was performed with different mesh sizes. The mesh was based on at least three finite elements through thickness of membrane layer, and the same mesh size was used for the substrate. As an example, in the case of substrate and membrane thickness 300 µm and 60 µm, the mesh size was 20 µm (10583 nodes, 3376 elements).

Investigations were also carried out for a dense BSCF membrane on a porous BSCF substrate. Similar loading conditions were used as in the case of the CGO using the data for BSCF given in section 5.2.1. The analysis was based on a chemical strain of the substrate of 0.07 % (calculation based on literature data [150], for 1 bar on the feed side and 20 mbar on the sweep side, at 900 °C), which was assumed to be constant in the porous substrate and to decrease linearly towards the free surface of the BSCF membrane. All mechanical properties were taken from room

temperature calculations. For the fracture toughness of dense BSCF a value of 0.93 MPa√m was used [151]. Based on the experimental results (see section 5.2.1), the elastic modulus and fracture strength were taken to be 52 GPa and 86 MPa for porous and dense BSCF, respectively.

4.3.5 FEM - based validation of ring-on-ring bending test

The analytical approach of ring-on-ring bending test is limited to deflections significantly smaller than the specimen thickness which restricts the applicability of the test. In fact, the critical deflection depends on the ratio of the radii of the loading to supporting ring and is ~ 50 % of the specimen thickness for a support ring to loading ring ratio of two [73,152]. Another complications arise if tests are carried out at thin layered functional ceramics, since differences in thermal expansion of the layers can result in residual stresses and strains causing specimen curvature [153,154]. These limitations can be overcome using finite element analysis in order to predict stresses, even for the non-linear behavior of curved bi-layered materials. For a bi-layered structure, the flexural rigidity will be affected by the presence of an additional layer and the term for a single layer:

$$I_1 = \frac{E \cdot t^3}{12} \qquad 4.11$$

which is a part of Equation 4.2, has to be replaced by:

$$I_2 = \frac{E_S^2 \cdot t_S^4 + E_C^2 \cdot t_C^4 + 2 \cdot E_S \cdot E_C \cdot t_S \cdot t_C \cdot \left(2 \cdot t_S^2 + 3 \cdot t_S \cdot t_C + 2 \cdot t_C^2\right)}{12 \cdot (E_S \cdot t_S + E_C \cdot t_C)} \qquad 4.12$$

where E_s and E_c are elastic moduli of substrate and coating, respectively, and t_s and t_c are thicknesses of substrate and coating, respectively. The analysis was based on SOFC half-cell specimens (see section 4.1.5). The presence of the 10 µm thin coating (YSZ, E_C = 200 GPa, ν = 0.3 at RT) made the entire structure stiffer, yielding a ~ 15 % lower deflection for the composite with oxidized anode in comparison with a monolithic oxidized anode substrate. This was also supported by FEM results. Hence, the effect of the layer cannot be neglected. The factor to be included in Equations (4.3) and (4.4) was:

$$f_1 = \frac{I_2}{I_1} \qquad 4.13$$

The additional layer will not only change the bending stiffness, but also the position of the neutral axis, which needs to be considered in the calculation of the fracture stress by an additional factor:

$$f_2 = \frac{\frac{t_S}{2}}{t_n} = \frac{\frac{t_S}{2}}{\frac{E_S \cdot t_S^2 - E_C \cdot t_C^2}{2 \cdot (E_S \cdot t_S + E_C \cdot t_C)}} \qquad 4.14$$

Furthermore, for a bi-layered material with differences in thermal expansion the total stress is the sum of applied and residual stress. The residual stresses could be calculated analytically based on the temperature dependency of thermal expansion and material properties such as elastic modulus and Poisson´s ratio. Relationships for the substrate stress at the free surface and near the coating interface are given in [155]. A relationship to determine the coating stress from the room temperature curvature is derived in [156]. The stress changes were linear across the substrate. If the room temperature curvature is known, the residual stress in the substrate, at the free surface and near the interface to the layer, could be determined from the room temperature properties using:

a) substrate residual stress - free surface:

$$\sigma_{Rf} = -\frac{1}{6 \cdot r}(3 \cdot E_s \cdot t_c + 4 \cdot E_s \cdot t_s) \qquad 4.15$$

b) substrate residual stress - interface:

$$\sigma_{Ri} = -\frac{1}{6 \cdot r}(-3 \cdot E_s \cdot t_c - 2 \cdot E_s \cdot t_s) \qquad 4.16$$

where r is the curvature radius of the specimen which can be easily obtained experimentally. Higher order terms are neglected in these relationships. The resulting error is equivalent to the relative coating thickness, e. g. for a coating thickness of 3 % of the substrate thickness, the error is 3 %, for a relative thickness of 10 % an error of 10 % is obtained. The advantage of this approach is that, similar as in equations (4.3), (4.3), (4.13) and (4.14), the residual stresses can be determined from room temperature data of elastic modulus and curvature, without considering the thermal history of the system., i.e. knowledge of the stress free temperature and the temperature dependency of the thermal expansion coefficients as well as elastic moduli is not necessary. Based on these analytical results the following procedure can be suggested: (i) to

correct the elastic modulus and fracture stress for the change in flexural rigidity and neutral axis induced by the additional layer (leading to a decrease in deflection and stress at a particular load), and (ii) to add the residual stress, which is the main influencing factor. The correct relationship for the stress is therefore:

$$\sigma_S = (\sigma_b \cdot f_1 \cdot f_2) + \sigma_R \qquad 4.17$$

where σ_R depends on the bending direction, i.e. whether the substrate free surface or the interface is under tensile bending stress. For the deflection of the composite the respective relation is:

$$u_s = (u \cdot f_1) \qquad 4.18$$

Contrary to the concave plate direction, for bending in the convex plate direction, the residual stress counteracts the bending stresses. Hence, elastic modulus and fracture stress can be determined for a composite material using Equations (4.17) and (4.18).

The specimens were supported in the tests by an outer ring ($r_2 \sim 9.5$ mm) and loaded with a smaller coaxial inner ring ($r_1 \sim 4.5$ mm). The circular disc specimens ($r_3 \sim 12.55$ mm) were loaded with a rate of 100 N/min at room temperature in oxidized and reduced anode state, respectively. To test the effect of positioning, either the coating layer (the composite has a concave shape with respect to the loading ring) or the free surface of the substrate layer (the composite has a convex shape, Figure 4-17) was placed on the supporting ring.

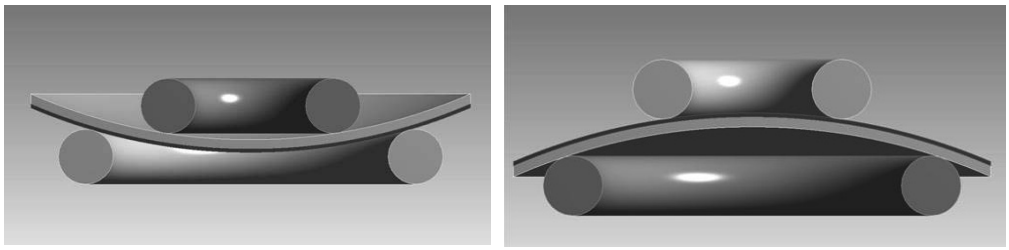

Figure 4–17: Definition of the (a) concave and (b) convex bending direction on cross-sectional models with over-scaled curvature.

The elastic finite element analysis was carried out in static structural mode using 2D axis-symmetry with 2D 8-node elements (PLANE 183). The loading and supporting rings were

approximated by line loads and line supports. The load was applied on one node as the change in loading contact position during bending, according to FEM analysis, showed small influence and thus was neglected. It is verified in [73] that the influence of friction can also be neglected. Geometry and material properties were taken from experimental data and used as input data for the simulation. Although the materials were assumed to be linear elastic, non-linear geometric behavior was taken into consideration using appropriate large deflection settings in the simulation. This option is related to a geometrical non-linearity behavior where the strains, due to change in the model geometry, are calculated and the stiffness contribution (stress stiffness) is added to the structure stiffness matrix. In addition, the instantaneous (deformed) state of the structure is always used in the next increment and updated through the calculation. This ensures that for large deflections the correct inertia forces are calculated.

5 RESULTS

5.1 Ring-on-ring test verification

Since specimen geometries were not clearly defined at the start of the project, it had first to be determined if ring-on-ring bending tests can be used to determine the properties of a curved bi-layered structure. Due to the limited availability of materials at that stage, NiO-YSZ and Ni-YSZ substrates with a dense YSZ membrane layer (see section 4.1.5) were used as model materials in the simulation and compared to available experimental data [139]. The experimental investigations were performed by T. Bause [157].

In the initial stage the layered composite is curved due to the differences in thermal expansion between dense YSZ membrane layer and porous substrate. A curvature radius of 520 mm for a half-cell with oxidized anode can be associated with a compressive stress of ~ −31 MPa at the free substrate surface, while close to the coating interface the substrate stress was ~ 66 MPa. These values were obtained using Equations (4.15) and (4.16), and were additionally verified by FEM analysis. The composites with NiO-YSZ and Ni-YSZ substrate differ in initial deflection due to differences in substrate elastic modulus and thermal expansion.

Initially, the substrate without membrane layer was simulated as a flat isotropic plate with a thickness of 300 μm. For the elastic modulus and Poisson's ratio typical values for NiO-YSZ at RT were used (E = 115 GPa, ν = 0.3). The resulting central deflection– and stress–load dependencies show the expected difference between analytical (Equations (4.3) and (4.4)) and geometrically non-linear FEM solution for large deflections (Figure 5-1 (a) and (b)). Obviously, the thin plate exhibits non-linear behavior when deflection exceeds approximately half the thickness: the specimen becomes stiffer and the deflection is significantly smaller than predicted by the analytical solution.

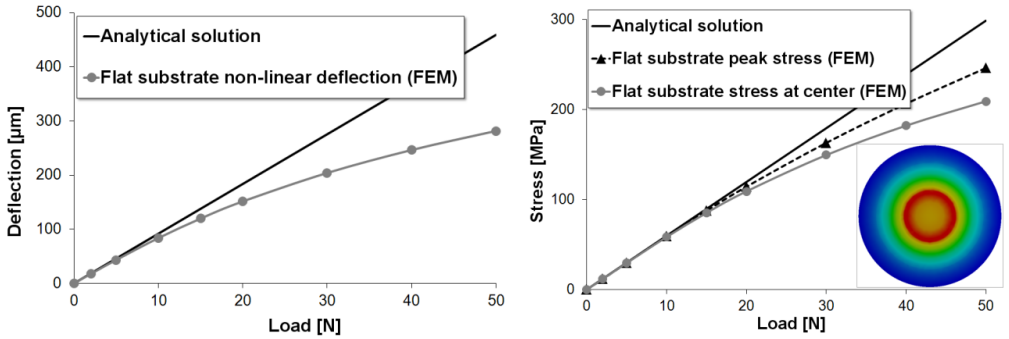

Figure 5–1: Comparison of analytical and FEM results for the (a) deflection– and (b) stress–load behavior of a flat plate. The insert shows the stress localization of the in-plane surface tensile stress for deflection similar to specimen thickness (at load of 50 N).

When the deflection approached the specimen thickness, the tensile stress in the central area inscribed by the loading ring was not constant anymore. A peak stress arose at the opposite side of the loading ring (Figure 5-1 (b), insert).

When a flat substrate with membrane layer was considered, FEA results revealed a similar behavior as for the substrate only. However, the slope of the load–deflection curves changed due to the larger stiffness of the composite. This agreed with the predictions of the analytical approach (Equations (4.17) and (4.18)).

If the same composite specimen was already curved before the test, and placed between the loading and supporting ring in a way that the curvature is increased by the applied load (Figure 4-17 (a), concave plate), the composite showed non-linear behavior already at significantly smaller deflections of ~ ¼ of the total thickness (Figure 5-2 (a)).

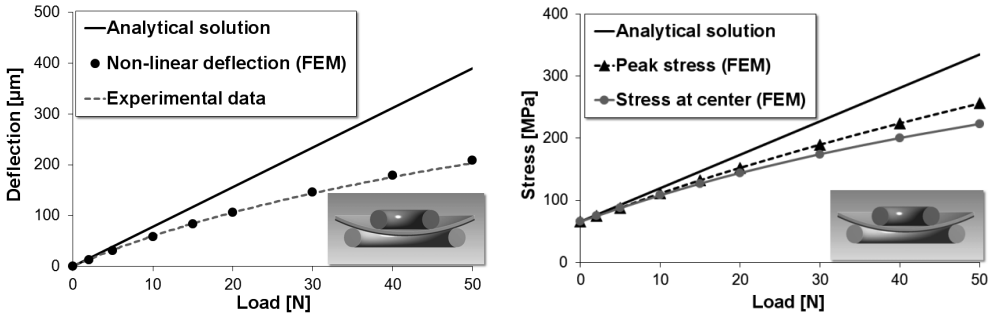

Figure 5–2: Comparison of analytical and FEM results for the (a) displacement–load and (b) stress–load dependencies (concave-shape).

As shown in Figure 5-2, the FEM results showed very good agreement with the displacement–load curve experimentally obtained by T. Bause [[157]]. For stress calculation, only the substrate near the membrane interface was considered as the failure relevant position, since the membrane itself was under compressive stresses of a few hundred MPa. The residual stress was added to the applied bending stress. Hence, the stress–load curve did not start at zero stress (Figure 5-2 (b)). Significantly smaller stresses were obtained than in the analytical approach (Equations (4.17) and (4.18)), and the curves diverged at much smaller deflections than ~ ½ of the thickness. Again a local peak stress arose in the surface opposite to the loading ring at larger deflections (Figure 5-2 (b)).

For the bi-layered composite plate, which was initially curved in convex direction, the curvature resulting from the difference in thermal expansion was reduced during the test (Figure 4-17 (b)), i.e. the specimen was initially flattened by the loading and was then bended in the opposite direction (Figure 5-3 (a)).

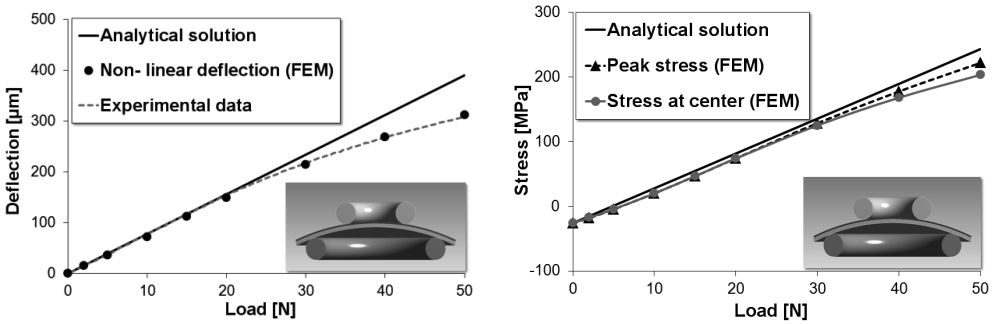

Figure 5–3: Comparison of analytical and FEM results for the (a) displacement–load and (b) stress–load dependencies (convex-shape).

Again the FEM results were in good agreement with the experimentally obtained displacement–load curve by T. Bause [157], as verified in Figure 5-3. Analytical and FEM results agreed up to a deflection of ~ ¾ of the specimen thickness, a larger value than for flat plate and concave bending, since in the case of the convex shape the compressive residual stress counteracted the bending stress (Figure 5-3 (b)). Even at deflections equal to specimen thickness (at load ~ 50 N), analytical (Equations (4.17) and (4.18)), and FEM results showed close agreement (difference < 10 %). A more uniform stress distribution was obtained since the peak stress was reduced in the large deflection regime. Hence, this bending direction is preferable, since it permits an analytical determination of elastic modulus and stress in an even larger deflection range than for flat plates. The substrate can be in an oxidized (NiO-YSZ) or reduced (Ni-YSZ) state. Oxidized and reduced anode differ in elastic modulus (~ 35 GPa reduced, 115 GPa oxidized) and radius of curvature (~ 170 mm reduced, 520 mm oxidized). Hence, these data permit to study the effect of the substrate stiffness and specimen curvature on the mechanical behavior of the composite specimens in a ring-on-ring bending test. Lower elastic modulus and larger curvature affect displacement– and stress–load behavior. Again the FEM results agreed well with the experimentally obtained displacement–load behavior by T. Bause [157], both for initially convex and concave bending direction (Figure 5-4).

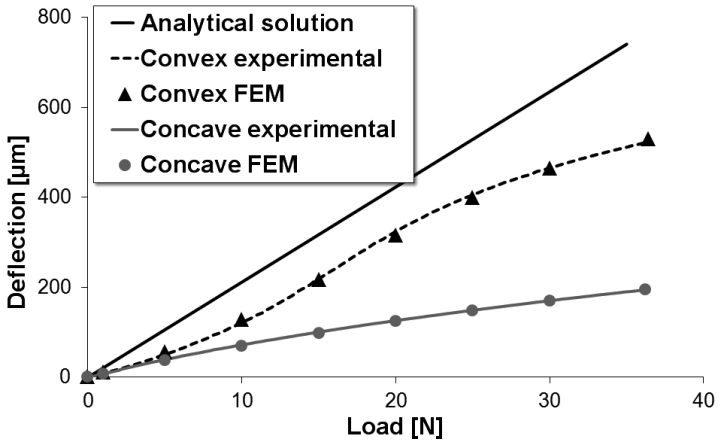

Figure 5–4: Comparison of analytical and FEM results for the displacement–load dependence of different geometry shapes in reduced state.

Due to the larger initial curvature of the reduced samples a larger difference was obtained between analytical (Equations (4-17) and (4.18)) and FEM results in both bending directions (Figure 5-4 and Figure 5-5). For the latter, the parallel shift of the curve caused by residual stresses was not considered in the plot for better visual comparison. As expected, the concave plates exhibited a larger difference to the analytical approach since initial deflection and bending induced deflection are superimposed in the same direction.

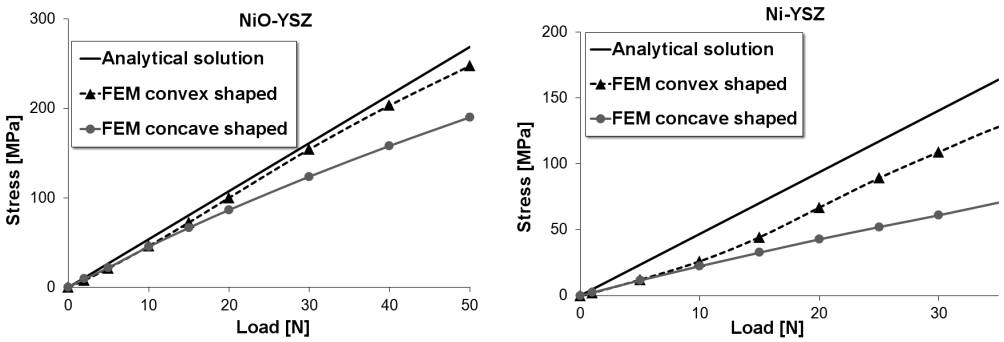

Figure 5–5: Comparison of stress state for different materials and geometry shapes.

To permit further conclusions, additional simulations for the initially convex direction were carried out for oxidized NiO-YSZ specimens with a smaller curvature radius (r ~ 170 mm:

reduced Ni-YSZ specimen at RT), and a reduced specimen with an initially larger radius (r ~ 520 mm, equivalent to an oxidized specimen at RT, similar to the state of the reduced specimens at ~ 800 °C). The results presented in Figure 5-6 show that for smaller initial curvature radius of an oxidized specimen an analytical description of the deformation–load behavior is not possible, even for small initial bending deflections, whereas the reduced specimen with a large initial curvature radius can be described by the analytical relationship up to a deflection of almost its thickness.

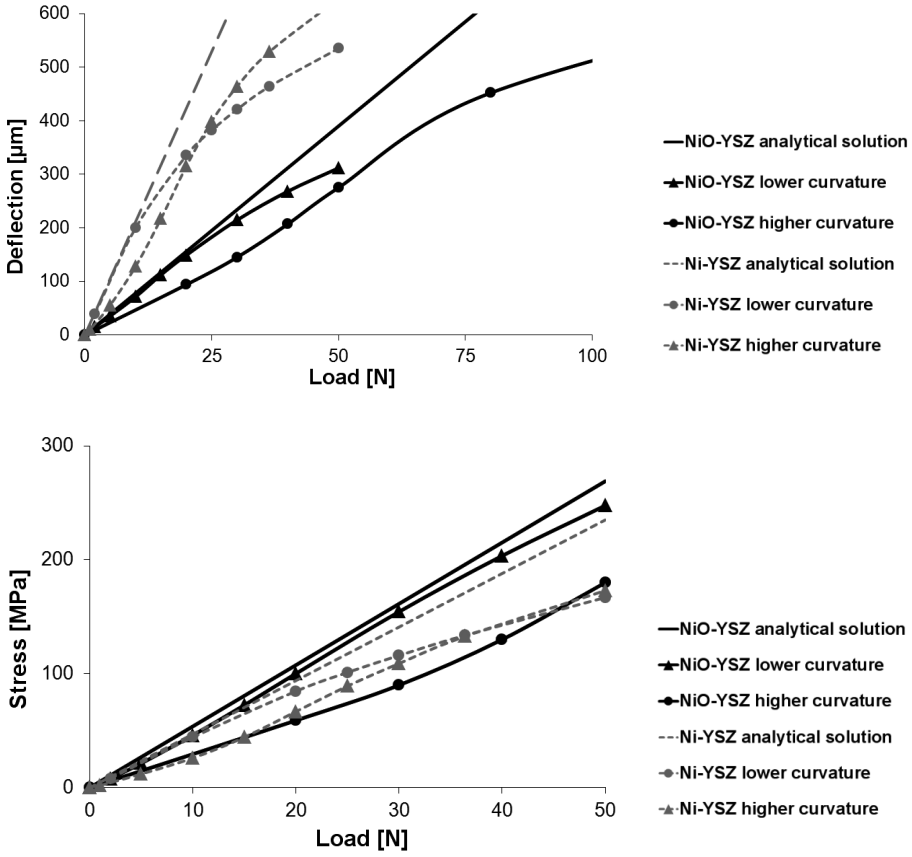

Figure 5–6: Initial curvature influence on (a) displacement–load and (b) stress–load dependencies.

It can be concluded from this section that changes in flexural rigidity, neutral axis, as well as residual stresses related to thermal mismatch, need to be taken into consideration. Simple relationships were given to assess the stress state in the substrate materials based on the room temperature curvature. However, for asymmetrically layered specimens the residual stress is also associated with curvature which influences the behavior in bending tests. Hence, the direction of curvature with respect to the applied loading direction is important. The results clearly showed that the ring-on-ring bending test with the initially convex curvature is preferable. This orientation permits the use of the analytical relationships to an even larger deflection than for a flat plate under identical boundary conditions. However, independent from the substrate stiffness the approach is limited to small initial curvatures (radius ~ 170 mm). The elastic modulus can be determined analytically from bending tests on curved specimens up to a deflection of approximately ¾ the specimen thickness. The analytical approach can be used to determine the fracture stress up to a deflection equal to the specimen thickness for the considered NiO-YSZ composite. For the Ni-YSZ substrate of identical initial curvature, the validity range of the analytical solution is smaller and at a deflection of 1.5 times the initial thickness a difference of 30 % to the analytical solution was obtained. The presented plots can serve as a tool to assess the elastic modulus and fracture stress also at larger deflections and for large initial curvatures where the analytical approach becomes invalid. Although in general FEM based procedures are very valuable, they are not always available and the analysis of materials data has often to be based on analytical procedures. The current work clearly verifies that for the rather complex case of bending of bi-layered materials with initial curvature an analytical analysis procedure is possible. The analytical approach can be extended to multilayer materials using the appropriate relationships for the residual stress, flexural rigidity and position of the neutral axis [[139]].

5.2 Materials characterization

This section compiles the experimental results obtained for the investigated materials (BSCF, LSCF, CGO and FeCrAlY) separately, followed by a comparison in the subsequent chapter. In each section the initial microstructure of the materials is characterized, the elastic modulus and its temperature dependence are given, followed by the failure relevant parameters such as fracture strength and strain, and finally an assessment of creep effects.

5.2.1 BSCF

Microstructure

The microstructure was investigated using thermally etched polished specimens (see section 4.2.4) with an optical microscope and graphically evaluated with the software package AnalySIS (Figure 5-7). Regarding dense BSCF, graphical analysis revealed a porosity of 8.7 ± 1.3 %. According to the manufacturer, porous BSCF had a porosity of 34 %.

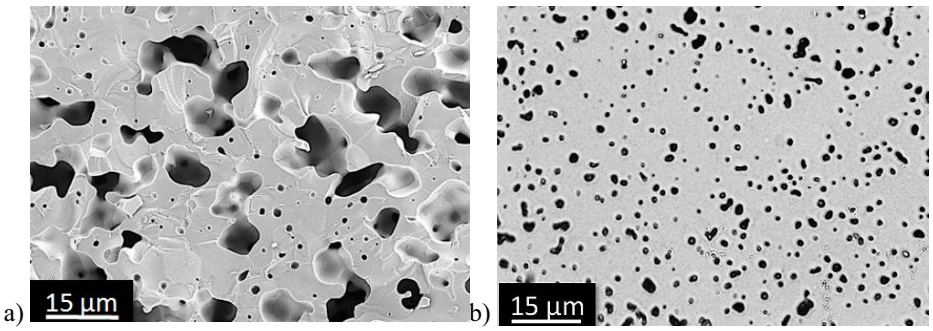

Figure 5–7: Microstructure of (a) porous and (b) dense BSCF material.

Assuming a spherical geometry, the average grain size represented by the equivalent circular diameter was 7.3 ± 2.5 µm. The micrographs are shown in Figure 5-8. The colors illustrate different size classes.

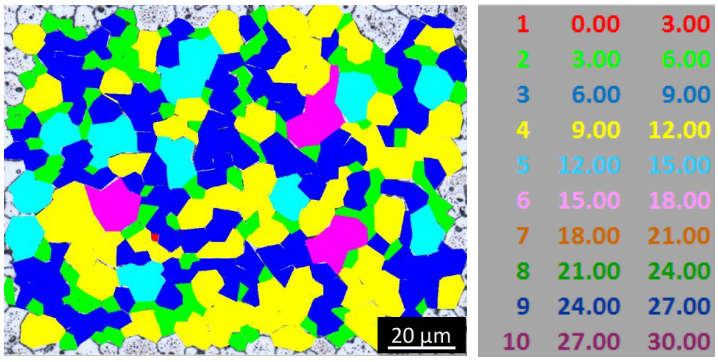

Figure 5–8: Graphical determination of grain size on a thermally etched specimen. Different colors indicate grain size range in µm.

Both, average porosity and grain size yield similar values as reported by Huang et al. [151], who analyzed material produced by the same manufacturer. They reported 4.5 % and 10 ± 4 μm values for porosity and grain size, respectively.

Elastic modulus

Elastic modulus of dense BSCF was determined by ring-on-ring bending test with a loading rate of 100 N/min by Rutkowski [76]. He reported the elastic modulus at RT in air to be 52 ± 1 GPa. The same batch of specimens was analyzed here under different loading rates. There was a negligible effect of the loading rates 1 N/min, 10 N/min and 1000 N/min, since the moduli were 51 ± 3 GPa, 52 ± 1 GPa, and 56 ± 2 GPa, respectively.

Investigations performed on ten porous BSCF specimens (34 % porosity) with a loading rate of 100 N/min resulted in an average elastic modulus of 35 ± 3 GPa. The value agrees very well with the data reported by Lipinska-Chwalek et al. [77]. They analyzed BSCF with 38 % porosity and reported an elastic modulus of 33 GPa.

Fracture strength and strain, reliability

Fracture tests were carried out on porous and dense BSCF in order to determine the characteristic strength. Most ring-on-ring bending tests were conducted with a loading rate of 100 N/min. However, some tests were also carried out with different loading rates in order to assess subcritical crack growth. Hence, the results of the tests with other loading rates are given in the next section.

Maximum likelihood estimation (ISO 20501) was used to determine the characteristic fracture strength and Weibull modulus of porous and dense BSCF. The results are compiled in Table 5-1. For prediction of the fracture stress of a real component and its failure probability, a rescaling with respect to the volume should be carried out (see section 3.2.2).

Table 5-1: Fracture strength of BSCF tested with a loading rate of 100 N/min.

	Dense BSCF	Porous BSCF
Characteristic fracture strength [MPa]	86 ± 4	31 ± 1
Unbiased Weibull modulus	7.0 ± 2.2	8.4 ± 2.7

Rutkowski [76] reported similar values for dense BSCF (porosity 8 %, strength 86 MPa) which he obtained by linear regression analysis of ring-on-ring bending test results. Regarding porous BSCF, the values are also similar as reported in literature (porosity 38 %, strength 34 MPa) [77].

Using Hooke´s law, the individual fracture strains were calculated from elastic modulus and fracture stresses. Maximum likelihood analysis of the data revealed a characteristic fracture strain of 0.17 ± 0.01 % with an unbiased Weibull modulus of 8.3 ± 2.6 for dense BSCF. Regarding porous BSCF, fracture strain and unbiased Weibull modulus were 0.09 ± 0.01 % and 6.2 ± 2.0, respectively.

Subcritical crack growth

Fracture stress values were also analyzed statistically to determine characteristic strength and Weibull modulus at different loading rates. The results obtained by maximum likelihood analysis are given in Table 5-2.

Table 5-2: Characteristic fracture strength and unbiased Weibull modulus as a function of loading rate.

	1 N/min	10 N/min	100 N/min	1000 N/min
Dense BSCF				
Characteristic fracture strength [MPa]	85 ± 6	83 ± 4	86 ± 4	102 ± 9
Unbiased Weibull modulus	7.1 ± 3.6	6.4 ± 2.0	7.0 ± 2.2	5.2 ± 2.3
Weighted mean Weibull modulus	6.5 ± 0.7			
Lower (95 %) / upper (5 %) confidence bounds	4.8 / 8.0			
Porous BSCF				
Characteristic fracture strength [MPa]	28 ± 2	25 ± 2	31 ± 1	29 ± 2
Unbiased Weibull modulus	5.2 ± 1.6	3.8 ± 1.3	8.4 ± 2.7	4.0 ± 1.3
Weighted mean Weibull modulus	5.4 ± 1.9			
Lower / upper confidence bounds	4.2 / 6.5			

The weighted mean evaluation was based on the number of tests at each loading rate. Due to high standard deviations, Weibull moduli of 7 and 5 were assumed for further analysis of dense and porous BSCF, respectively.

Figure 5-9 is a graphical representation of the characteristic fracture strength of BSCF as a function of loading rate. The resulting SCG parameters (see section 3.2.3) were determined from the slope and are given in Table 5-3 with their standard deviations.

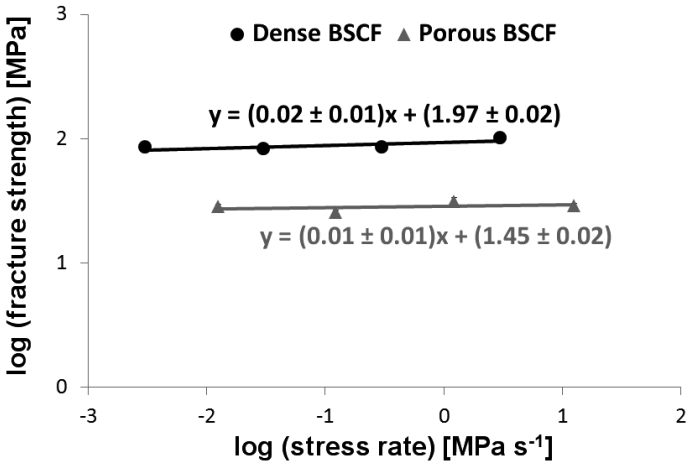

Figure 5–9: Fracture strength of BSCF at room temperature as a function of loading rate.

Table 5-3: SCG parameters of dense and porous BSCF.

Material	*n* parameter	*D* parameter
Dense BSCF	40^{+54}_{-15}	94^{+5}_{-5}
Porous BSCF	$83^{+\infty}_{-50}$	29^{+1}_{-2}

The upper standard deviation of *n* for porous BSCF was calculated to be -172, which is an unrealistic value. This value can occur when the slope decreases with the stress rate, which cannot be correct since in case of no subcritical crack growth the curve is parallel to X-axis, and *n* is infinite.

The differences of the Weibull moduli m_{SCG} and m_{inert} (see section 3.2.3) for dense and porous BSCF were only 7 % and 4 %, respectively, which was significantly smaller than the standard deviation of the Weibull modulus.

Fractography

Microstructural analysis of the ring-on-ring specimens revealed transgranular fracture at room temperature, similar as reported in literature for BSCF for the whole temperature range from RT up to 900 °C [158]. This suggests that BSCF has rather strong grain boundaries. The analysis performed on porous BSCF revealed the same result (Figure 5-10). Moreover, this failure mode was found to be representative for all specimens tested with different loading rates.

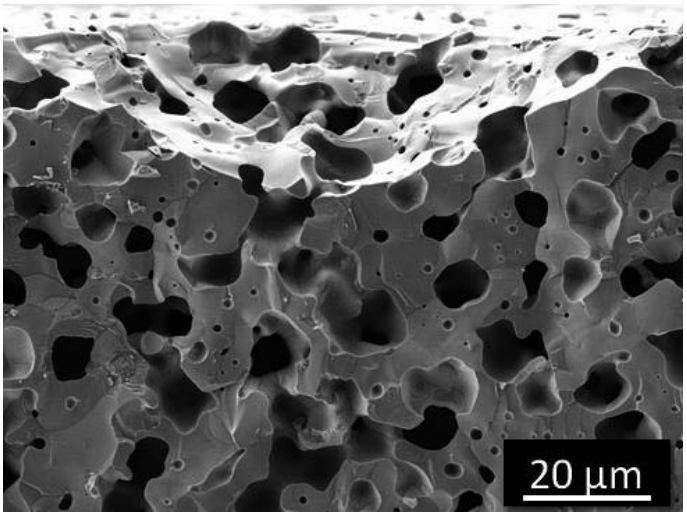

Figure 5–10: Transgranular fracture surface of porous BSCF after loading at RT with 1 N/min loading rate.

Fractographic analysis of the broken specimens revealed that volume defects were the most likely failure origins (pores that might be a result of local differences in densification or shrinkage, Figure 5-11). Similar observations were reported by Rutkowski for BSCF supplied by another producer [76].

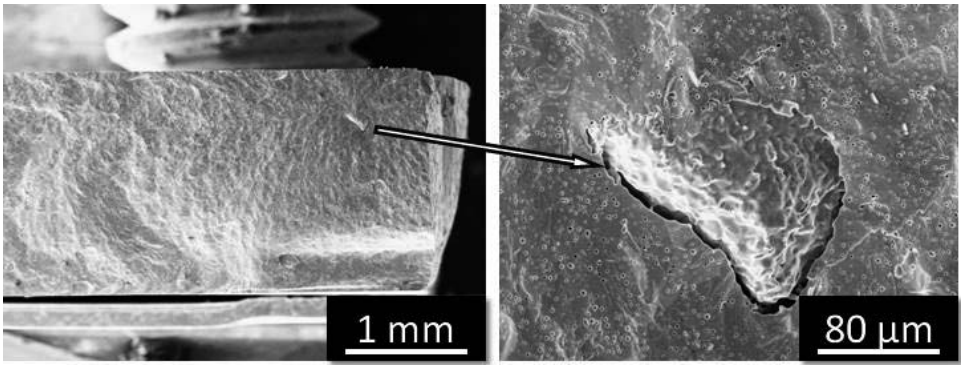

Figure 5–11: SEM images showing the failure origin of a dense BSCF specimen tested in ring-on-ring test at RT with 10 N/min loading rate.

Creep rupture

Three-point bending creep tests were carried out at 850 °C and 900 °C at dense BSCF. Porous material became available at a late stage of the project, hence creep rupture tests could not be carried out on such specimens. At 800 °C the creep deformation was too small to lead to failure in a sufficiently short time. The resulting creep rupture time versus the nominal applied stresses are illustrated for 850 °C and 900 °C in Figure 5-12.

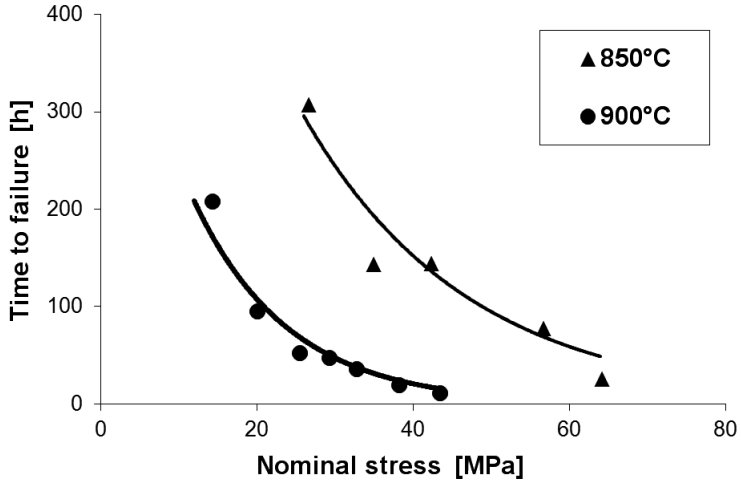

Figure 5–12: Time to rupture in 3-point bending creep tests.

A micrograph of a specimen after creep testing in Figure 5-13 shows microcracks along the grain boundaries near the outer surface. Contrary to specimens which were tested for fracture strength at RT, the creep specimens revealed intergranular crack growth.

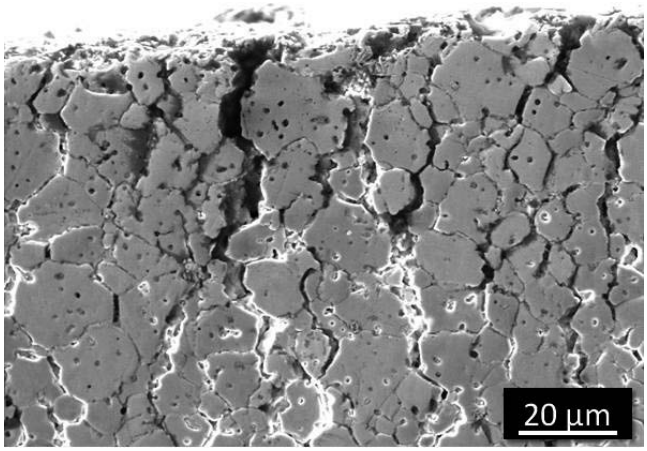

Figure 5–13: Intergranular crack-openings on the tensile side after creep testing at 850 °C for 140 hours.

Similar creep damage features are reported for high temperature creep rupture tests of alumina [110,122 ,159,160]. Although the experimentally straightforward three-point bending test permits determination of rupture time as a function of the applied stress, it does not provide any information on the actual failure strain. Furthermore, differences in creep rate under tensile and compressive load are reported for ceramic materials [161,162], an effect which also needs to be verified experimentally for BSCF. In order to assess these important aspects, additional bending tests with interruptions after defined times were performed. The specimens were cooled down after unloading. Because the deflection of specimens induced by creep deformation did not change during unloading, relaxation effects on the strain measured at the tensile surface were not expected. The strain distribution was measured after cooling down to room temperature by comparing the distance between the rows of hardness impressions (see section 4.2.1) in the cross-section before and after creep testing stages.

Unpolished specimens without impressions yielded similar time to rupture as specimens with impressions, and therefore proved that the effect of impressions on creep rupture is negligible.

The creep tests analyzed with respect to the strain distribution were performed at 900 °C with a nominal applied stress of 15 MPa. The distance between the rows of hardness impressions (initially ~ 120 μm) was re-measured after cooling down to room temperature after 25 h and again after additional 25 h of creep loading under the same conditions. The resulting strain rate as a function of the relative position with respect to the specimen thickness is given in Figure 5-14.

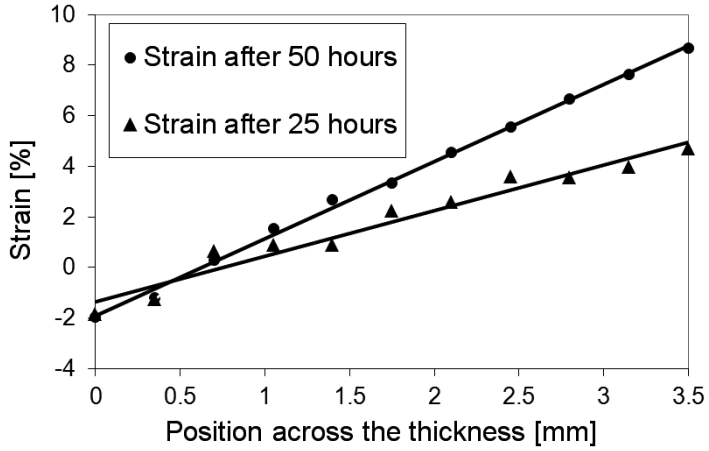

Figure 5–14: Strain distribution measured at the cross-section by the change in distance of hardness impressions (900 °C, time interval 25 h).

After the first 25 h of creep a maximum compressive strain of ~ (−1.5 %) and a maximum tensile strain of 4.5 %, respectively, were obtained by linear fitting of the measured local strains. After 25 h additional creep time, the total compressive strain remained nearly unchanged at −2 %, whereas the tensile strain increased to almost 9 %. This difference in deflection was therefore mainly caused by crack opening on the tensile side. Hence, the apparent strain was larger compared to the elastic theory. From the strain data obtained from the displacement of the indentations, a compressive strain rate of 2×10^{-7} s^{-1} was determined for the first 25 h interval, which is in a rough agreement with literature data of 3×10^{-7} s^{-1} for a compressive creep test at the same temperature and applied stress [109]. The tensile strain increased from 4.5 % for the first creep loading step to 9 % after an additional creep time of 25 h, implying that the tensile strain rate was nearly constant in spite of the crack-openings at the tensile surface.

Lifetime predictions

Failure by subcritical crack propagation at room temperature, and creep failure at elevated temperatures were considered for lifetime prediction. At room temperature, the prediction was based on a strength-probability-time diagram, whereas creep rupture and the Monkman-Grant relationship were considered for creep life analysis at elevated temperatures. Creep investigations were only performed on dense BSCF due to the late availability of porous material, whereas SPT plots for room temperature failure were used to characterize dense and porous BSCF.

Strength – probability – time diagram

The results of subcritical crack growth analysis were used as input data for lifetime predictions. Initially, the stress as a function of loading rate was converted to a constant stress that would cause the sample to fail when the load is held for 1 s (procedure described in section 3.3.1). For dense BSCF, σ_{1s} = 96 MPa was obtained for a failure probability of 63.2 %. Combination of fracture strength and Equation (3.17) yielded the first data point in the SPT diagram (Figure 5-15). Drawing a line across the σ_{1s} data point with the slope of the measured Weibull modulus m = 7 gave the fracture strength estimation at a constant load held for 1 s for all failure probabilities. The prediction of different lifetimes was performed using Equation (3.18). Therefore, in order to calculate the lifetime for A seconds, the 1 s line was shifted by $(\ln x\ A)/n$. As an example, the prediction calculated for 40 years lifetime is plotted in Figure 5-15 and discussed in more detail.

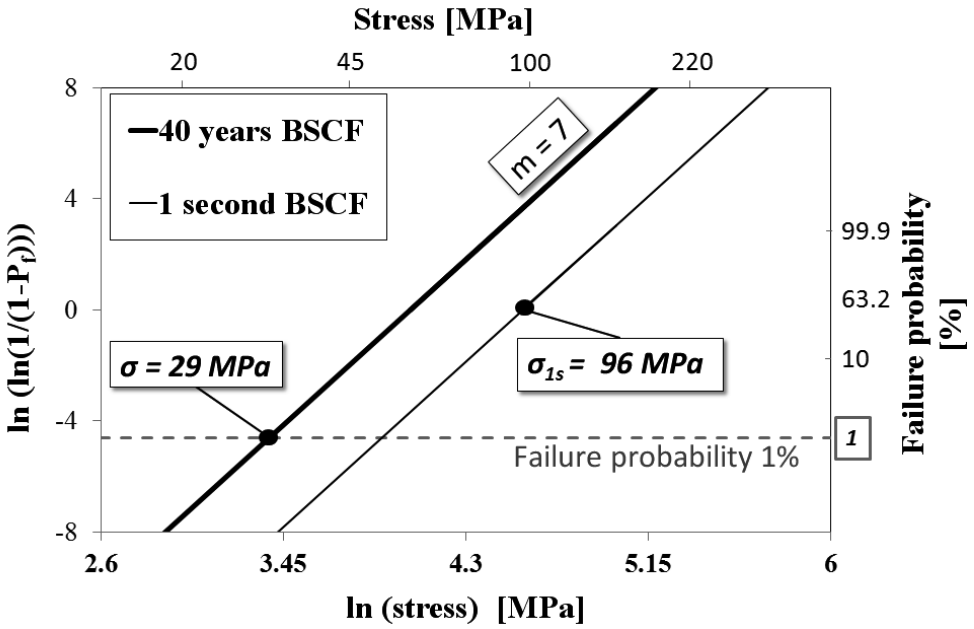

Figure 5–15: Strength-probability-time diagram for BSCF at RT.

Based on the SPT diagram, the design stress for an acceptable failure probability can be estimated. For example, the constant stress for a lifetime of 40 years should not exceed 29 MPa to warrant a failure probability of 1 %. As expected, calculations carried out on porous BSCF revealed lower tolerable stresses. In particular, for the same failure probability porous BSCF should not be constantly loaded with stresses higher than 9 MPa in order to achieve lifetime of 40 years. Details are given in Table 5-4.

Table 5-4: SPT parameters for dense and porous BSCF.

Material	Weibull modulus	σ_{1s} [MPa] for P_f = 63.2 %	σ_{40} [MPa] for P_f = 1 %
Dense BSCF	7	96	29
Porous BSCF	5	29	9

The determined fracture stresses are valid for a specific deformed volume, since the failure probability is a function of the relevant defect number which depends on the specimen volume. Hence, for practical application, rescaling to the volume of the real component using Equation (3.4) is necessary.

Creep rupture

Based on the data presented in Figure 5–12, it can be estimated that the specimen which failed at 900 °C / 20 MPa after ~ 210 h was deformed to a maximum apparent tensile strain of ~ 40 %, which is then equivalent to the rupture strain of this material. The failure time (Figure 5–12) appears to scale approximately with the inverse of the squared stress. Hence, in order to operate the component for 40 years in similar stress distribution, the applied stress should be reduced to less than ~ 0.4 MPa. It is shown that at 800 °C the creep rate is approximately a factor of ten lower [110] implying that the stress leading to failure in 40 years should be less than ~ 4 MPa at this temperature. However, there is no proof for a constant creep rate during long time and ceramics might never reach such high rupture strains in a homogenous stress application, since bending tests were performed in the present work. The reason for the relatively large strains in Figure 5-12 is solely the support of the damaged regions by the undamaged volume under smaller tensile and compressive stress in a bending test. Any generalization of these results to other loading cases therefore still needs to be verified.

Monkman – Grant

Bending creep BSCF specimens with hardness impressions were used in an additional investigation to describe creep life by the Monkman – Grant relationship, given in Equation (3.19). However, in case of three-point bending tests, as carried out here, the strain at rupture can neither be evaluated analytically, due to inhomogeneous stress state, nor measured using indentation marks since the samples fracture. However, since it was assumed that the strain is proportional to deflection, the strain to rupture might be replaced by the deflection at rupture, yielding:

$$\frac{\dot{\varepsilon}_{min} \cdot t_r}{d_r} = C_{MMG} \qquad 5.1$$

The proportionality constant C_{MMG} determined under different applied stress yielded rather constant values for 850 °C and 900 °C, as illustrated in Figure 5-16, with an average value of (6 ± 1) × 10^{-2} mm^{-1}.

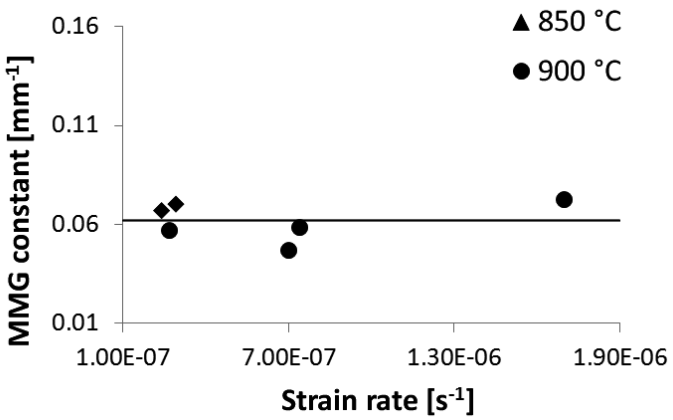

Figure 5–16: Modified Monkman-Grant constant for BSCF.

Although the analysis verifies that creep rupture behavior can be described by a modified Monkman–Grant equation, the relationship cannot be used to predict lifetime since the deflection at failure needs to be known. The analysis outlined above based on the data represented in Figure 5-12 appears to be a more suitable tool for the prediction of time to failure under 3-point bending creep. However, it is verified that in the range where experimental data can be described by a Monkman–Grant relationship, failure was creep damage controlled and rather independent of preexisting cracks that blunt due to diffusion induced plastic deformation at elevated temperatures [159].

5.2.2 LSCF

Results of investigations performed on dense LSCF are given in the following sections. The investigations were carried out to analyze the microstructure, mechanical properties, SCG sensitivity, creep rupture time and to perform lifetime prediction based on the SPT diagram. Porous material could not be investigated since it was not available during the time of the project.

Microstructure

The microstructural investigation revealed a rather inhomogeneous porosity of the LSCF material. Pore clusters were found in all specimens (Figure 5-17), where the porosity locally reached values up to 4.1 ± 0.1 %.

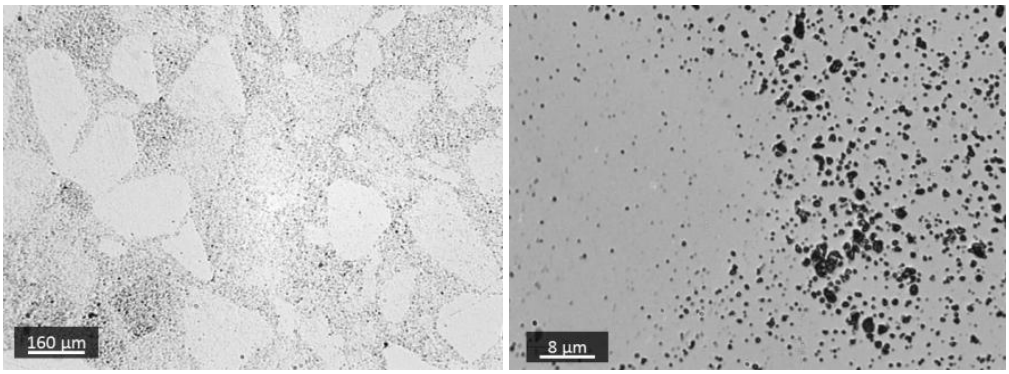

Figure 5–17: Inhomogeneous pore distribution in LSCF in different magnifications.

Determination of grain size was based on several representative SEM images. An example is given in Figure 5-18. Previously, the surface was thermally etched in order to enhance grain boundary visibility (see Table 4-8). Graphical analysis, based on the equivalent circular diameter, revealed an average grain size of 0.9 ± 0.4 µm, similar to the 0.6 ± 0.2 µm reported by Huang et al. [82] for LSCF material produced by the same manufacturer.

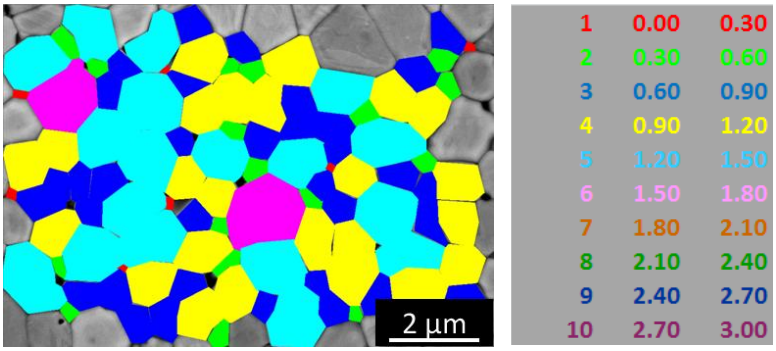

Figure 5–18: Example of the grain size evaluation at LSCF. The colors indicate ten grain size ranges up to 3 µm.

Elastic modulus

Ring-on-ring bending tests carried out at the standard loading rate of 100 N/min revealed an average elastic modulus of 44.6 ± 19.6 GPa. The specimens were tested in the as-received state. Huang et al. [45] reported an elastic modulus of 72 GPa for specimens which were previously grinded to achieve high flatness. This suggests that the elastic modulus measured in the present work was biased by specimen waviness which appeared to influence results of the ring-on-ring test. The comparatively high standard deviation also confirmed this assumption.

Similar as reported by Huang et al., the curves showed non-linear load-displacement behavior. They assigned this anomaly to the ferro-elasticity of the rhombohedral phase, which does not exist in the high temperature cubic symmetry. Load-displacement curves are given in Figure 5-19. The black curve is a representative example which clearly shows the non-linear behavior.

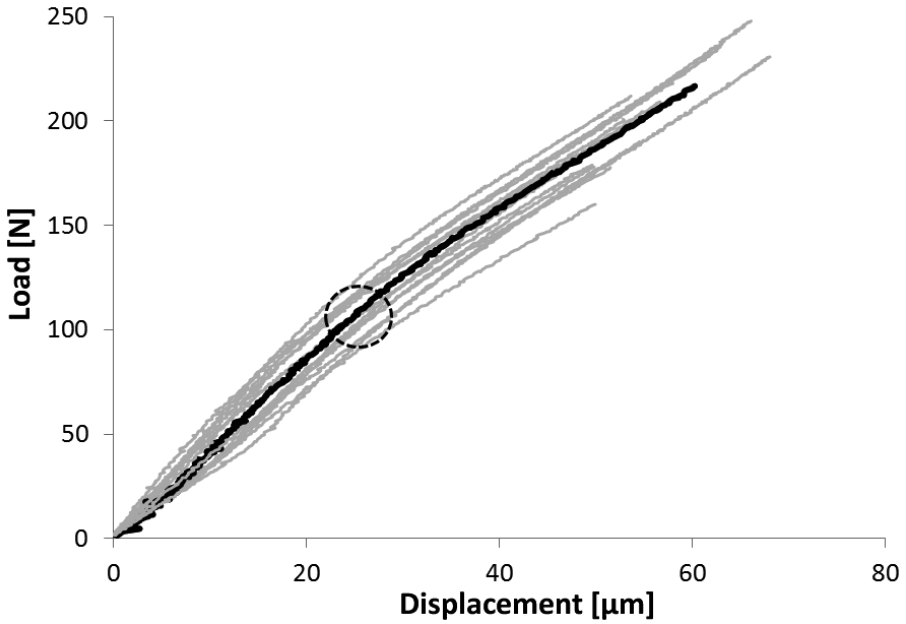

Figure 5–19: Load-displacement curves of LSCF revealing elastic modulus. The dashed circle indicates beginning of non-linear behavior.

Fracture strength and strain, reliability

Ring-on-ring bending tests were also carried out to evaluate fracture strength and strain together with their reliabilities. A loading rate of 100 N/min was applied. Tests with other loading rates were used for SCG analysis and these results are therefore presented in the next section. The calculation was based on the maximum likelihood estimation. The fracture strength was 73 ± 2 MPa, similar to the value of 70 MPa reported by Huang et al. [82]. The unbiased Weibull modulus was 10.7 ± 2.8.

Based on the same analysis as outlined above for BSCF, the characteristic fracture strain of LSCF was 0.22 ± 0.01 %. The unbiased Weibull modulus of fracture strain was 10.1 ± 2.6.

Subcritical crack growth

The loading rate sensitivity of the fracture stresses at room temperature was analyzed statistically to determine characteristic fracture strengths and Weibull moduli. The values obtained by maximum likelihood method are given in Table 5-5.

Table 5-5: Characteristic fracture strength and unbiased Weibull modulus of LSCF as a function of loading rate.

	1 N/min	10 N/min	100 N/min	1000 N/min
Characteristic fracture strength [MPa]	69 ± 1	64 ± 4	73 ± 2	76 ± 1
Unbiased Weibull modulus	27.5 ± 13.8	7.7 ± 3.9	10.7 ± 2.8	28.8 ± 14.4

Based on the number of tests at each loading rate, the weighted mean Weibull modulus was 15.4 ± 8.5, while the lower and upper confidence bounds were 11.3 and 19.0, respectively. Due to the high standard deviation, an average Weibull modulus of 15 was used in the subsequent analysis. Figure 5-20 is a graphical representation of the respective fracture strengths versus loading rate for LSCF. The resulting SCG parameters (see section 3.2.3) were determined from the fit, yielding $n \sim 49$ and $D \sim 73$ MPa. The asymmetric standard deviation for n parameter was

49^{+96}_{-19}, implying that even though there is a large scatter, the material´s relatively low sensitivity to SCG can be confirmed.

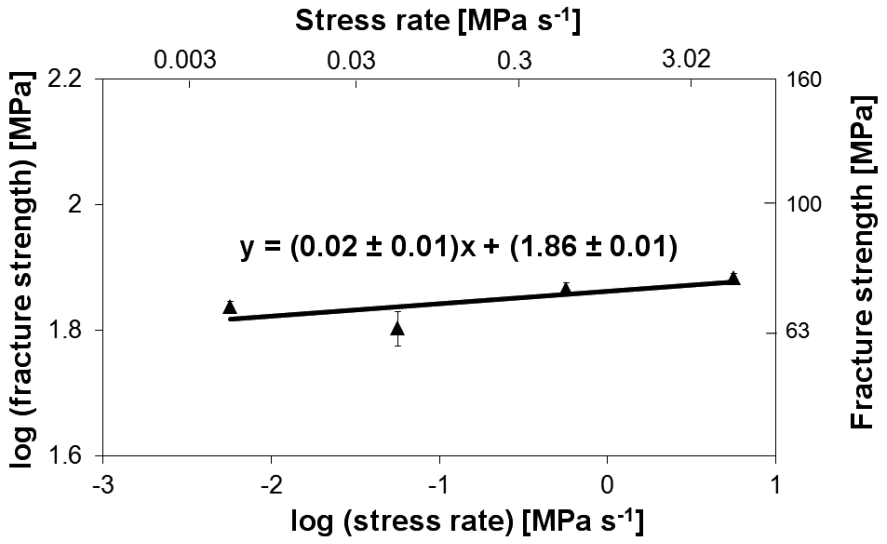

Figure 5–20: Subcritical crack growth sensitivity of LSCF.

The difference between m_{SCG} and m_{inert} (see section 3.2.3) was only 6 %, which was significantly smaller than the standard deviation of Weibull modulus.

Fractography

Fractographic analysis revealed that volume defects were the failure origin in most cases (Figure 5-21). These volume defects were mainly large pore clusters, already reported as typical fracture origin for LSCF [[163]]. The determined fracture stresses were characteristic for a specific deformed volume, and therefore, for practical application, a rescaling to the volume of a real component using Equation (3.4) is necessary.

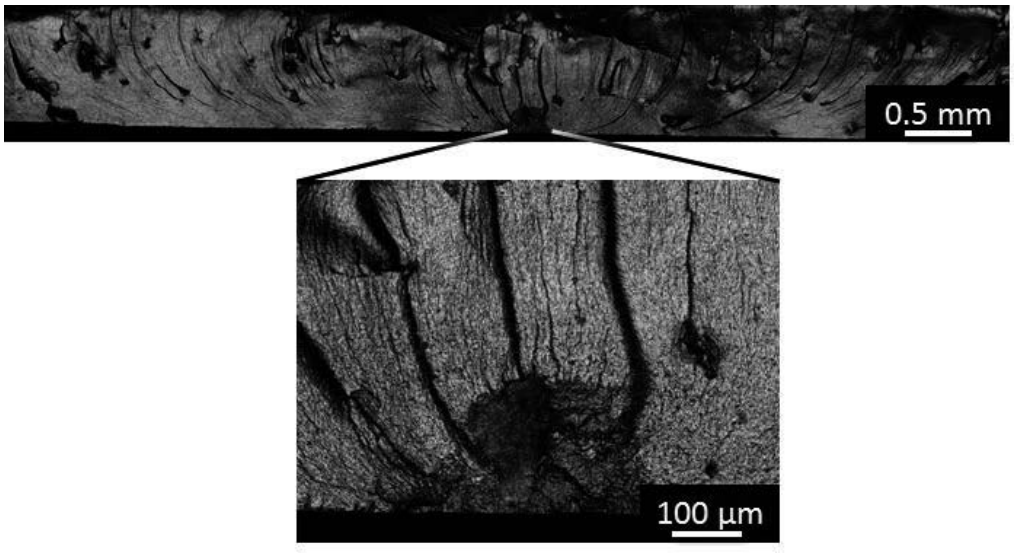

Figure 5–21: Volume defect in a facture surface of LSCF loaded with 10 N/min at RT in different magnifications.

Creep rupture

Due to limited materials availability and restrictions in testing time, only a limited number of specimens were tested in order to permit a comparison with the rupture behavior of the other materials. LSCF was creep tested in 3- point bending at 900 °C. The first specimen, loaded with a nominal maximum stress of 43 MPa, failed after 226 hours. A second test under 33 MPa nominal maximum stress was stopped after 5 hours since the specimen revealed a very low creep deformation (only 30 µm). Consequently, creep rupture of the material in a reasonable time was not expected under such conditions, which confirms the high creep resistance observed in the first test.

Lifetime predictions

The strength-probability-time diagram was used for lifetime prediction at room temperature. The evaluation was based on subcritical crack growth analysis and fracture strength with its reliability similar as for BSCF.

Strength – probability – time diagram

According to Equation (3.17), the minimum stress which LSCF material can withstand for a failure probability of 63.2 % under constant load held for 1 s was determined to be σ_{1s} = 74 MPa. Taking into account a Weibull modulus of 15 and the σ_{1s} data point, the prediction line was plotted for critical constant stress held for 1 s as a function of the failure probability. By parallel shifting of this line using Equation (3.18), a prediction line for 40 years lifetime was determined. The respective plot is displayed in Figure 5-22.

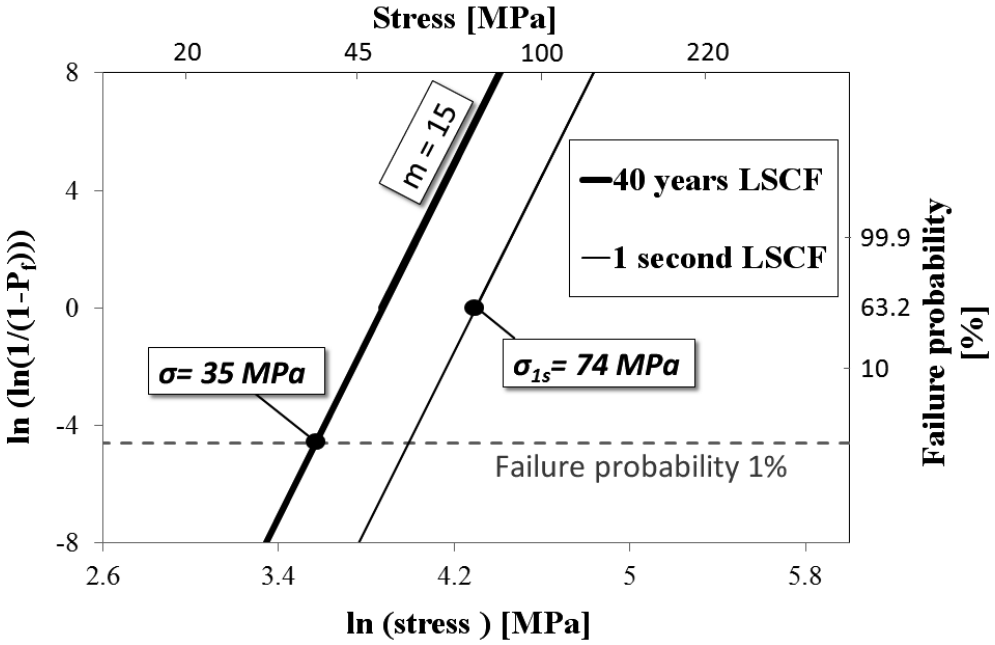

Figure 5–22: 1 s and 40 years lifetime prediction for LSCF at RT.

According to the SPT diagram, for a failure probability of 1 %, LSCF can withstand a constant stress of 35 MPa for 40 years in case of the applied ring-on-ring bending configuration.

5.2.3 CGO

Results for porous CGO are given in the following sections. Dense material was not available during the time of the project. Eleven CGO batches were produced by the project partner DTU

Energy Conversion within the framework of their materials development (see section 4.1.3). Preparation conditions and porosities were varied (Table 5-6), which were expected to influence the mechanical properties. Hence, one aim of the current study was to provide data as a baseline to optimize the CGO production. Investigations included fracture tests in air at room temperature for determination of the elastic and fracture properties. It should be noted that for batches 6-11 sintering time and temperature were the only varied parameters, and therefore only these batches permit an unbiased comparison of the effect of porosity on the mechanical properties.

Table 5-6: *Preparation conditions and resulting porosities of the CGO batches.*

Batch	1	2	3	4	5	6	7	8	9	10	11
Sintering time [h]	12	12	12	4	4	4	4	4	4	4	4
Sintering temp. [°C]	1300	1300	1300	1050	1050	1050	1150	1250	1050	1150	1250
Porosity [%]	29	21	16	38	36	56	40	27	43	29	12

Microstructure

The microstructure of all as-received CGO material was analyzed. In particular, lots of inclusions and scratches were found in the surfaces (Figure 5-23, image on the left side) of the initially produced batches 1-3. Since these inclusions were quite large, they could be potential failure origins. The inclusions were successfully removed during the further materials development after the production of batch 3 by the manufacturer (Figure 5-23, image on the right side).

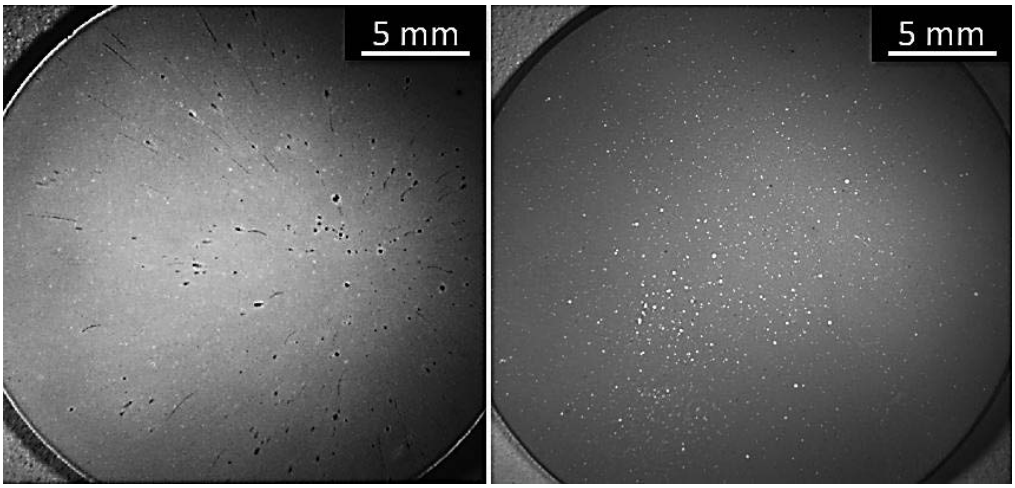

Figure 5–23: Numerous large defects (scratches and inclusions) found in the surface of as-received CGO batch 3(left image) and rather smooth surface of CGO batch 9 (right image). The image on the left hand side is representative surface for batches 1-3, whereas the image on the right hand side represents a typical surface of the improved batches 4-11.

Porosities were determined by the manufacturer based on the SEM microstructural images and are given in Table 5-6. In general, all CGO batches had rather similar grain size. However, slight differences between the batches could be distinguished. Grain size analysis of batches 6-11 revealed a very fine microstructure with an average grain size of 0.33 ± 0.14 μm. Figure 5-24 displays representative images of batches 6-11 revealing the differences in grain size.

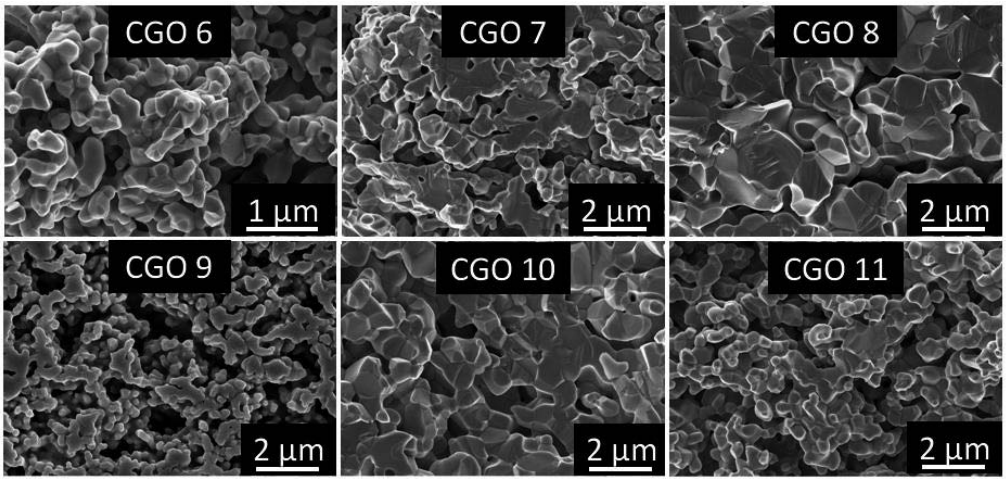

Figure 5–24: Microstructure of CGO batches 6-11, revealing the difference in grain sizes.

A more detailed analysis is presented in Figure 5-25, where the two lines represent batches with different amount of initial pore former. Clearly the grain size increased with sintering temperature. Moreover, the grain size was stronger affected for batches 6-8, hence, grain size was more influenced by the sintering temperature for materials with higher amount of pore former. CGO batch 10 was the only one deviating from this behavior. However, the high standard deviation could imply that CGO batch 10 had a lower average grain size.

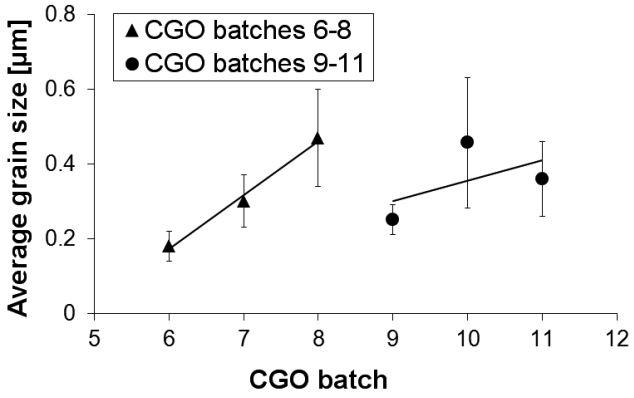

Figure 5–25: Difference in grain sizes for CGO batches 6-11 indicating the influence of sintering temperature and porosity.

Elastic modulus

Thin round plates were tested in ring-on-ring bending at RT. The results imply that the sintering temperature influenced the elastic modulus in agreement with the different individual porosity of each batch. All results are given in detail in Table 5-7, and are plotted in Figure 5-26.

Table 5-7: *Elastic moduli of CGO at RT.*

Batch number	*1*	*2*	*3*	*4*	*5*	*6*	*7*	*8*	*9*	*10*	*11*
Number of specimens	*11*	*8*	*7*	*18*	*26*	*10*	*25*	*29*	*28*	*30*	*29*
Elastic modulus [GPa]	***90***	***114***	***118***	***38***	***36***	*/*	***47***	***97***	***57***	***118***	***149***
Standard deviation	*30*	*10*	*32*	*5*	*7*	*/*	*7*	*21*	*14*	*15*	*18*

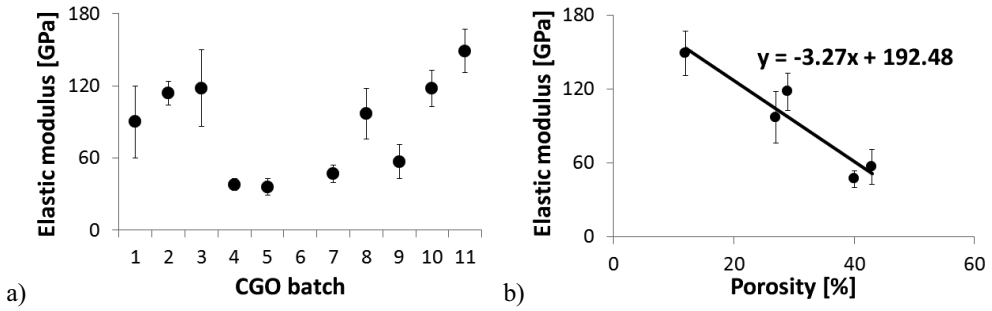

Figure 5–26: a) Elastic modulus of different CGO batches at RT; b) Elastic modulus as a function of porosity for batches 7-11.

The decrease of the elastic modulus of CGO with porosity is illustrated in Figure 5-26 (b). According to the available data, it seems that a good description of the data can be obtained by a linear fit. The data can be compared to [148], who evaluated elastic modulus of dense CGO to be 180 ± 10 GPa. The extrapolated linear trendline in Figure 5-26 yields a similar value of 192 GPa, whereas the Equation (3.16) proposed by Yao [120] results in a value of ~ 210 GPa.

Since the specimens were very thin, the fracture load was rather low. In fact, batch number 6 could not be characterized due to its very low strength, because failure already occurred under the experimentally necessary contact pre-load of 2 N. The elastic modulus was furthermore investigated as a function of temperature (Figure 5-27). Due to limited materials availability, this test was only carried out for batch number 9. The results clearly indicate that the elastic modulus remains rather constant up to 800 °C. Since the temperature dependence of elastic modulus is an intrinsic material property, it should be independent of porosity and it can be assumed that all other CGO batches should have similar behavior.

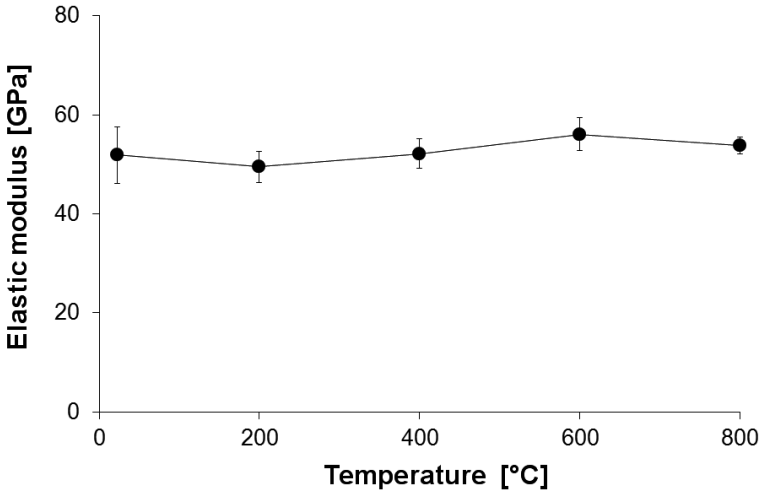

Figure 5–27: Elastic modulus of CGO batch 9 as a function of temperature.

Fracture strength and strain, reliability

The maximum likelihood method was used to determine fracture strengths and Weibull moduli. Fracture strength data are shown in Figure 5-28. The numbers in boxes present the unbiased Weibull moduli. Fracture strength as a function of porosity for the comparable 5 batches is given in a separate figure.

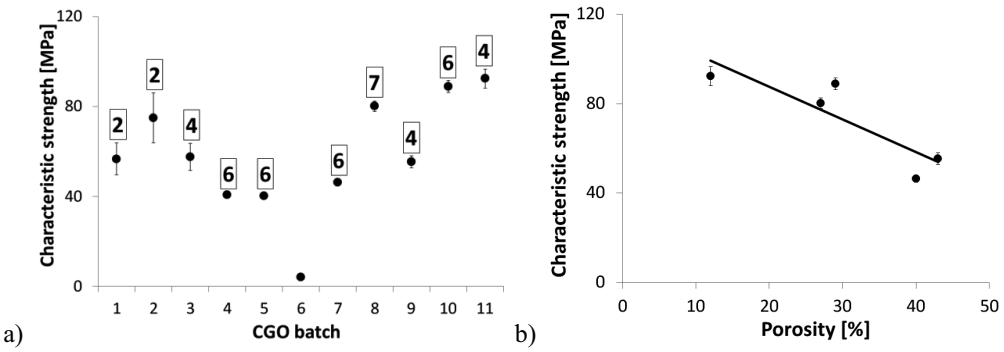

Figure 5–28: Characteristic fracture strength a) of all CGO batches with the corresponding Weibull modulus; b) as a function of porosity for the batches 7-11.

According to the presented data, it seems that fracture strength, similar as elastic modulus, decreases rather linearly with porosity. The higher reliability (larger Weibull modulus *m*) of the CGO batches, starting from batch number 4, was achieved by successful removal of large inclusions found in the initial batches 1-3 (see Figure 5-23). Again, batch number 6 could not be characterized due its very low strength and only an upper fracture strength limit of 4 MPa could be given. Additional fracture tests were carried out for CGO batch 9 at different elevated temperatures up to 800 °C. Contrary to elastic modulus, the fracture strength of CGO appeared to be slightly lower at RT and 400 °C (Figure 5-29). It might be assumed that the other batches show a similar behavior.

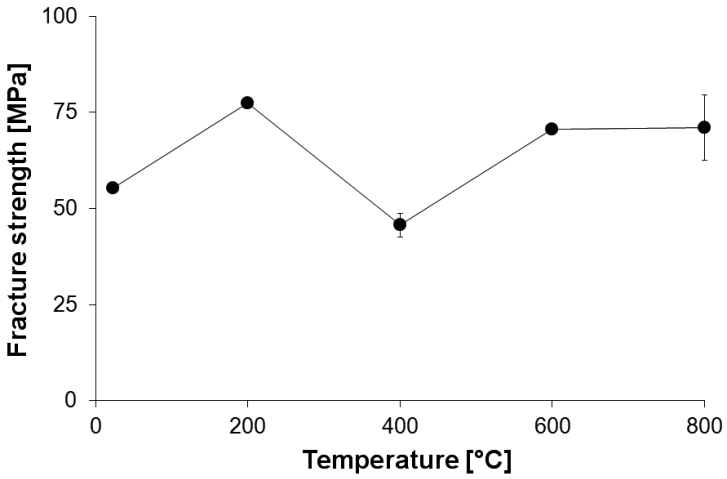

Figure 5–29: Fracture strength of CGO batch 9 as a function of temperature. The line is a guide to the eye.

Based on Hooke´s law, the fracture strains and the corresponding unbiased Weibull moduli were determined and are presented in Figure 5-30.

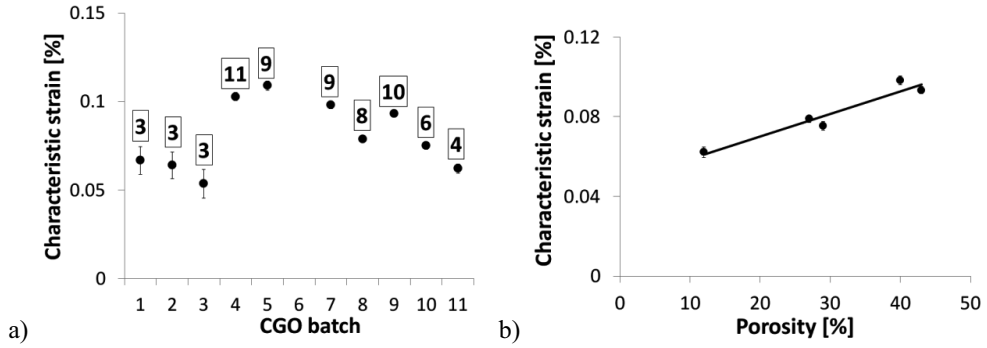

Figure 5–30: Characteristic fracture strain a) of CGO batches with corresponding Weibull moduli; b) presented as a function of porosity.

Contrary to elastic modulus and fracture strength, the fracture strain showed an increase with porosity, which is caused by the lower elastic modulus of the high-porosity batches and furthermore suggests that higher porosity levels aid the dissipation of energy at the crack tip.

Subcritical crack growth

The fracture stress as a function of loading rate obtained at room temperature was analyzed statistically to determine characteristic strength and Weibull modulus. The tests were performed on CGO batch 9 and were evaluated with the maximum likelihood method. The results including uncertainties are given in Table 5-8.

Table 5-8: Characteristic fracture strength and unbiased Weibull modulus of CGO as a function of loading rate.

	0.1 N/min	1 N/min	10 N/min	100 N/min
Characteristic fracture strength [MPa]	45 ± 2	49 ± 10	64 ± 5	55 ± 3
Unbiased Weibull modulus	7.6 ± 3.1	1.9 ± 0.7	3.2 ± 0.9	4.0 ± 0.8

Based on the number of tests at each loading rate, a weighted mean Weibull modulus of 3.9 ± 1.5 was obtained, whereas the lower and upper confidence bounds were 3.2 and 4.6, respectively. The average Weibull modulus of 4 was used in the subsequent analysis.

Figure 5-31 is a graphical representation of the respective characteristic fracture strength data of CGO. The resulting SCG parameters (see Equation (4-6) for CGO) were $n \sim 25$ and $D \sim 56$ MPa. The asymmetric standard deviation for n was 25^{+43}_{-10} suggesting that for CGO subcritical crack growth effects are not negligible.

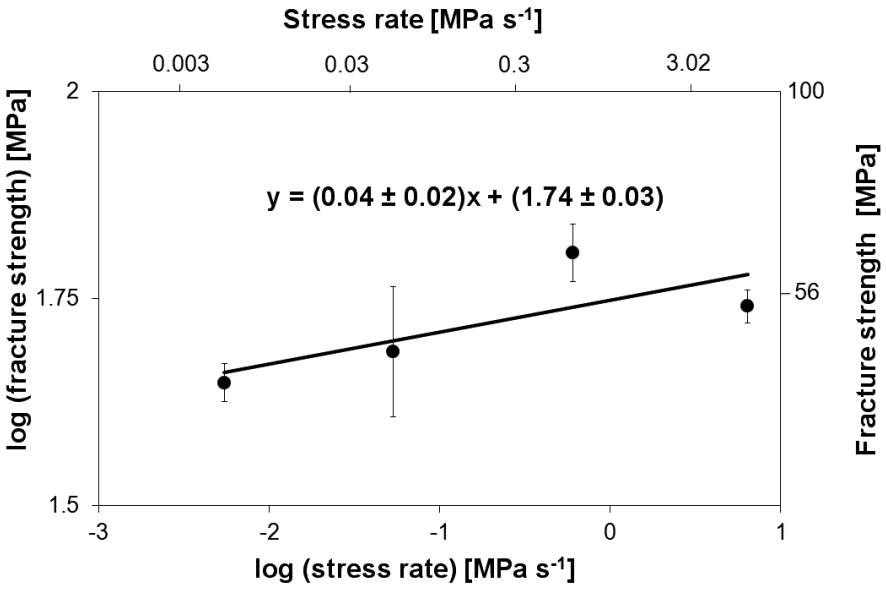

Figure 5–31: Subcritical crack growth sensitivity for CGO batch 9 at RT.

Considering an n parameter of 25 for the current material, the difference between m_{SCG} and m_{inert} was only ~ 10 %, which is again significantly smaller than the experimental uncertainty.

Fractography

Fractographic analysis suggested that volume defects are the main failure origin (Figure 5-32). However, apart from such defects the microstructure seemed to be rather homogenous, almost without significant pore clusters or inclusions. The determined fracture stress values were characteristic for a specific deformed volume, since the probability of failure relevant defects depends on the specimen volume. Hence, for practical application, a rescaling to the volume of the real component using Equation (3.4) is necessary.

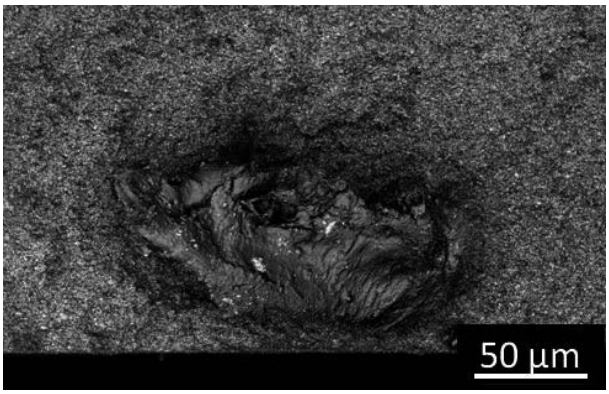

Figure 5–32: Volume defect found in a fracture surface of CGO batch 5 specimen.

Strength – probability – time diagram

CGO batch 9 was used for SPT lifetime prediction. Based on the data from subcritical crack growth analysis, a value of σ_{1s} = 58 MPa was obtained for a failure probability of 63.2 %. An example of lifetime prediction of 40 years is given in Figure 5-33. In this case, the applied stress should not exceed 8 MPa to warrant a failure probability of 1 %.

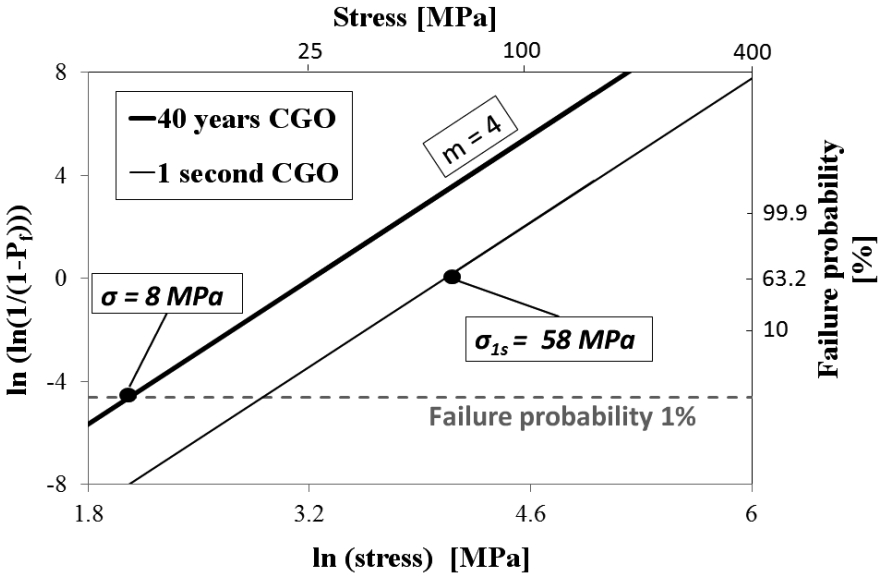

Figure 5–33: SPT prediction diagram for CGO batch 9.

5.2.4 FeCrAlY

Microstructure

Two batches of FeCrAlY alloy (dense and porous - see section 4.1.4) were investigated. Microstructural analysis of the dense FeCrAlY alloy batch revealed an average porosity of 1.0 ± 0.2 % (Figure 5-34).

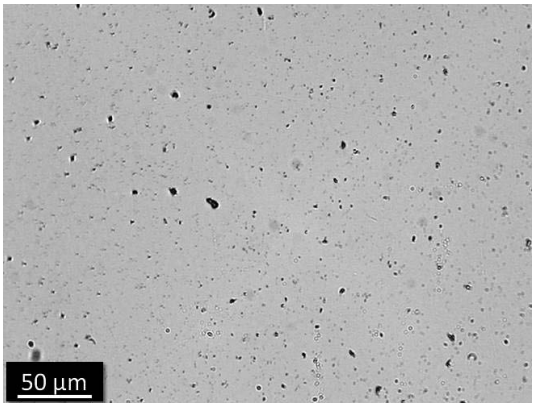

Figure 5–34: Polished microstructure of dense FeCrAlY alloy.

The microstructure of the porous FeCrAlY alloy was also characterized (Figure 5-35). The average porosity was graphically determined to be 35 ± 2 %.

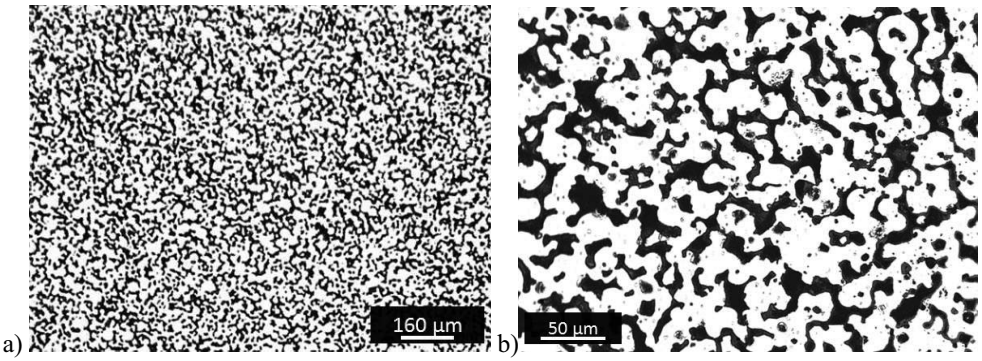

Figure 5–35: Graphical analysis based on the microstructural images of porous FeCrAlY alloy with (a) lower and (b) higher magnification. Both revealed an average porosity of 35 %.

Determination of the grain size was based on microstructural images, as shown in Figure 5-36. Previously, the surface was etched (see section 4.2.4) in order to enhance the grain boundaries´ visibility. Graphical analysis of the equivalent circular diameter revealed an average grain size of 14.7 ± 6.0 µm for the dense material. According to the microstructural images, a similar value can be assumed for the porous material (Figure 5-36).

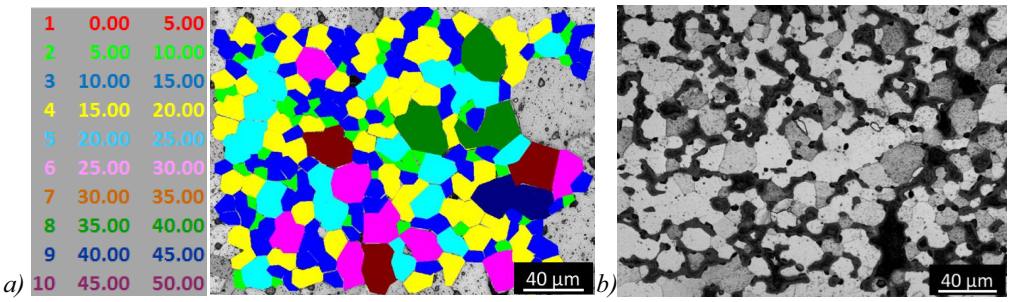

a) *b)*

Figure 5–36: Grain structure of (a) dense and (b) porous FeCrAlY alloy.

Elastic modulus

The elastic modulus of the porous material was determined with three-point bending tests at temperatures up to 600 °C in air. The test at room temperature revealed an elastic modulus of 107.0 ± 0.2 GPa. This value is higher than reported for promising ceramic substrate materials of similar porosity [[151]]. The elastic modulus decreased monotonously with increasing temperature, yielding a ~ 25 % lower value at 600 °C. A comparison of the normalized data of elastic modulus at RT with dense steel X10CrAlSi18 [[86]] shows good agreement of the temperature dependence (Figure 5-37).

The elastic modulus of dense FeCrAlY alloy was measured by micro-indentation. Tests with 1 N peak load revealed an elastic modulus of 164 ± 6 GPa at RT. The value is again similar to that of the dense ferritic steel X10CrAlSi18 (181 GPa [[86]]).

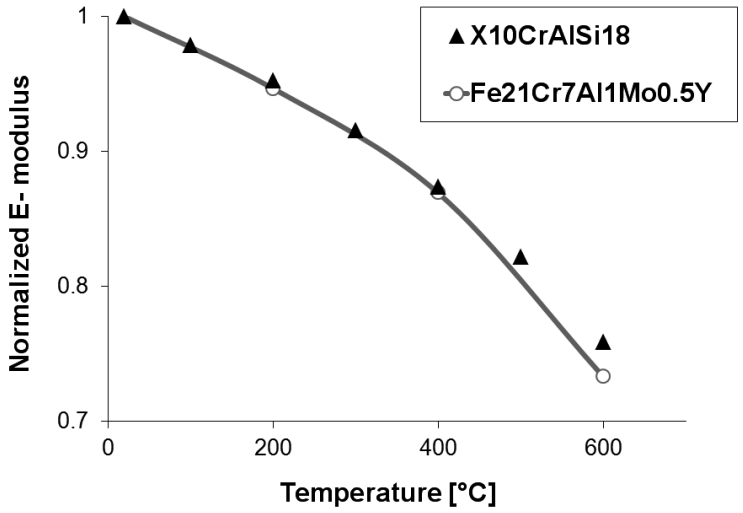

Figure 5–37: Comparison of the normalized elastic modulus of the porous materials with data for X10CrAlSi18 steel.

Fracture strength and strain, reliability

Due to the ductile behavior of the material, no fracture was observed during bending test. Therefore, the fracture strength could not be determined for this material.

Creep behavior

Compressive creep tests (see section 4.2.3) were carried out at 700 °C and 800 °C for dense and porous material, and, in addition, at 900 °C only for the dense material. Although the data for the porous material were not analyzed in detail since due to closure of pores during the test a steady state creep rate could not be obtained, the creep behavior of porous material suggested that the difference between porous and dense material was mainly a result of the smaller effective contact area and, hence, a larger apparent stress occurs in the porous material. Exemplary curves for dense and porous material are shown in Figure 5-38.

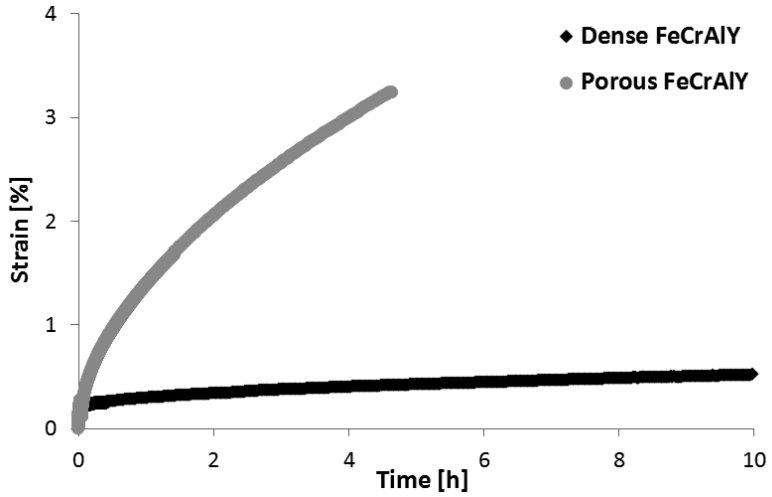

Figure 5–38: Creep curves of dense and porous FeCrAlY alloy for 30 MPa at 700 °C.

Due to continuous densification, analysis of data for porous material with conventional approaches would lead to misleading results. The creep results of the dense material are given in Figure 5-39.

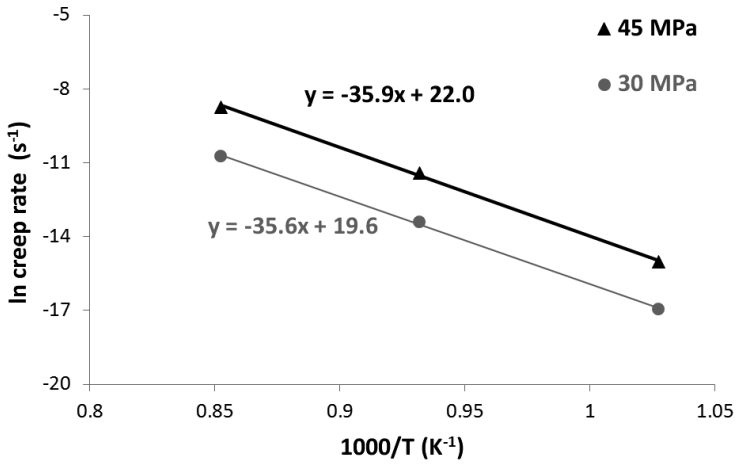

Figure 5–39: Creep rates of dense FeCrAlY specimens as a function of the inverse temperature. A linear fit was used for the analysis and the slope indicates the activation energy.

The average activation energy, pre-exponential factor and stress exponent of the dense FeCrAlY alloy material were 297 kJ/mol, (25 ± 2) 1/(MPa$^{4.872}$ s), and 4.87 ± 0.08, respectively. The stress exponent of 4.9 indicates dislocation creep. These data are roughly similar to that reported by Schweda [84]. He determined 486 kJ/mol and 5.29 as an average activation energy and stress exponent of the FeCr alloy, respectively.

6 DISCUSSION

The materials selected within the framework of the NASA-OTM project were investigated with respect to their mechanical behavior under several loading conditions. Ceramic materials have relatively low strength in tensile loading, whereas metallic materials are often more ductile and therefore might have higher tensile strength, at least at moderate temperature. However, strong creep deformation might be a major disadvantage of metallic materials compared to ceramics. These aspects are discussed in the following sections.

6.1 Correlation of microstructure and mechanical properties

For all materials grain size and porosity were characterized, since grain size influences creep deformation [103] and porosity needs to be taken into account to permit a comparison of dense and porous materials.

High substrate porosity is advantageous for membrane applications since it can enhance the gas flux to the functional layer and was proved in the case of CGO to increase the fracture strain (see section 5.2.3). However, besides the fact that porosities lead to lower stress at a given strain due to lower elastic modulus, a higher porosity is associated with a lower strength (see section 5.2.3).

Porosities and grain sizes for the nominally dense materials are compiled in Table 6-1. CGO batch 11 was used for comparison with dense BSCF and LSCF since it had the lowest porosity of all tested CGO batches.

Table 6-1: Porosity and grain size of the tested materials.

	BSCF	*LSCF*	*FeCrAlY*	*CGO 11*
Average porosity [%]	*9*	*4*	*1*	*12*
Average grain size [µm]	*10*	*1*	*16*	*1*

Elastic moduli of BSCF, LSCF and CGO were determined by ring-on-ring bending tests, whereas for FeCrAlY alloy three-point bending and indentation tests were used for porous and dense material, respectively. All tests were carried out in laboratory air. Since the elastic

modulus depends on porosity, properties at RT were linearly extrapolated to zero porosity, i.e. based on the experimental results for CGO (see section 5.2.3), where the mechanical properties revealed a rather linear dependency on porosity.

The calculation for BSCF was based on experimentally determined mechanical properties of specimens with 8.7 % and 34 % porosities. For LSCF material the experimental results for specimens with 4 % porosity were considered as well as data by M. Lipinska-Chwalek [[164]] who investigated $La_{0.6}Sr_{0.4}Co_{0.2}Fe_{0.8}O_{3-\delta}$ material with a porosity of ~ 46 %. The analysis for the FeCrAlY alloy considered data for porosities of 1 % and 35 %. Calculated elastic moduli are compiled in Table 6-2 and also given in Figure 6-1 for better visual comparison.

Table 6-2: Comparison of calculated (predicted) elastic moduli for 0 % porosity.

	BSCF		*LSCF*		*FeCrAlY*		*CGO*
Specimen´s porosity [%]	*8.7*	*34*	*4.1*	*46*	*35*	*1*	*12*
Corresponding elastic moduli [GPa]	*52*	*35*	*45*	*16 [[164]]*	*107*	*164*	*149*
Extrapolated value for 0 % porosity [GPa]	***58***		***48***		***166***		***192***

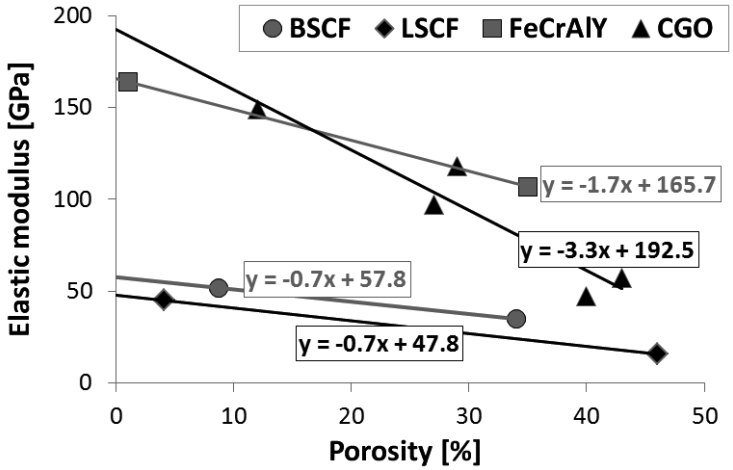

Figure 6–1: Extrapolations of elastic moduli to 0 % porosity for the selected materials.

FeCrAlY alloy and CGO yield significantly higher elastic moduli for dense material compared to BSCF and LSCF. However, high elastic modulus does not need to be in general an advantage since it leads to high stresses if identical strains are applied.

The elastic modulus of FeCrAlY alloy and CGO batch 9 were determined as a function of temperature (see sections 5.2.3 and 5.2.4). Normalized values were compared to literature data, for BSCF and LSCF. Figure 6-2 shows that the value for BSCF at 800 °C is slightly lower than at RT. The decrease and increase of the elastic moduli with temperature is assigned to spin transition effects [78]. LSCF showed a higher elastic modulus at 800 °C than at RT, which is assigned to the phase change [45]. The elastic modulus of CGO remained rather constant up to 800 °C. As expected, the elastic modulus of the FeCrAlY alloy significantly decreased with temperature down to 25 % of the RT value at 600 °C.

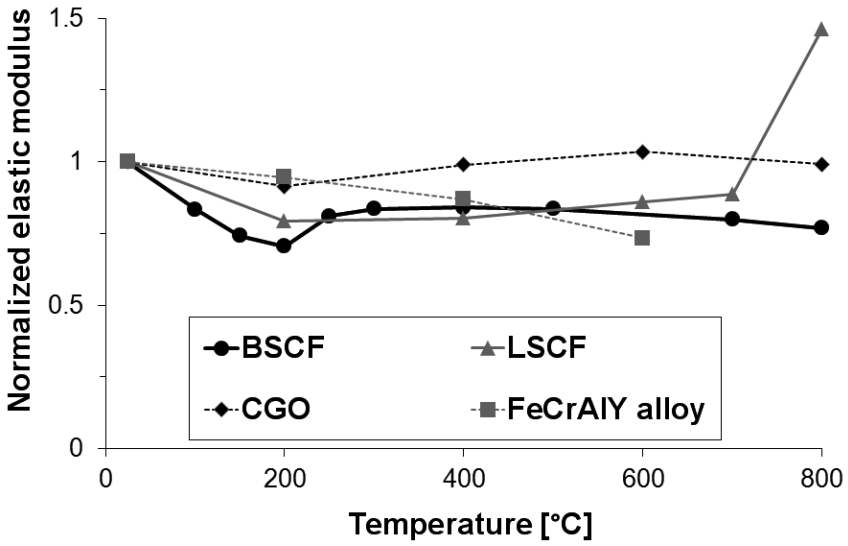

Figure 6–2: Elastic modulus normalized to the RT value of each material as a function of temperature for BSCF [78], LSCF [45], FeCrAlY alloy and CGO batch 9. The lines are a guide to the eye.

Fracture tests were carried out in laboratory air at all ceramic materials. For simplification, only results obtained using the maximum likelihood estimation (MLE) were compared according to ASTM C1239-07. Although not given in detail, in addition to MLE, all tests were also evaluated

using linear regression. Values of the characteristic fracture strength and failure strain were similar for both methods (within 5 %), whereas Weibull moduli showed a 15 % difference without any general trend.

Since the data are compared as design and engineering parameters, they were not extrapolated to zero porosity. Characteristic fracture strength and strain values with their Weibull moduli are compared in Table 6-3. For CGO, batches 7 and 11 are shown since they have the most similar porosity compared to BSCF and LSCF. The results obtained for other CGO batches are given in section 5.2.3. In both cases, for low and high porosities, CGO has slightly higher fracture strengths than BSCF and LSCF, similar as observed for the elastic moduli. However, CGO exhibits a rather low Weibull modulus and low fracture strains. The discussion which mechanical property is more important follows in section 6.4.1.

Table 6-3: Fracture properties obtained in tests with a loading rate of 100 N/min at room temperature.

	BSCF		*LSCF*	*CGO*	
	dense	*porous*		*Batch 7*	*Batch 11*
Porosity [%]	*8.7*	*34*	*4*	*12*	*40*
Characteristic fracture strength [MPa]	*86*	*31*	*73*	*92*	*46*
Unbiased Weibull modulus for strength	*7*	*8*	*11*	*4*	*6*
Characteristic fracture strain [%]	*0.17*	*0.09*	*0.22*	*0.06*	*0.10*
Unbiased Weibull modulus for strain	*8*	*6*	*10*	*4*	*9*

The fracture strength data as a function of temperature for BSCF [78] and LSCF [45] showed the same tendency as the elastic modulus (Figure 6-3). The CGO data revealed a slight deviation at 200 °C and 400 °C from the otherwise rather constant value. According to Schweda [84], the fracture stress of FeCr alloy strongly decreases with temperature above 400 °C. Compared with the RT value, the fracture stress at 800 °C is reduced by more than 90 %.

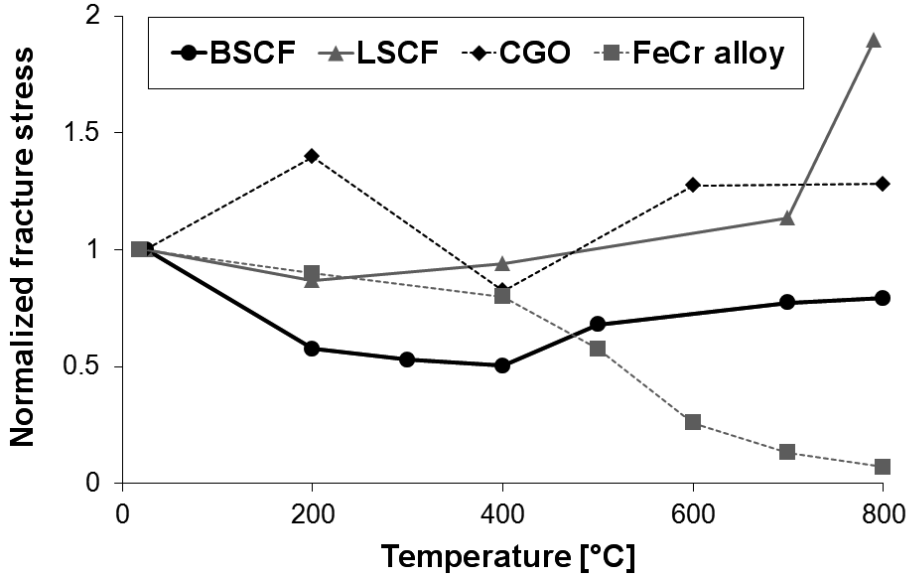

Figure 6–3: Normalized fracture stresses as a function of temperature for BSCF [78], LSCF [45], FeCr alloy [84] and CGO batch 9. The lines are a guide to the eye.

6.2 Subcritical crack growth and strength – probability – time diagram

BSCF, LSCF and CGO batch 9 were investigated with respect to subcritical crack growth. Detailed description is given in sections 5.2.1, 5.2.2 and 5.2.3. Here a comparison of the behavior of the different materials is given. The results are compiled in Figure 6-4.

According to the experimental results and the subsequent calculations of SCG parameters, BSCF and LSCF are rather insensitive to SCG, whereas CGO shows significant crack growth at subcritical stress levels in laboratory air. Investigations at dense and porous BSCF permit to assess the effect of porosity on SCG. The dense materials are more affected by SCG than the porous ones which might be correlated to pores that blunt the crack tip. In particular, BSCF with 9 % porosity shows approximately two times faster SCG than BSCF with 34 % porosity (~ two times higher *n* parameter).

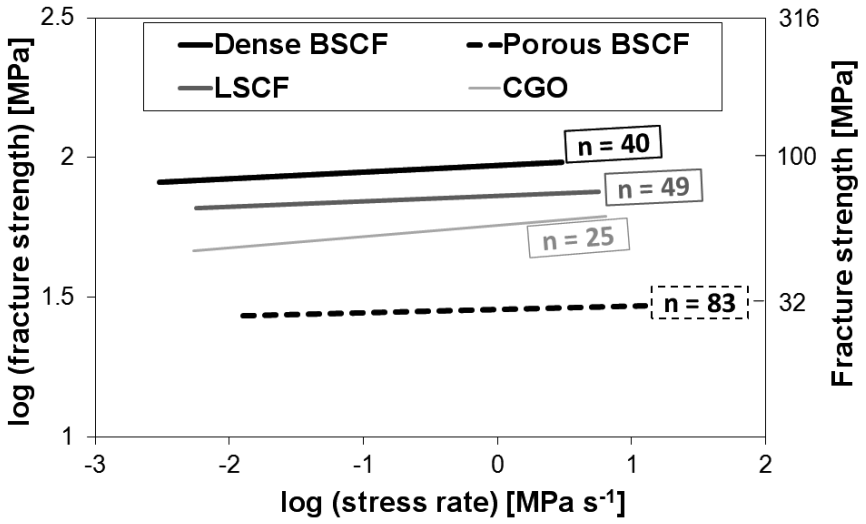

Figure 6–4: Fracture strength as a function of loading rate indicating the subcritical crack growth sensitivity at RT in air (n parameter).

The relationship between strength, probability and time was used for lifetime prediction of BSCF, LSCF, and CGO. For comparison, a calculated lifetime of 40 years at 1 % failure probability was chosen (Figure 6-5).

Although dense BSCF has higher fracture strength at room temperature, LSCF can withstand higher stresses in the long term operation for 40 years due to its lower subcritical crack growth sensitivity. In particular, for a 1 % failure probability, dense BSCF and LSCF should not be constantly loaded by stresses higher than ~ 29 MPa and ~ 35 MPa, respectively. This implies that the substrate stress induced by, for example, differences in thermal expansion to the sealant materials, should not exceed this value.

In case of porous material, the tolerable stresses become significantly lower. For porous BSCF, the stress should not exceed 9 MPa. Due to the higher porosity (43 %) in combination with lower Weibull modulus and higher sensitivity to SCG, CGO yielded the lowest tolerable stress. For a 1 % failure probability, this CGO variant should not be exposed to constant stresses of more than 8 MPa in order to withstand the 40 years lifetime.

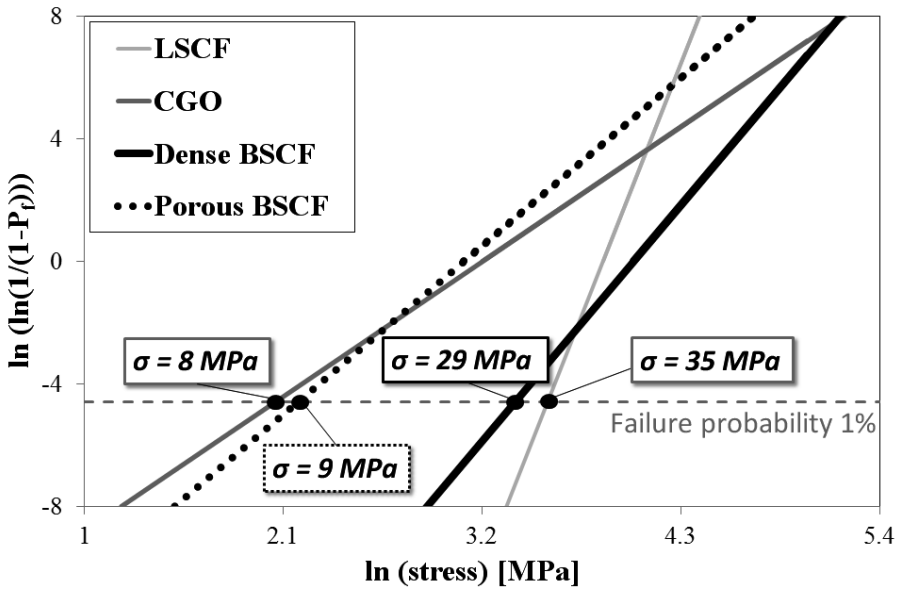

Figure 6–5: Strength-probability-time diagram for a 40 years lifetime.

6.3 Creep deformation and rupture

The results of compressive creep tests on FeCrAlY alloy are compared with literature values of BSCF and LSCF in Figure 6-6. The tests were carried out with a load of 30 MPa, which is considered to be representative for application in a membrane system [[113]]. CGO creep data were not found in the literature and this material could not be creep tested in the present work since specimens were not available in suitable geometry.

The dashed line represents a tolerable strain rate of 1 % per year [[112]]. Considering this limit, BSCF shows higher creep deformation than tolerable at temperatures from 700 °C to 950 °C. Besides the similar creep rate at 850 °C, LSCF shows higher creep resistance than BSCF. In particular, LSCF shows tolerable creep rates at 800 °C and below. As might be expected, the tests performed at FeCrAlY alloy yielded larger creep deformations than the ceramics. At 700 °C, 800 °C and 900 °C significantly higher creep rates occur than the tolerable 1 % per year. However, creep can also aid the relaxation of stresses induced by differences in thermal expansion and a detailed consideration of creep and thermal mismatch effects on the actual design requires detailed finite element simulations.

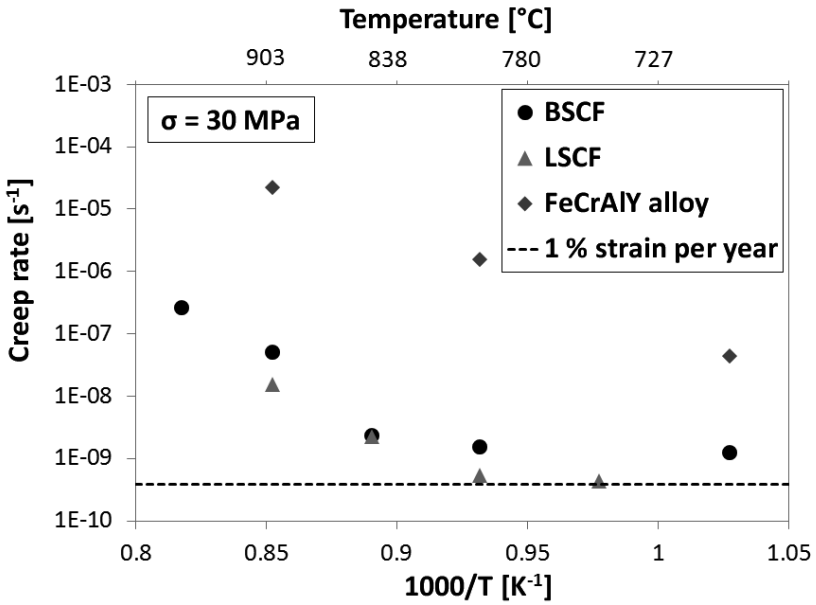

Figure 6–6: Creep rates of BSCF [[110]], LSCF [[111]] and FeCrAlY alloy.

Due to experimental limitations creep rupture tests were restricted to BSCF. A number of creep rupture tests were carried out for dense BSCF at application relevant temperatures, i.e. 850 °C and 900 °C. As expected, time to creep failure decreased with temperature and applied nominal stress (Figure 6-7). Moreover, an increase in temperature from 850 °C to 900 °C decreased the time to failure by a factor of ~ 5 – 10.

For comparative purposes, only one test up to rupture was performed for LCSF. Under the same applied stress, the LSCF specimen showed an around 20 times longer lifetime compared to BSCF. Reasons for the longer lifetime of LSCF compared to BSCF under these conditions can be the lower creep rate of LSCF compared to BSCF [[110]]. The smaller grain size of LSCF (~ 1 μm) compared to BSCF (~ 10 μm) can be ruled out as an additional factor since creep rupture time should increase with grain size [[165]].

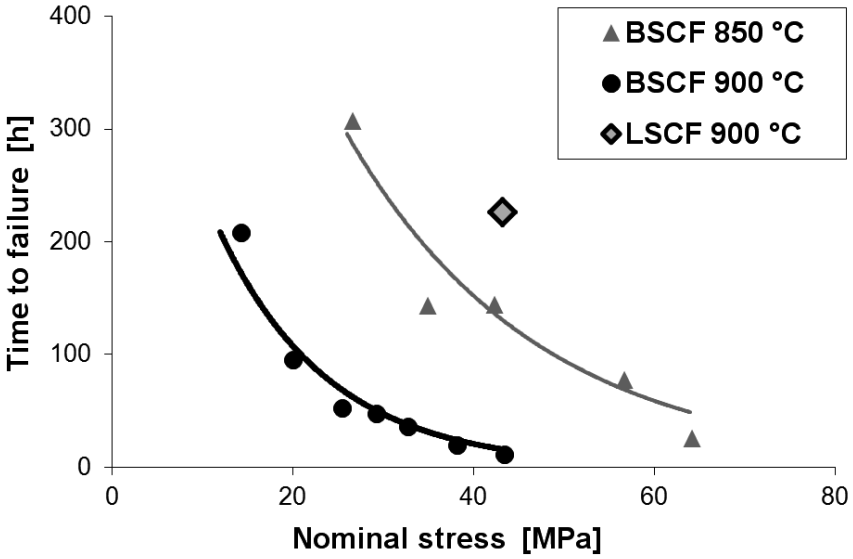

Figure 6–7: Time to rupture in bending creep. The curves are a guide to the eye.

6.4 Simulations

The experimental investigations described so far were mainly performed on substrates. The membrane assembly consists of a dense layer on a porous substrate. In the subsequent sections the influence of material properties, geometrical arrangement and orientation with respect to the oxygen partial pressure gradient on the stress state in a layered membrane composite will be discussed. Critical selection criteria for porous substrate will be given, and, finally, the probability of membrane layer failure during operation will be discussed.

6.4.1 Influence of mechanical properties on stress/strain induced failure

As pointed out in section 4.3.1, the aim of this investigation was to determine which mechanical properties can be used for a reliability assessment of layered membrane structures. Accordingly, finite element simulation of thermo-mechanical loads was performed for a model system based on different porous CGO batches. The structural design was symmetrical (see Figure 4-10), with a dense layer between two porous supports of identical thickness. The elastic modulus of the dense membrane layer was assumed according to [148] and used in all simulations, whereas

mechanical properties (elastic modulus, fracture strength and strain) of porous substrate were applied for each particular CGO batch. Table 6-4 compiles the results obtained by stress simulations for material variations corresponding to the data of all CGO batches. Grey boxes indicate the characteristic parameters calculated as stress to fracture strength ratio and strain to fracture strain ratio. The stresses were taken from the central part of the FEM-model. Due to a vertical constraint (see Figure 4-10), the stresses of a particular substrate were constant at that position through the thickness. Bold numbers indicate the optimal batch which showed the lowest stress/strain ratio compared to its fracture strength/strain ratio.

Table 6-4: Data to select the optimal CGO batch.

Batch number	1	2	3	4	**5**	6	7	8	9	10	11
Elastic modulus [GPa]	90	114	118	38	**36**	/	47	97	57	118	149
Fracture strength [MPa]	57	75	58	41	**40**	/	46	80	55	89	92
Fracture strain [%]	0.07	0.06	0.05	0.10	**0.11**	/	0.10	0.08	0.09	0.08	0.06
Stress ratio	1.6	1.5	2.0	0.9	**0.9**	/	1.0	1.2	1.0	1.3	1.6
Strain ratio	1.5	1.6	1.9	1.0	**0.9**	/	1.0	1.3	1.1	1.3	1.6

Although there were several batches with similar critical strain, FEM analysis revealed that the CGO batch 5 has the optimal mechanical properties to avoid failure. Obviously its low stiffness led to low stresses. It is observed very often that the elastic modulus and strength scale with porosity [166,167]. In such cases one would suggest that the optimum material will be the one with the lowest elastic modulus. Although it exhibits lowest induced stresses, the material with the lowest elastic modulus can become unsuitable if its strength is too low. Note that the simulation carried out above only considered the effect of chemical strains. Nevertheless, the effect of

thermal mismatch strains in systems with different substrate and membrane materials would be similar.

6.4.2 Parameters which influence the stress state of membrane structure

The stress state in the membrane assembly is not only determined by the properties of membrane layer and substrate, but also by the geometrical arrangement. Hence, the effect of different geometries, tubular and planar, had to be assessed in order to minimize the mechanical loading of the materials. Since not all parameters have the same impact on stress state, it was necessary to determine the crucial parameters. Numerical simulation appeared to be more suitable for this purpose than experimental testing due to the large number of parameters. Details on input data for simulation can be found in section 4.3.2.

The first analysis step considered the influence of TEC mismatch. The resulting in-plane stresses induced by an assumed TEC difference (substrate minus membrane) of $-2 \cdot 10^{-6}$ K^{-1} are given in Table 6-5. An illustration of stress distribution for the planar case is displayed in Figure 6-8.

Table 6-5: Stresses caused by the TEC mismatch of substrate and membrane layer.

Position	Stress- planar case	Stress- tubular case	Difference
Membrane	380 MPa	420 MPa	10 %
Substrate at interface	-15 MPa	-4 MPa	380 %
Free substrate surface	8 MPa	-4 MPa	75 %

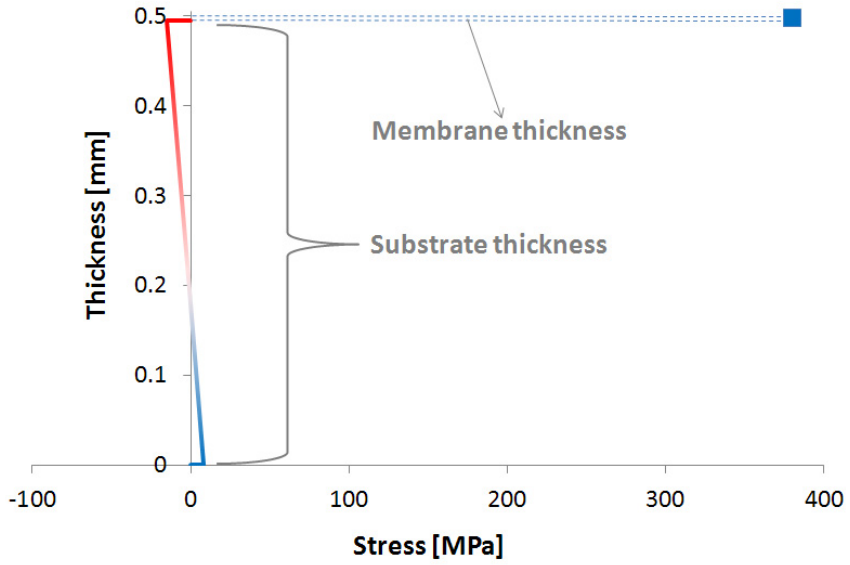

Figure 6–8: Stress distribution over membrane thickness for the planar case revealing significantly higher stresses in membrane layer compared to the substrate. The interface is at the position 0.495 mm.

The tubular assembly yielded lower absolute values of the substrate stress. Furthermore, as brittle materials are more stable in compression than in tension, the tubular case is again favorable for substrate stability. The membrane layer is loaded with very high stress in both cases. Further analysis of membrane failure based on fracture energy is given in section 6.4.4. If TEC mismatch is $+2 \cdot 10^{-6}$ K^{-1}, the sign of the values presented in Table 6-5 will change but the absolute values will remain unchanged.

Table 6-6 presents the effect of the substrate elastic modulus. The investigation was carried out for the planar and tubular case in which the elastic modulus was varied from 35 GPa to 75 GPa.

*Table 6-6 a): Influence of the substrate elastic modulus in the **planar** case.*

Position	E_S **= 35 GPa**	E_S **= 75 GPa**	**Difference**
Membrane	350 MPa	390 MPa	10 %
Substrate at interface	-14 MPa	-16 MPa	10 %
Free substrate surface	7 MPa	8 MPa	10 %

*Table 6-6 b): Influence of the substrate elastic modulus in the **tubular** case.*

Position	E_S **= 35 GPa**	E_S **= 75 GPa**	**Difference**
Membrane	410 MPa	420 MPa	3 %
Substrate at interface	-4 MPa	-4 MPa	3 %
Free substrate surface	-4 MPa	-4 MPa	3 %

In all cases, the membrane layer showed high stresses, slightly higher in tubular case. However, the planar case appeared to be less favorable for the substrate. The stresses were always low at the free substrate surface.

A similar analysis was carried out for the influence of elastic modulus of the membrane layer. The results showed the same tendency in planar and tubular cases as in the calculations where the substrate elastic modulus was varied. Although the variation range was smaller, from 180 GPa to 220 GPa, the elastic modulus of the membrane had much stronger impact than the elastic modulus of the substrate (Table 6-7).

*Table 6-7 a): Influence of the coating elastic modulus in the **planar** case.*

Position	**E_C = 180 GPa**	**E_C = 220 GPa**	**Difference**
Membrane	340 MPa	410 MPa	20 %
Substrate at interface	-14 MPa	-16 MPa	20 %
Free substrate surface	7 MPa	8 MPa	20 %

*Table 6-7 b): Influence of the coating elastic modulus in the **tubular** case.*

Position	**E_C = 180 GPa**	**E_C = 220 GPa**	**Difference**
Membrane	380 MPa	460 MPa	22 %
Substrate at interface	-4 MPa	-4 MPa	22 %
Free substrate surface	-4 MPa	-5 MPa	21 %

The thicknesses of substrate and membrane are other important parameters that were analyzed. In Table 6-8 values are given for extreme cases where the thickness ratio (membrane divided by substrate thickness) ranges from 0.0025 to 0.1. The elastic moduli of substrate and membrane layer were set to 55 GPa and 200 GPa, respectively.

*Table 6-8 a): Influence of the thickness ratio in the **planar** case.*

Position	**t_C / t_S = 0.0025**	**t_C / t_S = 0.1**	**Factor**
Membrane	420 MPa	160 MPa	2.6
Substrate at interface	-4 MPa	-70 MPa	17
Free substrate surface	2 MPa	49 MPa	18

*Table 6-8 b): Influence of the thickness ratio in the **tubular** case.*

Position	t_C / t_S **= 0.0025**	t_C / t_S **= 0.1**	**Factor**
Membrane	430 MPa	320 MPa	1.3
Substrate at interface	-1 MPa	-31 MPa	34
Free substrate surface	-1 MPa	-30 MPa	28

As expected, a thicker substrate increased the membrane stresses and decreased the substrate stresses. For the higher thickness ratio, the planar case appears to be more favorable for the membrane, whereas the tubular case results in lower and only compressive substrate stresses. With changing the sign of the TEC mismatch the stresses again change from compressive to tensile.

As shown by these FEM studies, difference in TEC between substrate and membrane plays an important role. Therefore, when choosing a certain combination of materials for membrane assembly, special attention has to be directed towards the minimization of TEC mismatch. The elastic modulus of the substrate material has relatively small influence on the resulting residual stresses due to the very high substrate/membrane thickness ratio. Contrary to the substrate, varying the elastic modulus of the membrane significantly changes the stress state. With increasing thickness, the substrate exhibits lower stresses. The difference between planar and tubular case with respect to the considered positions is illustrated in Figure 6-9.

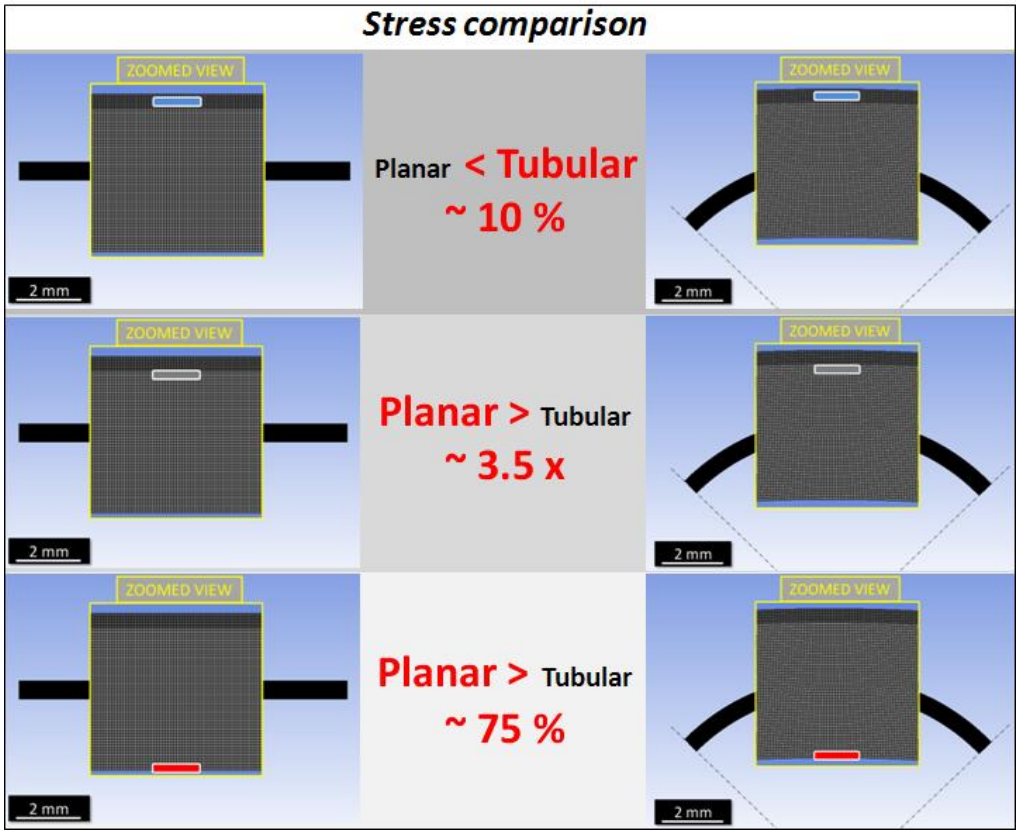

Figure 6–9: Stress difference of planar and tubular design case. Colored boxes represent the observed positions.

The membrane layer will generally be exposed to very high stresses, which are even slightly higher in tubular case. However, the planar configuration seems to be less favorable for the substrate, since higher tensile stresses appear. In all cases the free surface of the substrate showed low stresses and thus is not a critical position. The difference between the planar and tubular case is most pronounced for the substrate, however, at small absolute stress levels (less than 10 MPa).

6.4.3 Optimal membrane design

Three different membrane geometries were analyzed in order to find an optimal design with respect to stress induced in the substrate. The analyzed geometries were one symmetric assembly, one asymmetric with the substrate on the oxidized and one with the substrate on the reduced side (see Figure 4-10 and Figure 4-15). The simulation was based on CGO material properties. The mechanical properties of dense membrane layer were taken as described in section 4.3.1, whereas the mechanical properties of the favorable batch 5 were used as input data of the porous substrate (see section 6.4.1). Table 6-9 summarizes the obtained stress results.

Table 6-9: Comparison of different membrane arrangements.

Design	*Substrate stress [MPa]*	*Substrate strain [%]*	*Membrane stress gradient [MPa]*
Symmetric membrane assembly	*36*	*0.100*	*± 180*
Asymmetric, substrate on oxidized (feed side)	*12*	*0.033*	*60 / -300*
Asymmetric, substrate on reduced (sweep side)	***-12***	***-0.033***	*- 60 / 300*

By exchanging feed and sweep side, different stress and strain distributions were obtained. Effects of the gas flow in pores were not taken into consideration. It can be concluded that, from the mechanical point of view, the most favorable design for the porous substrate is an asymmetric membrane assembly with the porous substrate placed on the sweep side since the substrate in this case exhibits rather low compressive stresses. In all cases, the membrane layer exhibited significantly higher stresses than the substrate. Stress distribution and possible failure of the membrane layer is discussed in the next chapter since the aim of this section was the analysis of optimal design for the substrate based on the arbitrarily applied load described in section 4.3.1.

6.4.4 Membrane layer failure - fracture energy criterion

To assess the risk of membrane layer failure, numerical simulations of fracture energy were carried out. Due to limitations in the available input data, the analyses were performed for two cases, a CGO layer on a CGO substrate, and a BSCF layer on a BSCF substrate. The asymmetric membrane structure was used in the analysis since it showed optimal stress distribution. Input data for simulation are given in section 4.3.4.

In case of a CGO layer on a CGO substrate, the fracture energy was calculated to be 2.5 J/m^2 based on the Equation (3.11). The FEM analysis showed that in this loading situation the membrane exhibits high tensile stresses due to chemical expansion of the substrate. The stress distribution over the membrane system is shown in Figure 6-10. Hence, the membrane might fail by surface cracking. For that case, the non-dimensional Z constant from Equation (3.13) was taken as 0.25 (according to [99]) in order to calculate the energy release rate.

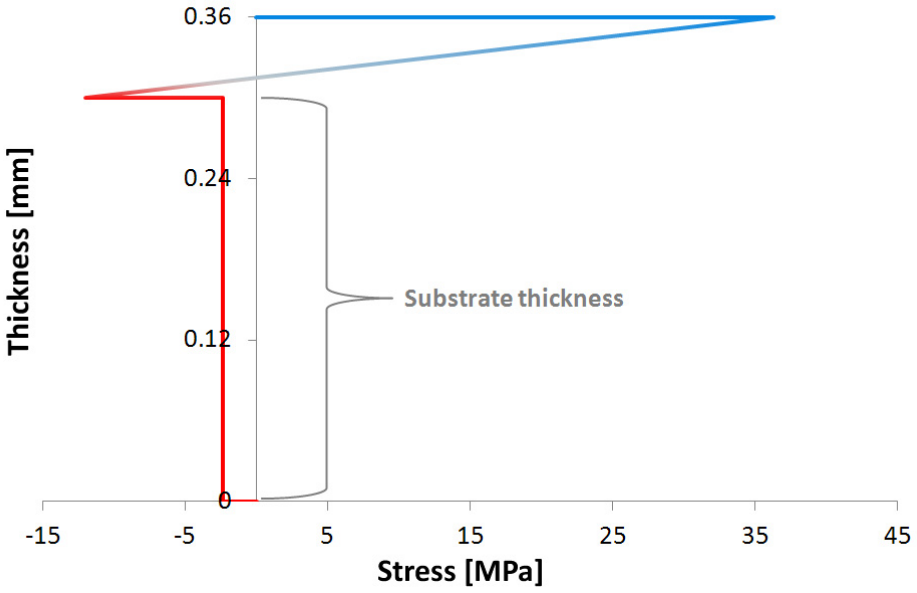

Figure 6–10: Calculated stress distribution across the membrane assembly.

However, since the applied chemical strain causes too low stresses even to reach the fracture strength of CGO, it is expected that the CGO membrane will survive under these conditions. Another positive circumstance is that even if the stresses would be higher than the fracture strength, the membrane would not fail since there would not be enough energy for crack propagation. Results comparing energy release rate (available energy) and fracture energy, as well as residual stresses and fracture strength, as a function of membrane thickness are depicted in Figure 6-11.

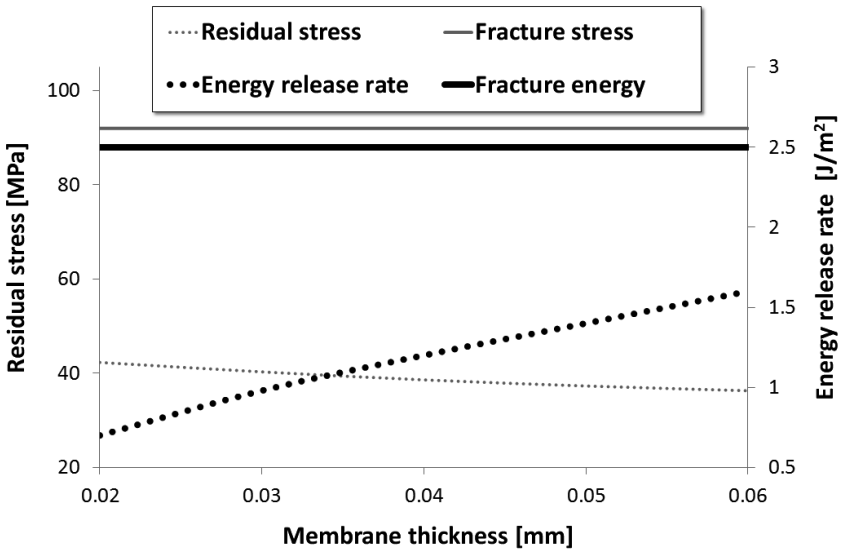

Figure 6–11: Energy release rate and residual stresses as a function of membrane thickness for CGO (asymmetric design, membrane on feed side).

Investigations were also carried out for a dense BSCF membrane on a porous (34 %) BSCF substrate. According to Equation (3.11), for plane strain condition, the fracture energy of dense BSCF was calculated to be 15 J/m^2. Similar as in the case of CGO, the membrane exhibited high tensile stresses, and therefore had a risk of fracture by surface cracking. Hence, the non-dimensional Z constant from the Equation (3.13) was taken as 0.25 (according to [99]) to calculate the energy release rate. The results are depicted graphically in Figure 6-12. The energy release rate did not exceed the fracture energy and in addition the residual stress was lower than

the fracture strength of dense material. Hence, both criteria imply that stable operation is possible from a mechanical point of view.

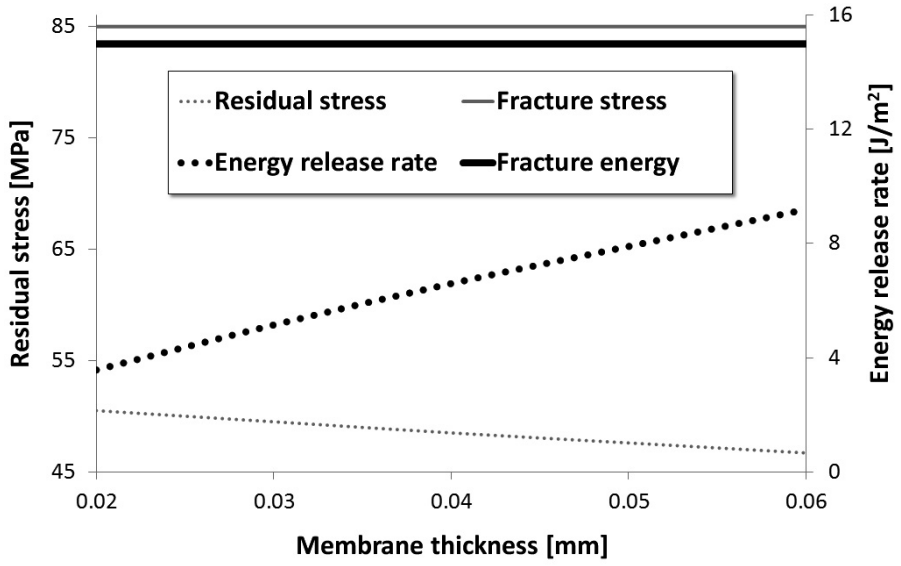

Figure 6–12: Energy release rate and residual stresses as a function of membrane thickness for BSCF (asymmetric design, membrane on feed side).

7 CONCLUSIONS

Within the framework of the NASA-OTM project porous and dense BSCF, LSCF, CGO ceramics as well as a FeCrAlY alloy were selected as promising materials for oxygen transport membrane application. These materials were characterized with respect to their mechanical behavior and failure limits at room and operation relevant temperatures. Additional simulations have been carried out with respect to the interpretation of mechanical data for layered composites that permitted to assess different membrane design variants.

Elastic modulus and fracture strength of the investigated materials basically agreed with the data reported in literature for similar porous and dense materials. In particular, results for BSCF and LSCF agreed well with previous reports, data for CGO are novel in this respect, whereas the results for FeCrAlY alloy agree to previous reports. Overall, all materials appear to have advantages and disadvantages, and hence, there was no material that might be considered to be superior in any respect.

Compared to the other investigated ceramics, BSCF displayed intermediate elastic modulus, fracture strength and fracture strain at RT. The investigations carried out in the range of the expected operation temperature of around 800 °C revealed a slight decrease of these characteristic values compared to RT. Both, porous and dense BSCF appeared not to be very sensitive to subcritical crack growth. SPT analysis, which permits a lifetime prediction, revealed that dense BSCF might sustain static stress of 29 MPa for 40 years, with a failure probability of 1 %. In case of porous BSCF, the tolerable stress was 9 MPa for the same probability and lifetime. In fact, the ratio of these data is identical to the ratio of the measured fracture strengths at room temperature. BSCF appears to be prone to creep rupture already at 850 °C. Hence, in order to warrant safe operation for 40 years at elevated temperatures, an applied stress in the order of 1 MPa might be assumed as a limit. Creep rupture tests furthermore revealed that increasing the temperature from 850 °C to 900 °C reduces the lifetime for dense BSCF by almost a factor of 10.

Dense LSCF had similar mechanical characteristics (elastic modulus, fracture strength) as dense BSCF at RT. However, these characteristics increased at around 800 °C due to a well-known phase transition. Similar as BSCF, LSCF also has a low sensitivity to subcritical crack growth. Predictions based on the SPT diagram revealed that dense LSCF might tolerate static stress of 35

MPa for 40 years, with a failure probability of 1 %, which is similar to the load limit of BSCF. However, with respect to creep rupture, LSCF appeared to be superior, with similar values at 900 °C as BSCF at 850 °C.

Eleven different batches of porous CGO prepared using different sintering conditions were thoroughly investigated. The optimal batch seems to be the one with the highest fracture strain. This conclusion can be generalized to all materials because mechanical loading induced by chemical and thermal strain mismatch in the membrane assembly are mostly strain controlled. Microstructural and mechanical analysis results were given as a feedback to the material´s supplier (DTU Energy Conversion) and led to an improvement of materials production and subsequently higher reliability of the material. The porous CGO yielded rather similar elastic modulus and fracture strength at RT and at elevated temperatures. Although, compared to the other ceramics, CGO indicated higher sensitivity to subcritical crack growth, the allowable stress for a 40 years static load at room temperature conditions is comparable to the data obtained for porous BSCF. It should be noted that initial results indicated that this material is the least sensitive with respect to creep deformation and hence creep rupture.

FeCrAlY alloy showed the highest RT elastic modulus, which, however, strongly decreases with temperature. Its creep behavior is inferior to all investigated ceramic materials.

Simulation of bi-layered membrane structures revealed that the TEC mismatch of dense membrane layer and porous substrate strongly affects the stress state. The elastic modulus of the porous substrate has only a rather small influence on membrane stress. Contrary to the substrate, varying the elastic modulus of the dense membrane, significantly changes the stress state, in particular of the substrate material.

FEM analysis comparing symmetrical and asymmetrical structures revealed that the favorable set-up is the asymmetrical one, with the substrate on the sweep side since in this case the porous substrate exhibits the lowest and also compressive stresses which is more favorable for long term operation.

Simulations of a BSCF layer on a BSCF substrate, and a CGO layer on a CGO substrate, revealed that in both cases a membrane failure due to chemically induced strains should not be expected.

In case of a ring-on-ring test performed on the curved, bi-layered specimens, it was shown by finite element analysis that the linear elastic theory can still be used for the convex shaped specimens within the certain curvature limits.

8 REFERENCES

[1] V. Ramanathan, Y. Feng: Air pollution, greenhouse gases and climate change: Global and regional perspectives, Atmospheric Environment, Volume 43, Issue 1, 2009, p. 37-50

[2] *http://unfccc.int/kyoto_protocol/items/2830.php*

[3] J. Gibbins, H. Chalmers: Carbon capture and storage, Energy Policy, Volume 36, Issue 12, 2008, p. 4317-4322

[4] IPCC special report on Carbon Dioxide Capture and Storage, Cambridge University Press, 2005, ISBN 13 978-0-521-68551-1

[5] R. Thiruvenkatachari, S. Su, H. An, X. Xiang Yu: Post combustion CO_2 capture by carbon fibre monolithic adsorbents, Progress in Energy and Combustion Science, Volume 35, Issue 5, 2009, p. 438-455

[6] B.J.P. Buhre, L.K. Elliott, C.D. Sheng, R.P. Gupta, T.F. Wall: Oxy-fuel combustion technology for coal-fired power generation, Progress in Energy and Combustion Science, Volume 31, Issue 4, 2005, p. 283-307

[7] C. A. Scholes, K. H. Smith, S. E. Kentish, G. W. Stevens: CO_2 capture from pre-combustion processes—Strategies for membrane gas separation, International Journal of Greenhouse Gas Control, Volume 4, Issue 5, 2010, p. 739-755

[8] C.Y. Park, T.H. Lee, S.E. Dorris, U. Balachandran: Hydrogen production from fossil and renewable sources using an oxygen transport membrane, International Journal of Hydrogen Energy, Volume 35, Issue 9, 2010, p. 4103-4110

[9] *www.bellona.org*

[10] L.M van der Haar, H. Verweij: Homogeneous porous perovskite supports for thin dense oxygen separation membranes, Journal of Membrane Science, Volume 180, Issue 1, 2000, p. 147-155

[11] S. Baumann, J.M. Serra, M.P. Lobera, S. Escolástico, F. Schulze-Küppers, W.A. Meulenberg: Ultrahigh oxygen permeation flux through supported $Ba_{0.5}Sr_{0.5}Co_{0.8}Fe_{0.2}O_{3-\delta}$ membranes, Journal of Membrane Science, Volume 377, Issues 1–2, 2011, p. 198-205

[12] Z. Shao, W. Yang, Y. Cong, H. Dong, J. Tong, G. Xiong: Investigation of the permeation behavior and stability of a $Ba_{0.5}Sr_{0.5}Co_{0.8}Fe_{0.2}O_{3-\delta}$ oxygen membrane, Journal of Membrane Science, Volume 172, Issue 1-2, 2000, p. 177-188

[13] Y. Teraoka, Y. Honbe, J. Ishii, H. Furukawa, I. Moriguchi: Catalytic effects in oxygen permeation through mixed-conductive LSCF perovskite membranes, Solid State Ionics, Volumes 152–153, 2002, p. 681-687

[14] O. Büchler, J.M. Serra, W.A. Meulenberg, D. Sebold, H.P. Buchkremer: Preparation and properties of thin $La_{1-x}Sr_xCo_{1-y}Fe_yO_{3-\delta}$ perovskitic membranes supported on tailored ceramic substrates, Solid State Ionics, Volume 178, Issues 1–2, 2007, p. 91-99

[15] S. Diethelm, J. Van Herle, P.H. Middleton, D. Favrat: Oxygen permeation and stability of $La_{0.4}Ca_{0.6}Fe_{1-x}Co_xO_{3-\delta}$ (x = 0, 0.25, 0.5) membranes, Journal of Power Sources, Volume 118, Issues 1–2, 2003, p. 270–275

[16] J. Sunarso, S. Baumann, J.M. Serra, W.A. Meulenberg, S. Liu, Y.S. Lin, J.C. Diniz da Costa: Mixed Ionic-Electronic Conducting (MIEC) ceramic-based membranes for oxygen separation, Journal of Membrane Science, 2008, Volume 320, Issues 1–2, p. 13-41

[17] A. Neumann, N.H. Menzler, I. Vinke, H. Lippert: Systematic study of chromium poisoning of LSM cathodes – single cell tests, Ecs Transactions, Volume 25, No. 2, 2009, p. 2889-2898

[18] H. Wang, C. Tablet, A. Feldhoff, J. Caro: Investigation of phase structure, sintering, and permeability of perovskite-type $Ba_{0.5}Sr_{0.5}Co_{0.8}Fe_{0.2}O_{3-\delta}$ membranes, Journal of Membrane Science, Volume 262, Issues 1–2, 2005, p. 20–26

[19] H.J.M. Bouwmeester: Dense ceramic membranes for methane conversion, 5th International Conference on Catalysis in Membrane Reactors, Catalysis Today, Volume 82, Issues 1–4, 2003, p. 141–150,

[20] L. Katz, R. Ward: Structure relations in mixed metal oxides, Inorg. Chem., 3(2), 1964, p. 205-211.

[21] W. D. Kingery, H. K. Bowen, D. R. Uhlmann, Introduction to Ceramics, John Wiley & Sons, 1976

[22] V.M. Goldschmidt, Akad. Oslo., A42, 1946, 224.

[23] C. Li, K. Chi, K. Soh, P. Wu: Formability of ABO_3 perovskites, Journal of Alloys and Compounds, Volume 372, 2004, p. 40-48.

[24] S. Stølen, E. Bakken, C.E. Mohn: Oxygen-deficient perovskites: linking structure, energetics and ion transport, Phys. Chem. Chem. Phys., Volume 8, Issue 4, 2006, p. 429-447

[25] Y. Teraoka, H. Zhang, N. Yamazone: Oxygen-sorptive properties of defect perovskite-type $La_{1-x}Sr_xCo_{1-y}FeyO_{3-\delta}$, Chem Lett., 1985, p. 1367- 1370

[26] Y. Teraoka, H. Zhang, S. Furukawa, N. Yamazone: Oxygen-permeation through perovskite-type oxide. Chem Lett., 1985, p. 1743-1746

[27] Y. Teraoka, H.M. Zhang, K. Okamoto, N. Yamazone: Mixed ionic-electronic conductivity of $La_{1-x}Sr_xCo_{1-y}FeyO_{3-\delta}$, Mater Res Bull., 1988, Volume 23, p. 51-58

[28] W. Zhou, R. Ran, Z. Shao: Progress in understanding and development of $Ba_{0.5}Sr_{0.5}Co_{0.8}Fe_{0.2}O_{3-\delta}$ based cathodes for intermediate-temperature solid-oxide fuel cells: A review, Journal of Power Sources, Volume 192, Issue 2, 2009, p. 231–246

[29] H. Yokokawa, N. Sakai, T. Kawada, M. Dokiya: Thermodynamic stabilities of perovskite oxides for electrodes and other electrochemical materials, Solid State Ionics, Volume 52, 1992, p. 43-56

[30] Z.P. Shao, G.X. Xiong, J.H. Tong, H. Dong,W.S. Yang: Ba effect in doped $Sr(Co_{0.8}Fe_{0.2})O_{3-\delta}$ on the phase structure and oxygen permeation properties of the dense ceramic membranes, Sep. Purif. Tech. 25, 2001, p. 419-429

[31] J.F. Vente, S. McIntosh, W.G. Haije, H.J.M. Bouwmeester, Properties and performance of $Ba_xSr_{1-x}Co_{0.8}Fe_{0.2}O_{3-\delta}$ materials for oxygen transport membranes, Journal of Solid State Electrochemistry 10, 2006, p. 581-588

[32] C. Niedrig, S.Taufall, M. Burriel, W. Menesklou, S. F. Wagner, S. Baumann, E. Ivers-Tiffée, Solid State Ionics, Volume 197, 2011, p. 25-31

[33] S. Svarcova, K. Wiik, J. Tolchard, H.J.M. Bouwmeester, T. Grande: Structural instability of cubic perovskite $Ba_xSr_{1-x}Co_{1-y}Fe_yO_{3-\delta}$, Solid State Ionics 178, 2008, p. 1787-1791

[34] M. Schulz, R. Kriegel, A. Kämpfer: Assessment of CO_2 stability and oxygen flux of oxygen permeable membranes, Journal of Membrane Science 378, 2011, p. 10–17

[35] S. Engels, T. Markus, M. Modigell, L. Singheiser: Oxygen permeation and stability investigations on MIEC membrane materials under operating conditions for Power-Plant-Processes, Journal of Membrane Science, Volume 370, 2011, p. 58-69

[36] M. Arnold, H.H. Wang, A. Feldhoff: Influence of CO_2 on the oxygen permeation performance and the microstructure of perovskite-type $(Ba_{0.5}Sr_{0.5})(Co_{0.8}Fe_{0.2})O_{3-\delta}$ membranes. Journal of Membrane Science 293, 2007, p. 44-52

[37] A.Y. Yan, M. Yang, Z.F. Hou, Y.L. Dong, M.J. Cheng: Investigation of $Ba_{1-x}Sr_xCo_{0.8}Fe_{0.2}O_{3-\delta}$ as cathodes for low-temperature solid oxide fuel cells both in the absence and presence of CO_2, Journal of Power Sources 185, 2008, p. 76-84

[38] J. Mizusaki, Y. Mima, S. Yamauchi, K. Fueki: Nonstoichiometry of the perovskite-type oxides $La_{1-x}Sr_xCoO_{3-\delta}$, Journal of Solid State Chemistry, Volume 80, 1989, p. 102-111

[39] A. Petric, P. Huang, F. Tietz: Evaluation of La-Sr-Co-Fe-O perovskites for solid oxide fuel cells and gas separation membranes, Solid State Ionics, Volume 135, 2000, p. 719-725.

[40] A. Mineshige, J. Izutsu, M. Nakamura, K. Nigaki, J. Abe, M. Kobune, S. Fujii, T. Yazawa: Introduction of A-site deficiency into $La_{0.6}Sr_{0.4}Co_{0.2}Fe_{0.8}O_{3-\delta}$ and its effect on structure and conductivity, Solid State Ionics, Volume 176, 2005, p. 1145-1149

[41] C.Y. Tsai, A.G. Dixon, H.M. Yi, W.R. Moser, M.R. Pascucci: Dense perovskite, $La_{1-x}A'_xFe_{1-y}Co_yO_{3-\delta}$ (A'=Ba, Sr, Ca), membrane synthesis, applications, and characterization, J. Am. Ceram. Soc., Volume 81, 1998, p. 1437-1444

[42] J.W. Stevenson, T.R. Armstrong, R.D. Carneim, L.R. Pederson, W.J. Weber: Electrochemical properties of mixed conducting perovskites $La_{1-x}M_xCo_{1-y}Fe_yO_{3-\delta}$ (M=Sr, Ba, Ca), J. Electrochem. Soc., vol. 143, 1996, p. 2722-2729

[43] J.A. Lane, S.J. Benson, D. Waller, J.A. Kilner "Oxygen transport in $La_{0.6}Sr_{0.4}Co_{0.2}Fe_{0.8}$", Solid State Ionics, Volume 121, 1999, p. 201-208

[44] J.H. Park, S.D. Park: Oxygen permeability and structural stability of $La_{0.6}Sr_{0.4}Co_{0.2}Fe_{0.8}O_{3-\delta}$ membrane, Korean J. Chem. Eng., Volume 24, 2007, p. 897-905

[45] B.X. Huang, J. Malzbender, R.W. Steinbrech, E. Wessel, H.J. Penkalla, L. Singheiser: Mechanical aspects of ferro-elastic behavior and phase composition of $La_{0.58}Sr_{0.4}Co_{0.2}Fe_{0.8}O_{3-\delta}$, Journal of Membrane Science, Volume 349, Issues 1–2, 2010, p. 183-188

[46] A. Ellet, Doctoral thesis, RWTH Aachen, 2009

[47] M.W. Barsoum, Fundamentals of Ceramics, McGraw-Hill Co., 1997

[48] M. Mogensen, N. M. Sammes, G. A. Tompsett: Physical, Chemical and Electrochemical Properties of Pure and Doped Ceria, Solid State Ionics, 129, 2000, p. 63–94
[49] H. Inaba, H. Tagawa: Ceria-based solid electrolytes, Solid State Ionics, Volume 83, Issues 1–2, 1996, p. 1–16
[50] B. T. Kilbourn: Cerium: A guide to its role in chemical technology, Molycorp Inc., 1992
[51] M. Mogensen, T. Lindegaard, U.R. Hansen: Physical properties of mixed conductor solid oxide fuel cell anodes of doped CeO_2, J. Electrochem. Soc. 141, 1994, 2122.
[52] T. Inoue, T. Setoguchi, K. Eguchi, H. Arai: Study of a solid oxide fuel cell with a ceria-based solid electrolyte, Solid State Ionics 35, 1989, p. 285-291
[53] K. Eguchi, T. Setoguchi, T. Inoue, H. Arai: Electrical properties of ceria-based oxides and their application to solid oxide fuel cells, Solid State Ionics 52, 1992, p. 165-172
[54] S. Wang, H. Inaba, H. Tagawa, M. Dokiya, T. Hashimoto: Nonstoichiometry of $Ce_{0.9}Gd_{0.1}O_{1.95-x}$, Solid State Ionics, Volume 107, Issues 1–2, 1998, p. 73–79
[55] B. C. H. Steele: Appraisal of $Ce_{1-y}Gd_yO_{2-y/2}$ Electrolytes for IT-SOFC Operation at 500°C, Solid State Ionics, Volume 129, 2000, p. 95–110
[56] V. Esposito, E. Traversa: Design of electroceramics for solid oxide fuel cells applications: Playing with ceria, J. Am. Ceram. Soc., Volume 91, 2008, p. 1037–1051
[57] J. Cheng, S. Zha, X. Fang, X. Lin, G. Meng: On the green density, sintering behaviour and electrical property of tape cast $Ce_{0.9}Gd_{0.1}O_{1.95}$ electrolyte films, Mater. Res. Bull., Volume 37, 2002, p. 2437–2446
[58] D. T. Llewellyn, Roger C. Hudd: Steels: Metallurgy and Applications, Materials science engineering, Butterworth-Heinemann, 1998
[59] R. E. Smallman, A. H. W. Ngan: Physical Metallurgy and Advanced Materials, Butterworth-Heinemann, 2007
[60] http://www.chasealloys.co.uk/steel/alloying-elements-in-steel/index.html
[61] J. Engkvist, S. Canovic, K. Hellström, A. Järdnäs, J.-E. Svensson, L.-G. Johansson, M. Olssom, M. Halvarsson: Oxidation of Metals, Volume 73, 2010, p. 233-253
[62] B.A. Pint: Oxidation of Metals, Volume 45, 1996, p. 1-37
[63] R.J. Christensen, V.K. Tolpygo, D.R. Clarke: The influence of the reactive element yttrium on the stress in alumina scales formed by oxidation, Acta Materialia, Volume 45, 1997, p. 1761-1766
[64] S. Taniguchi, A. Andoh, T. Shibata: Materials Aspects in Automotive Catalytic Converters, Wiley-VCH, 2002
[65] J.A. Glasscock, L. Mikkelsen, P. Blennow, A.H. Persson, P.V. Hendriksen: Porous Fe21Cr7Al stainless steel structures for metal-supported electrochemical devices, European Powder Metallurgy Association Congress, Barcelona, 2011
[66] M. Schütze, W.J. Quadakkers: Novel Approaches to Improving High Temperature Corrosion Resistance, Woodhead Publishing Limited, Cambridge, England, 2008, p. 129-160.
[67] E. N'Dah, A. Galerie, Y. Wouters, D. Goossens, D. Naumenko, V. Kochubey, W.J. Quadakkers: Metastable alumina formation during oxidation of FeCrAl and its suppression by surface treatments, Materials and Corrosion 56, 2005, p. 843-847
[68] M.J. Bennett, J.R. Nicholls, N.J. Simms, D. Naumenko, W.J. Quadakkers, V. Kochubey, R. Fordham, R. Bachorczyk, D. Goossens, H. Hattendorf, A.B. Smith, D. Britton: Lifetime Extension of FeCrAIRE Alloys in Air: Potential Roles of an Enhanced Al-Reservoir and Surface Pre-treatment, Materials and Corrosion 56, 2005, p. 854-866
[69] J. Banhart, M.F. Ashby, N.A. Fleck: Metal Foams and Porous Metal Structures, MIT Verlag, Bremen, Germany, 1999.
[70] E. Klar, P. Samal: Powder Metallurgy Stainless Steels: Processing, Microstructures, and Properties, ASM International, Ohio- USA, 2007
[71] J. Wu, X. Liu: Recent Development of SOFC Metallic Interconnect, Journal of Materials Science and Technology 26, 2010, p. 293-305
[72] J.D. Lord, R. Morrell: Elastic modulus measurement, Measurement Good Practice Guide No. 98, Centre for Materials Measurement and Technology, National Physical Laboratory, 2007
[73] R. Morrell: Biaxial flexural strength testing of ceramic materials. Measurement Good Practice Guide No. 12 , Centre for Materials Measurement and Technology, National Physical Laboratory, 2007
[74] G.F. Vander Voort: Microindentation Hardness Testing, ASM Handbook Volume 8, Mechanical Testing and Evaluation (ASM International), 2000

[75] R.L. Smith, G.E. Sandland: An Accurate Method of Determining the Hardness of Metals, with Particular Reference to Those of a High Degree of Hardness, Proceedings of the Institution of Mechanical Engineers, Vol. I, 1922, p. 623–641
[76] B. Rutkowski, Doctoral thesis, RWTH Aachen, 2012
[77] M. Lipinska-Chwalek, J. Malzbender, A. Chanda, S. Baumann, R.W. Steinbrech: Mechanical characterization of porous $Ba_{0.5}Sr_{0.5}Co_{0.8}Fe_{0.2}O_{3-d}$, Journal of the European Ceramic Society, Volume 31, Issue 15, 2011, p. 2997-3002
[78] B.X. Huang, J. Malzbender, R.W. Steinbrech, L. Singheiser: Discussion of the complex thermo-mechanical behavior of $Ba_{0.5}Sr_{0.5}Co_{0.8}Fe_{0.2}O_{3-\delta}$, Journal of Membrane Science 359, 2010, p. 80-85
[79] N. Orlovskaya, K. Kleveland, T. Grande, M.A. Einarsrud: Mechanical properties of $LaCoO_3$ based ceramics, Journal of the European Ceramic Society 20, 2000, p. 51-56
[80] A. Fossdal, M. A. Einarsrud and T. Grande: Mechanical properties of $LaFeO_3$ ceramics, Journal of the European Ceramic Society 25, 2005, p. 927-933
[81] Y. S. Chou, J. W. Stevenson, T. R. Armstrong and L. R. Pederson: Mechanical Properties of $La_{1-x}Sr_xCo_{0.2}Fe_{0.8}0_3$ Mixed-Conducting Perovskites Made by the Combustion Synthesis Technique, Journal of the American Ceramic Society 83, 2000, p. 1457-1464
[82] B.X. Huang, J. Malzbender, R.W. Steinbrech, L. Singheiser, Mechanical properties of $La_{0.58}Sr_{0.4}Co_{0.2}Fe_{0.8}O_{3-\delta}$ membranes, Solid State Ionics, Volume 180, Issues 2–3, 2009, p. 241-245
[83] K. Yasuda, K. Uemura, T. Shiota: Sintering and mechanical properties of gadolinium-doped ceria ceramics, Journal of Physics, Volume 339, 2012
[84] M. Schweda, Doctoral thesis, RWTH Aachen, 2010.
[85] www.specialmetals.de
[86] M. Spittel, T. Spittel in: H. Warlimont (Ed.), Metal Forming Data - Ferrous Alloys - Deformation Behaviour, Springer-Verlag Berlin Heidelberg, 2009
[87] W. Weibull: A statistical distribution function of wide applicability, J. Appl. Mech.-Trans. ASME 18 (3), 1951, p. 293–297.
[88] K. Bongartz, H. Schuster: Statistical and systematical errors in the Strength Determination of brittle materials, Materialwissenschaft und Werkstofftechnik, Volume 22, Issue 12, 1991, p. 449–461
[89] G. de With, Structure, Deformation, and Integrity of Materials, Volume I: Fundamentals and Elasticity / Volume II: Plasticity, Visco-elasticity, and Fracture, Wiley-VCH, 2006
[90] B.X. Huang, J. Malzbender, R.W. Steinbrech, L. Singheiser, Mechanical properties of $La_{0.58}Sr_{0.4}Co_{0.2}Fe_{0.8}O_{3-\delta}$ membranes, Solid State Ionics, Volume 180, Issues 2–3, 2009, p. 241-245
[91] S. M. Wiederhorn, Influence of Water Vapor on Crack Propagation in Soda-Lime Glass, J. Am. Ceram. Soc. 50, 1997, p. 407-414
[92] S.R. Choi, J.A. Salem, F.A. Holland, Estimation of Slow Crack Growth Parameters for Constant Stress-Rate Test Data of Advanced Ceramics and Glass by the Individual Data and Arithmetic Mean Methods, NASA Technical Memorandum 107369, 1997.
[93] S.M. Wiederhorn, Subcritical crack growth in ceramics, Fracture Mechanics of Ceramics, 2Plenum Press, New York, 1974, p. 613–646
[94] A.A. Griffith: The phenomena of rupture and flow in solids. Phil. Trans. Roy. Soc. London, A 221, 1920, p. 163-198
[95] P. V. Hendriksen,J. R. Høgsberg, A. M. Kjeldsen,B. F. Sørensen,H. G. Pedersen, Failure Modes of Thin Supported Membranes, Advances in Solid Oxide Fuel Cells II: Ceramic Engineering and Science Proceedings, Volume 27, 2008
[96] E.T. Wessel, W.G. Clark, W.K. Wilson: Engineering methods for the design and selection of materials against fracture, Westinghouse Research labs Pittsburgh, 1966
[97] D. Broek: Elementary Engineering Fracture Mechanics, Springer, 1982
[98] A. Kaiser, S. Foghmoes, C. Chatzichristodoulou, M. Søgaard, J.A. Glasscock, H.L. Frandsen, P.V. Hendriksen: Evaluation of thin film ceria membranes for syngas membrane reactors—Preparation, characterization and testing, Journal of Membrane Science, Volume 378, 2011, p. 51-60
[99] J.W. Hutchinson, Z. Suo: Mixed Mode Cracking in Layered Materials, Advances in Applied Mechanics, Volume 29, 1992, p. 63-191
[100] Mechanical testing, ASM Handbook, Volume 8, ASM International, 2000

[101] G. Pećanac, S. Baumann, J. Malzbender: Mechanical properties and lifetime predictions for $Ba_{0.5}Sr_{0.5}Co_{0.8}Fe_{0.2}O_{3-\delta}$ membrane material, Journal of Membrane Science, Volumes 385–386, 2011, p. 263-268
[102] M.F Ashby, D.R.H. Jones: Engineering Materials 1: An Introduction to their Properties and Applications. Pergamon Press, 1980
[103] D.J. Green: An Introduction to the Mechanical Properties of Ceramics, Cambridge University Press, 1998
[104] F.R.N. Nabarro: Report on a Conference on Strength of Solids. The Physical Society of London, 1948, p. 75
[105] C.J. Herring: Diffusional viscosity of a polycrystalline solid, J. Appl. Phys, Volume 21, 1950, p. 437-445
[106] R. Coble: Model for Boundary Diffusion-Controlled Creep in Polycrystalline Materials, J. Appl. Phys, Volume 34, 1963, p. 1679-1682
[107] A.H. Chokshi: Diffusion creep in oxide ceramics, Journal of the European Ceramic Society, Volume 22, 2002, p. 2469-2478
[108] F.H. Norton: The creep of steel at high temperatures, New York , McGraw-Hill book, 1929
[109] J.X. Yi, H.L. Lein, T. Grande, S. Yakovlev, H.J.M. Bouwmeester: High-temperature compressive creep behaviour of the perovskite-type oxide $Ba_{0.5}Sr_{0.5}Co_{0.8}Fe_{0.2}O_{3-\delta}$, Solid State Ionics, Volume 180, 2009, p. 1564-1568
[110] B. Rutkowski, J. Malzbender, T. Beck, R.W. Steinbrech, L. Singheiser, Creep behaviour of tubular $Ba_{0.5}Sr_{0.5}Co_{0.8}Fe_{0.2}O_{3-d}$ gas separation membranes, J. Eur. Ceram. Soc. 31, 2011, p. 493–499
[111] B.X. Huang, R.W. Steinbrech, S. Baumann, J. Malzbender, Creep behavior and its correlation with defect chemistry of $La_{0.58}Sr_{0.4}Co_{0.2}Fe_{0.8}O_{3-\delta}$, Acta Materialia, Volume 60, 2012, p. 2479-2484
[112] D.R. Thompson, L.E. Bool, J.C. Chen: Oxygen enhanced combustion for NOx control, Final report, Praxair, 2004
[113] M. Schulz, R. Kriegel, W. Burckhardt: Modeling of oxygen flux and stress distribution for $Ba_{0.5}Sr_{0.5}Co_{0.8}Fe_{0.2}O_{3-\delta}$ membranes at application conditions, 10. Intern. Conf. Inorg. Membranes, Japan, 2008
[114] Brian R. Lawn: Fracture of Brittle Solids, Cambridge Solid State Science Series, Cambridge University Press, 1993
[115] W.D. Kingery, R.L. Coble: Effect of Porosity on Physical Properties of Sintered Alumina, Journal of the American Ceramic Society, Volume 39, Issue 11, 2006, p. 377–385
[116] F. P. Knudsen: Dependence of Mechanical Strength of Brittle Polycrystalline Specimens on Porosity and Grain Size, Journal of the American Ceramic Society, Volume 42, Issue 8, 2006, p. 376–387
[117] A. P. Roberts, E. J. Garboczi: Elastic properties of model porous ceramics, National Institute of Standards and Technology, Gaithersburg, 2000
[118] E. Ryskewitsch: Compression Strength of Sintered Alumina and Zirconia, J.Am.Ceram.Soc. 36, 65, 1953
[119] M. Radovic, E. Lara-Curzio: Mechanical Properties of Tape Cast Nickel-based Anode Materials for Solid Oxide Fuel Cells Before and After Reduction in Hydrogen, Acta. Mater. 52, 2004, p. 5747-5756
[120] Y. Yao, Master thesis, RWTH Aachen, 2012
[121] N. Nagabhushana, T. Nithyanantham, S. Bandopadhyay, J. Zhang: Subcritical crack growth behavior of a perovskite-type oxygen transport ceramic membrane, Int. J. Appl. Ceram. Technol. 8, 2011, p. 390–397
[122] E. M. Passmore, R. H. Duff, T. Vasilos: Creep of Dense, Polycrystalline Magnesium Oxide, Journal of the American Ceramic Society, Volume 49, Issue 11, 1966, p. 594–600
[123] E.Y. Sun, S.R. Nutt, J.J. Brennan: Flexural creep of coated SiC-fiber-reinforced glass-ceramic composites, J. Am. Ceram. Soc., Volume 78, 1995, p. 1233–1239
[124] C. Baudín, M.P. Villar: Microstructural and microchemical analysis of the creep damage in mullite tested in flexure, Journal of the European Ceramic Society, Volume 22, Issues 14–15, 2002, p. 2647-2655
[125] R.J. Krause, T.J. Chuang: A test method for tensile creep of structural ceramics using flexural beams, In: Ceramic today – tomorrow's ceramics, Elsevier, 1991, p. 1865
[126] P.K. Talty, R.A. Dirks: Determination of tensile and compression creep behavior of ceramic materials from bend tests, J. Mater Sci., 13, 1978, p. 580–586
[127] A.R. Rosenfield, D.K. Shetty: Estimating Damage Laws from Bend-Test Data, J. of Mat. Sci., Volume 20, 1985 p. 935-940
[128] J.H. Kim, D.B. Han, K.T. Kim: High temperature creep behavior of Cr_3C_2 ceramic composite, Mater. Sci. Eng. A212, 1996, p. 87–93
[129] C.F. Chen, T.J. Chuang: Improved analysis for flexural creep with application to sialon ceramics, J. Am. Ceram. Soc. 73 (8), 1990, p. 2366

[130] F.C. Monkman, N.J. Grant: An empirical relationship between rupture life and minimum creep rate in creep–rupture test, Proc. ASTM 56, 1956, p. 593
[131] S.M. Wiederhorn, E.R. Fuller: Structural reliability of ceramic matrials, Mater. Sci. Engng., 71, 1985, p. 169-186
[132] B.J. Dalgleish, S.M. Johnson, A.G. Evans, W. Blumenthal: High temperature failure of polycrystalline alumina: I, II, III. J.Am.Ceram. Soc., 67, 1984, p. 741-763
[133] F. Dobes, K. Milicka: The relation between minimum creep rate and time to fracture, Met. Sci. 10, 1976, p. 382
[134] A.I.Y. Tok, F.Y.C Boey, K.A Khor: Tape casting of high dielectric ceramic composite substrates for microelectronics application, Journal of Materials Processing Technology, Volumes 89–90, 1999, p. 508-512
[135] P. Kountouros, R. Förthmann, A. Naoumidis, G. Stochniol, E. Syskakis: Synthesis, forming and characterization of ceramic materials for the planar solid oxide fuel cell (SOFC), Ionics, Volume 1, p. 40-50
[136] T. Klemensø, M. Menon, S. Ramousse, Low toxicity binder systems for tape cast $Ce_{0.9}Gd_{0.1}O_{1.95}$ laminates, Ceramics International, Volume 36, 2010, p. 773
[137] R.L. Smith, G.E. Sandland: An Accurate Method of Determining the Hardness of Metals, with Particular Reference to Those of a High Degree of Hardness, Proceedings of the Institution of Mechanical Engineers, Vol. I, 1922, p. 623–641
[138] W. C. Oliver, G. M. Pharr: An improved technique for determining hardness and elastic modulus using load and displacement sensing indentation experiments, J. Mater. Res., Vol. 7, No. 6, 1992
[139] G. Pećanac, T. Bause, J. Malzbender: Ring-on-ring testing of thin, curved bi-layered materials, J. Eur. Ceram. Soc. 31, 2011, p. 2037–2042
[140] M.N. Giovan, G. Sines, Biaxial and uniaxial data for statistical comparisons of ceramic's strength, J. Am. Ceram. Soc., Volume 62, 1979, p. 510
[141] J. Malzbender, R.W. Steinbrech: Fracture test of thin sheet electrolytes for solid oxide fuel cells, J. Eur. Ceram. Soc., Volume 27, 2007, p. 597–603
[142] G.J. Hahn, S.S. Shapiro: Statistical models in engineering, J. Wiley and Sons, New York, 1967
[143] R.W. Davidge, G. Tappin: Thermal shock and fracture in ceramics, Trans. Br. Ceram. Soc., Volume 66, 1967, p. 405
[144] J.H. Kim, D.B. Han, K.T. Kim: High temperature creep behavior of Cr_3C_2 ceramic composite, Mater. Sci. Eng. A212, 1996, p. 87–93
[145] C.F. Chen, T.J. Chuang, Improved analysis for flexural creep with application to sialon ceramics, J. Am. Ceram. Soc. 73 (8), 1990, p. 2366
[146] Characterization and failure analysis of plastics, ASM International, 2003
[147] R. Morrell, B. Roebuck, E.G. Bennett: Microstructural measurement on ceramics and hardmetals, Measurement Good Practice Guide No. 21, 2007
[148] J. Malzbender, NASA-OTM project report, Jülich, January 2010.
[149] C. Chatzichristodoulou, M. Sogaard, J. Glasscock, A. Kaiser, S. Foghmoes: Oxygen Permeation in Thin, Dense CeGdO Membranes II. Experimental Determination, Electrochemical Society Journal , Volume 158, issue: 5, 2011, p. F73-F83
[150] S. McIntosh, J. F. Vente, W. G. Haije, D. H. A. Blank, H. J. M. Bouwmeester: Oxygen Stoichiometry and Chemical Expansion of $Ba_{0.5}Sr_{0.5}Co_{0.8}Fe_{0.2}O_{3-d}$ Measured by in Situ Neutron Diffraction, Chem. Mater., Volume 18, 2006, p. 2187-2193
[151] A. Chanda, B.X. Huang, J. Malzbender, R.W. Steinbrech: Micro- and macro-indentation behaviour of $Ba_{0.5}Sr_{0.5}Co_{0.8}Fe_{0.2}O_{3-d}$ perovskite, Journal of the European Ceramic Society, Volume 31, Issue 3, 2011, p. 401-408
[152] R. Kao, N. Perrone N, W. Capps: Large- deflection solution for the coaxial-ring circular-glass-plate flexure problem. J. Am. Ceram. Soc., Volume 54, 1971, p. 566–571
[153] A. Selcuk, A. Atkinson: Strength and toughness of tape-cast yttria-stabilized zirconia. J. Am. Ceram. Soc., Volume 83 (8), 2000, p. 2029–2035
[154] J. Malzbender, R.W. Steinbrech: Substrate stiffness determination in curved layered composites using bending methods, Surf Coat Technol, Volume 202(2), p. 379–81
[155] C.H. Hsueh: Some considerations of determination of residual stresses and Young's moduli in ceramic coatings. J Am Ceram Soc, Volume 74 (7), 1991, p. 1646–1649

[156] J. Malzbender, W. Fischer, R.W. Steinbrech: Studies of residual stresses in planar solid oxide fuel cells. J Power Sources, Volume 182 (8), 2008, p. 594–598
[157] T. Bause, PhD thesis, RWTH Aachen, 2012
[158] B. Huang, PhD thesis, RWTH Aachen, 2010
[159] B.J. Dalgleish, E. Slamovich, A.G. Evans: High temperature failure of ceramics, J. Mater. Energy Systems 8, 1986, p. 211
[160] K. Bongartz, E. Gyarmati, H. Schuster, K. Tauber: The Brittle Ring Test: a method for measuring strength and young's modulus on coatings of HTR fuel particles, J Nucl Mater, Volume 62 (2–3), 1976, p. 123–137
[161] J.H. Kim, D.B. Han, K.T. Kim: High temperature creep behavior of Cr_3C_2 ceramic composite, Mater. Sci. Eng. A212, 1996, p. 87–93
[162] C.F. Chen, T.J. Chuang: Improved analysis for flexural creep with application to sialon ceramics, J. Am. Ceram. Soc. 73 (8), 1990, p. 2366
[163] M. Lipinska-Chwalek, 8th Mem-Oxycoal project meeting report, Münster, 8-9 November, 2011
[164] M. Lipinska-Chwalek, Mem-Oxycoal Project meeting, Würzburg, 9-10 May 2012
[165] M. Tanaka, Y. Ito, R. Kato, A. Kayama, Grain size dependence of creep–rupture properties and fracture mechanism in austenitic SUS304 steel at 973 K, J. Mater. Sci. Lett. 19, 2000, p. 899–902
[166] J. Zhou, Y. Li, R. Zhu, Z. Zhang: The grain size and porosity dependent elastic moduli and yield strength of nanocrystalline ceramics, Materials Science and Engineering: A, Volumes 445–446, 2007, p. 717-724
[167] J. Luo, R. Stevens: Porosity-dependence of elastic moduli and hardness of 3Y-TZP ceramics, Ceramics International, Volume 25, Issue 3, 1999, p. 281-286

Acknowledgement

I would like to thank Univ.-Prof. Dr.-Ing. L. Singheiser for providing excellent conditions during my PhD study at the IEK-2 Institute at Forschungszentrum Jülich GmbH, and Univ.-Prof. J. Schneider, Ph.D., for his great support as the DoctorVater of my thesis. I am also very grateful to Univ.-Prof. Dr.-Ing. T. Beck for his thorough and precise scientific supervision and valuable instructions.

Very deep and sincere appreciation goes to Dr. R.W. Steinbrech for his outstanding leadership. For providing excellent scientific support, my honest gratitude and special thanks go to Dr. J. Malzbender, who has been invaluable on both an academic and a personal level.

Furthermore, I would like to thank all partners from the NASA-OTM project for an encouraging project work, especially Dr. W.A. Meulenberg for his project guidance, and Dr. S. Baumann and Dr. S. Foghmoes for their excellent collaboration.

T. Osipova, J. Mönch and R. Küppers are kindly acknowledged for their experimental support, Dr. E. Wessel and Dr. D. Grüner for SEM studies, J. Bartsch and V. Gutzeit for their assistance in metallographic preparations, and Mrs. M. Offermann, Mrs. M. Felden and P. Joecken for their technical support.

Many thanks to my colleagues from the working group: Dr. B. Rutkowski, Dr. M. Lipińska-Chwałek, Dr. O. Tokariev, Prof. W. Araki, V. Stournari, Y. Zhao, A. Böhm, Dr. B. Huang, E. Skiera, V. Vasechko, and T. Bause. I am especially grateful to W.A. Popolović for bringing the team spirit into the group. Many thanks also go to all my friends in Croatia, who supported me during my PhD study.

Above all, to my wife and family, for their support and patience at all times – thank you.

Band / Volume 165
Interest Mediation and Policy Formulation in the European Union
Influence of Transnational Technology-Oriented Agreements on European Policy in the Field of Carbon Capture and Storage
Advances in Systems Analysis 3
O. Schenk (2013), XIII, 253 pp
ISBN: 978-3-89336-852-5

Band / Volume 166
Versagensverhalten plasmagespritzter Mg-Al-Spinell-Schichten unter Thermozyklierung
S. M. Ebert (2013), X, 173 pp
ISBN: 978-3-89336-853-2

Band / Volume 167
Coupled modeling of water, vapor and heat in unsaturated soils - Field applications and numerical studies
C. Steenpaß (2013), X, 123 pp
ISBN: 978-3-89336-854-9

Band / Volume 168
An analysis of the global atmospheric methane budget under different climates
A. Basu (2013), v, 110 pp
ISBN: 978-3-89336-859-4

Band / Volume 169
Experimental determination of the partitioning coefficient of nopinone as a marker substance in organic aerosol
B. Steitz (2013), 132 pp
ISBN: 978-3-89336-862-4

Band / Volume 170
Ion Beam Treatment of Functional Layers in Thin-Film Silicon Solar Cells
W. Zhang (2013), xi, 191 pp
ISBN: 978-3-89336-864-8

Band / Volume 171
Pulvermetallurgische Herstellung von porösem Titan und von NiTi-Legierungen für biomedizinische Anwendungen
M. Bram (2013), X, 238 pp
ISBN: 978-3-89336-866-2

Band / Volume 172
IEK-3 Report 2013. Langlebige Elektrochemische Verfahrenstechnik
(2013), ca. 185 pp
ISBN: 978-3-89336-868-6

Band / Volume 173
Combined Steady State and High Cycle Transient Heat Load Simulation with the Electron Beam Facility JUDITH 2
Th. Loewenhoff (2013), XVI, 108 pp
ISBN: 978-3-89336-869-3

Band / Volume 174
High-Quality Thorium TRISO Fuel Performance in HTGRs
K. Verfondern, H. Nabielek, M.J. Kania, H.-J. Allelein (2013), viii, 109 pp
ISBN: 978-3-89336-873-0

Band / Volume 175
Characterization of effective hydraulic properties of unsaturated porous media using spectral induced polarization (SIP)
K. Breede (2013), xiv, 72 pp
ISBN: 978-3-89336-875-4

Band / Volume 176
Zur Mikrostruktur siliziumbasierter Dünnschichten für die Photovoltaik
F. Köhler (2013), i, 100 pp
ISBN: 978-3-89336-876-1

Band / Volume 177
Grundlagen für die Transformation von Energiesystemen
Texte und Ergebnisse der Cadenabbia-Tagung 2012
der Konrad-Adenauer-Stiftung und des Forschungszentrum Jülich GmbH
L. Gruber, J.-F. Hake (Eds.) (2013), VI, 114 pp
ISBN: 978-3-89336-877-8

Band / Volume 178
Thermo - mechanical investigations and predictions for oxygen transport membrane materials
G. Pećanac (2013), 143 pp
ISBN: 978-3-89336-878-5

Weitere ***Schriften des Verlags im Forschungszentrum Jülich*** unter
http://wwwzb1.fz-juelich.de/verlagextern1/index.asp

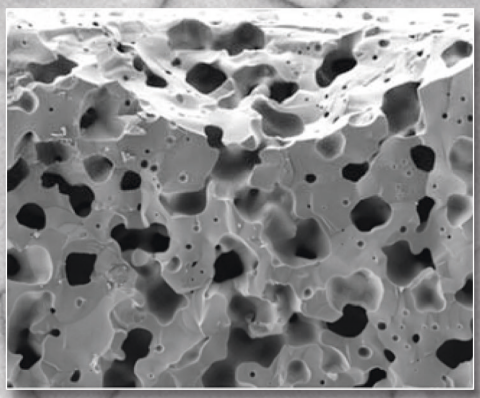
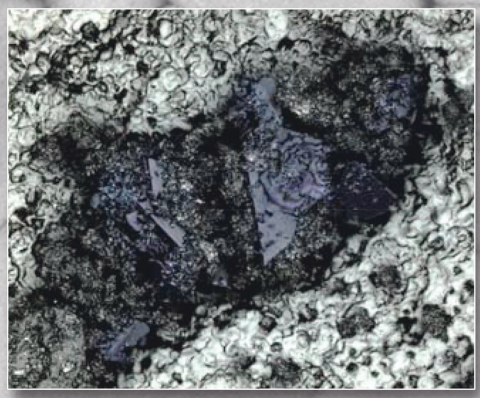
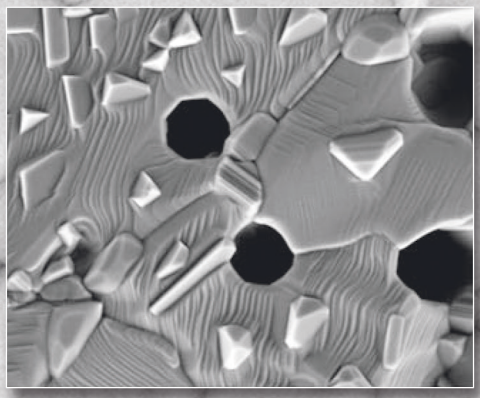
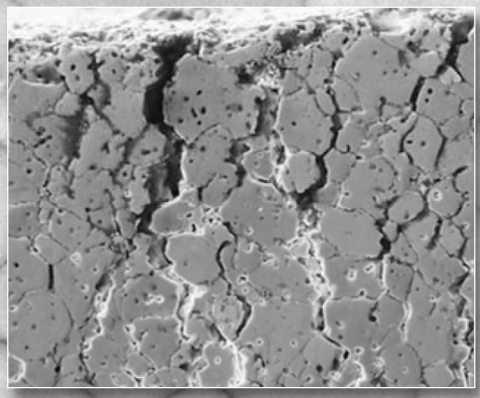

Energie & Umwelt / Energy & Environment
Band / Volume 178
ISBN 978-3-89336-878-5

JÜLICH
FORSCHUNGSZENTRUM